Universidad de Alcalá

ACTA DE EVALUACIÓN DE LA TESIS DOCTORAL

Año académico 2016/17

DOCTORANDO: **LIDÓ DE LA MUELA, CRISTINA**
D.N.I./PASAPORTE: ******209J**

PROGRAMA DE DOCTORADO: **D347 DOCTORADO EN TECNOLOGÍAS DE LA INFORMACIÓN Y LAS COMUNICACIONES**
DEPARTAMENTO DE: **TEORÍA DE LA SEÑAL Y COMUNICACIONES**
TITULACIÓN DE DOCTOR EN: **DOCTOR/A POR LA UNIVERSIDAD DE ALCALÁ**

En el día de hoy 21/03/17, reunido el tribunal de evaluación nombrado por la Comisión de Estudios Oficiales de Posgrado y Doctorado de la Universidad y constituido por los miembros que suscriben la presente Acta, el aspirante defendió su Tesis Doctoral, elaborada bajo la dirección de **JOSÉ CARLOS NIETO BORGE .**

Sobre el siguiente tema: *ANALYSIS OF SEA SURFACE FEATURES BY USING X-BAND RADAR DATA SETS*

Finalizada la defensa y discusión de la tesis, el tribunal acordó otorgar la CALIFICACIÓN GLOBAL[2] de (**no apto, aprobado, notable** y **sobresaliente**): _Sobresaliente_

Alcalá de Henares, _21_ de _marzo_ de _2017_

EL PRESIDENTE   EL SECRETARIO   EL VOCAL

Fdo.: _Germán Rodríguez Rguez_   Fdo._Enrique Alexandre Cortno_   Fdo.: _Jochim Horstmann_

Con fecha _29_ de _marzo_ de _2017_ la Comisión
Delegada de la Comisión de Estudios Oficiales de Posgrado,
a la vista de los votos emitidos de manera anónima por el
tribunal que ha juzgado la tesis, resuelve:

☒ Conceder la Mención de "Cum Laude"
☐ No conceder la Mención de "Cum Laude"

FIRMA DEL ALUMNO,

La Secretaria de la Comisión Delegada

Fdo.: ....

INCIDENCIAS / OBSERVACIONES:

Universidad de Alcalá

COMISIÓN DE ESTUDIOS OFICIALES
DE POSGRADO Y DOCTORADO

En aplicación del art. 14.7 del RD. 99/2011 y el art. 14 del Reglamento de Elaboración, Autorización y Defensa de la Tesis Doctoral, la Comisión Delegada de la Comisión de Estudios Oficiales de Posgrado y Doctorado, en sesión pública de fecha 29 de marzo, procedió al escrutinio de los votos emitidos por los miembros del tribunal de la tesis defendida por *LIDÓ DE LA MUELA, CRISTINA*, el día 21 de marzo de 2017, titulada *ANALYSIS OF SEA SURFACE FEATURES BY USING X-BAND RADAR DATA SETS*, para determinar, si a la misma, se le concede la mención "cum laude", arrojando como resultado el voto favorable de todos los miembros del tribunal.

Por lo tanto, la Comisión de Estudios Oficiales de Posgrado **resuelve otorgar** a dicha tesis la

MENCIÓN "CUM LAUDE"

Alcalá de Henares, 31 de marzo de 2017
EL PRESIDENTE DE LA COMISIÓN DE ESTUDIOS
OFICIALES DE POSGRADO Y DOCTORADO

Juan Ramón Velasco Pérez

Copia por e-mail a:
Doctorando: LIDÓ DE LA MUELA, CRISTINA
Secretario del Tribunal: ENRIQUE ALEXANDRE CORTIZO.
Director de Tesis: JOSÉ CARLOS NIETO BORGE

UNIVERSIDAD DE ALCALÁ, PATRIMONIO DE LA HUMANIDAD
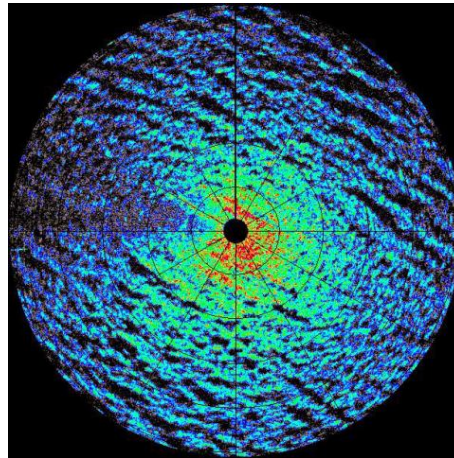
Universidad de Alcalá

Escuela Politécnica Superior

Departamento de Teoría de la Señal y Comunicaciones

TESIS DOCTORAL

Analysis of Sea Surface Features by Using X-Band Radar Data Sets

Autor:

Cristina Lidó de la Muela

Director:

Dr. D. José Carlos Nieto Borge

Enero 2017

Programa: *Doctorado en Tecnologías de la Información y las Comunicaciones*
(RD 1397/2007) - D347

Dpto. de Teoría de la Señal y Comunicaciones
Campus Universitario s/n
28805 Alcalá de Henares (Madrid)
Telf: (+34) 91 885 66 54
Fax: (+34) 91 885 66 99
E-mail: josecarlos.nieto@uah.es
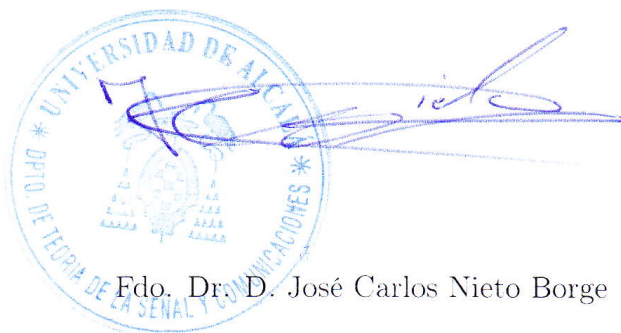
Dr. José Carlos Nieto Borge, Profesor Titular de Universidad en el Área de Conocimiento de Teoría de la Señal y Comunicaciones de la Universidad de Alcalá,

CERTIFICA

Que la tesis **"Analysis of sea surface features by using X-Band radar data sets"**, presentada por Dña. Cristina Lidó de la Muela, realizada en el Departamento de Teoría de la Señal y Comunicaciones bajo mi dirección, reúne los méritos suficientes para optar al grado de Doctor, por lo que puede procederse a su depósito y defensa.

Alcalá de Henares, enero de 2017.

Fdo. Dr. D. José Carlos Nieto Borge

Universidad de Alcalá

Dña. Cristina Lidó de la Muela ha realizado en el Departamento de Teoría de la Señal y Comunicaciones, y bajo la dirección del Doctor D. José Carlos Nieto Borge, la tésis doctoral titulada **"Analysis of sea surface features by using X-Band radar data sets"**, cumpliendo todos los requisitos para la tramitación que conduce a su posterior lectura.

Alcalá de Henares, enero de 2017.

EL DIRECTOR DEL DEPARTAMENTO

Fdo. Dr. D. Francisco Javier Acevedo Rodríguez

Universidad de Alcalá

Escuela Politécnica Superior

Departamento de Teoría de la Señal y Comunicaciones

Tesis Doctoral

ANALYSIS OF SEA SURFACE FEATURES BY USING X-BAND RADAR DATA SETS

Autora:
Cristina Lidó de la Muela

Director:
Dr. José Carlos Nieto Borge

Enero, 2017

Abstract

In this work some phenomena that happen in the ocean, which are caused by wind-generated waves, are studied by using microwave remote sensing techniques. These phenomena are related to the processes responsible of the radar imaging effects in X-band at grazing incidence conditions responsible of the formation of the radar images, commonly known for navigation purposes as sea clutter. Those imaging mechanisms permit to detect phenomena such as the dispersion relation of the waves, its higher harmonics or the so-called group line. The study of all these phenomena it is carried out from the analysis of the spectrum of the X-band marine radar images, provided by measuring stations based on X-band marine radar technology. These radar systems supply temporal sequences of marine images. Hence, after a three-dimensional spatio-temporal Fourier decomposition, the spectra of the time series of radar images is derived and analysed. The spectrum of the X-band marine radar images provides information about the distribution of the wave energy, and it is possible to see all the phenomena related to waves, local wind, etc. The study of the clutter, or the background noise of the spectrum, is important as well because it is very useful to estimate the significant wave height.

A detailed study related to the detection of the group line and the dispersion relation dependent on the different azimuths that sweep the radar image and different ranges from the location of the radar is presented in this work. Besides a Signal to Noise Ratio study is collected considering the phenomena commented before and the illumination mask, due to the shadowing effect of the radar antenna, of the free sea surface because it includes the main contributions of image spectrum energy.

Resumen

En este trabajo se recoge el estudio de algunos de los fenómenos que ocurren en el océano debido al oleaje mediante técnicas de teledetección en el rango de las microondas. Estos fenómenos están relacionados con los diferentes mecanismos de formación de la imagen radar en banda X y en condiciones de incidencia tangente. Dichos mecanismos permiten detectar fenómenos en dichas imágenes radar (conocidas como *clutter marino* para propósitos de navegación), como son la relación de dispersión del oleaje, sus armónicos superiores y la contribución espectral conocida en la literatura científica como *group line*. Para el estudio de estos fenómenos se emplean los espectros de las imágenes proporcionadas por diferentes estaciones que utilizan tecnología basadas en radar de navegación en banda X. Los sistemas radar proporcionan una secuencia de imágenes en el dominio del tiempo que, gracias a la descomposición tridimensional de Fourier, permite obtener dichos espectros correspondientes de la secuencia de imágenes radar para su posterior análisis. Así, el espectro de la secuencia de imágenes de radar marino proporciona información sobre la distribución de la energía del oleaje, haciendo visible todos los fenómenos relacionados con el oleaje, el viento local, etc. El estudio del clutter, o del ruido de fondo del espectro, también es importante ya que permite la estimación de la altura significativa de las olas.

En este trabajo se recoge un estudio detallado de la detección del *group line* y de la relación de dispersión del oleaje en función de la dirección de los diferentes ángulos de azimut que barren la imagen del radar, así como para diferentes alcances a partir de la ubicación del radar, además, de un estudio de la relación señal-ruido considerando los fenómenos anteriores, así como de la máscara de iluminación de la superficie del mar, debida al efecto de ensombrecimiento de la antena radar, que también contiene las principales contribuciones del espectro de la imagen.

To my parents and my sister.

To those friends who support me, and supported me, in this adventure.

Acknowledgements

I would be an ungrateful if I do not express my grateful to those people who encourage and help me to carry out this work.

- José Carlos Nieto Borge: My supervisor and my reference, giving me the opportunity to develop this work, helping me and encouraging me untiringly. For all of these funny and exhausting moments.

- Jochen Horstmann: 'Il mio capo tedesco'. Thank you to give me the opportunity to meet you and work for you. It was a great experience, and the moments living with you are countless.

- Sancho Salcedo: For your encouragement from the first moment that I decided to do this work.

- My colleagues at NURC-CMRE: For all of those nice people who helped and taught me new knowledge.

- OceanWaveS GmbH: For the provision of the WaMoS acquired at the FINO 1 and Hörnum.

Contents

Bibliography

List of Figures

List of Tables

Chapter 1

Introduction

The study of ocean waves is very complicated because of the sea state can vary significantly, but it is very important because it is widely used for the design of marine structures, such as oil platforms, breakwaters, off-shore platforms, ships, etc. Furthermore, waves and currents are some of the most important phenomena to distribute the temperature of the ocean, modifications of the coastline, the quality of the water and sea life, etc.

The ordinary X-band marine radar is a device that scan the free sea surface at grazing incidence with HH-polarization. The marine radar images are due to the interaction of the electromagnetic waves emitted by the radar with the sea surface ripples caused by the local wind. The images of the sea surface and the measurements of the ocean waves parameters are based on the analysis in spatial and temporal domain of the sea surface. The main benefit of marine radars is that it can be used as remote sensing system for oceanographic purpose. The most of the marine radars have installed the Wave Monitoring System WaMoS II to monitor the real time measurements of directional ocean wave spectra. They are able to monitor the sea surface in both time and space allowing the determination of unambiguous directional wave spectra.

The X-band marine radar images have to be handled to work easily. Therefore, a three-dimensional Fourier Transform is applied in the images getting the spectrum of the radar image of the sea surface. In the spectrum it is possible to see the distribution of the energy of the sea. There are some characteristic phenomena, or energy distributions, in the spectrum related to waves. The main energy is located in the dispersion relation caused by waves. The dispersion shell relates the dependency between the angular frequency and the wave number describing the shape of the wave propagation. With the dispersion shell it is possible to study the behaviour of the ocean waves, as well as the wind speed and direction.

Then the rest of the energy is distributed in other structures visible as ocean wave features in the spectrum, such as the subharmonic group line and the higher harmonics of the dispersion relation. The group line is the combination of nonlinear phenomena existing in the surface of the ocean, such as the wind, the effects produced by the waves breaking, etc. The group line study is not easy because of the closeness with the dispersion shell. This makes the isolation of

the group line difficult. Moreover the size and the intensity of the group line is modified by the intensity of the wind, the wave direction and the range in the radar image. The rest of the low energy is distributed in the background spectral noise. This background spectral noise is useful to estimate the significant wave height, because the accuracy of the estimation of additional sea state parameters as the significant wave height.

The data employed in this work come from two different stations. The first station is FINO 1, located in the North Sea, near the German island of Borkum. The second station is Hörnum, which is located in the German island of Sylt. In addition, simulation techniques of radar images based in the stochastic theory of ocean waves have been employed. In this case, radar imagery have been obtained from simulated wave fields that hold a given theoretical meteorological situation. Simulation techniques provide realistic synthetic sea clutter images and they have shown that the main sea surface modulation mechanisms for grazing incident and horizontal polarization is the shadowing and the tilt modulation. Illumination mask of the free sea surface is as well obtained and its spectrum includes the most important phenomena related to waves, such as dispersion relation and the subharmonics.

This Thesis is divided in nine chapters which are grouped in two blocks. The first block is a theoretical background related to the stochastic description of the ocean waves and sea states in chapter 2, and radar theory and the processes followed in X-band marine radar images in chapter 3. The second block is the work carried out in this Thesis related to the analysis of the sea surface from X-band marine radar images. The chapter 4 presents the dispersion relation detection according to the range and azimuth of the marine radar. Another characteristic feature of the sea is the known as group line, which is going to be presented in chapter 5. The Signal to Noise Ratio according to the azimuth and range of the marine radar is collected in chapter 6. In chapter 7 the used data will come from the Hörnum station and the main features as the dispersion relation, the group line and SNR will be studied. In chapter 8 a comparison of the simulation of wave fields and real marine radar data is presented. The sea surface current detected by different devices is collected in chapter 9. The last chapter summarises the conclusions of this work.

Part I

Theoretical Background

Chapter 2

Stochastic Description of Ocean Waves

2.1 Wind-generated waves

Ocean waves play an important role in the energy transference mechanisms between the Atmosphere and the Ocean. Furthermore, ocean waves can be a dangerous hazard for human activities, such as navigation, on- and off-shore platforms maintenance, coastal and oceanic management and engineering, etc. At present, a proper characterisation of the properties of ocean wave fields is an important issue still under research.

The Ocean is a complex dynamical system that presents different kind oceanic oscillations (e.g. tides, internal waves, planetary waves, etc.). One of these oceanic oscillations are the so-called wind-generated waves. The general idea about wind-generated waves, or more commonly known as ocean waves, is the effect produced by the wind blowing over the free sea surface. Wind-generated waves transmit energy instead of mass [2]. Ocean waves consume a small amount of their energy in their movement but mainly when they are closed to the coast, where ocean waves break releasing the potential and kinetic energy, because of the shallow water conditions. However, other ocean oscillations are caused by water mass transmission, such as tsunamis, which are due to seismic movements with vertical component, or pushing heavy material stuff against the water. An overview of the physical oscillation phenomena on the sea can be seen in the figure 2.1.

When the ocean waves correspond to the same area where the wind is blowing, the wave field is known as *wind sea*. Once those waves propagate to different geographical locations, far away from the storm that generated the wind sea, the wave field is known in the scientific literature as *swell*. Commonly wind sea waves present a large spreading in the wave propagation directions than swell. In addition, those wave fields corresponding to swell cases are usually composed of larger wave lengths and wave periods than the wind sea cases. In general, it is common in the ocean to measure wave fields composed of two or more individual wave systems (i.e. superposition of different swell and wind sea cases). Those mixed wave fields are known in the scientific literature as multimodal wave fields, in contrast of those wave fields formed by a unique wave system (swell or wind sea), which are known as unimodal wave fields.
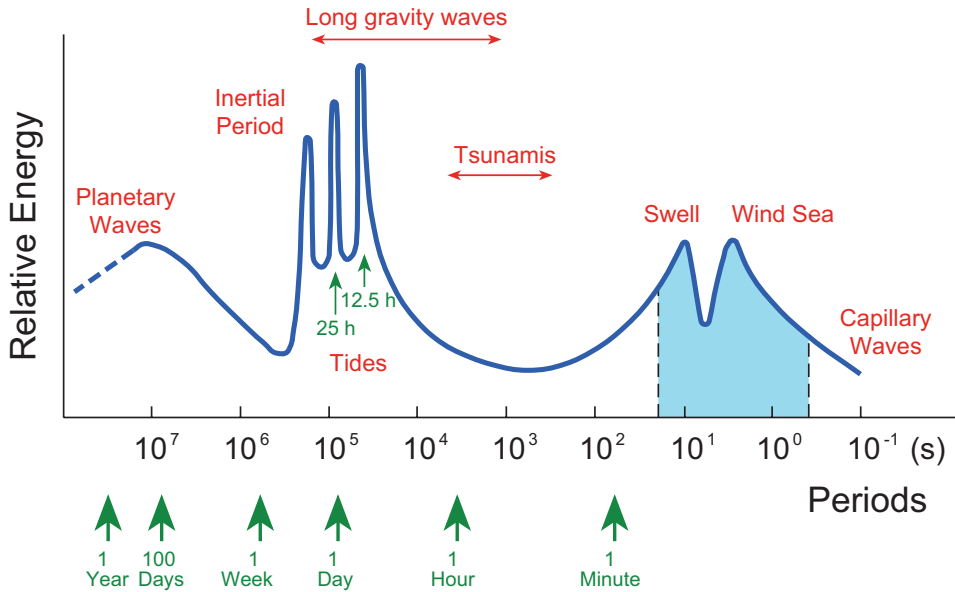
Figure 2.1: Scheme showing the relative energy of different oceanic oscillations (adapted from Pond and Pickard, 1983 [1]).

For practical applications, and mainly offshore and deep areas, it is usually considered that those ocean wave fields (e.g wind sea and swell) can be described using a linear approach for the solutions of the hydrodynamic equations that describe the oscillation of the free sea surface forced by the wind. This linear description is as well applicable in practice for moderate water depth conditions. However, it is not possible to assume this statement close to the coast, where nonlinear effects take an important role in the wave dynamics due to the effects of the bottom topography [3]. The description of the surface of a single wave affected by the wind seems chaotic and irregular in time and space. Therefore, additionally of the hydrodynamic description of the wave oscillation movements, the stochastic theory is as well applied. Then, ocean waves are described from the concept of *sea state*. A sea sate is a wave field that presents constant statistical properties for a time interval (typically about one hour) and for a given oceanic area (few squared kilometres for deep waters). Therefore, a sea state can be regarded as a stochastic process stationary in time and homogeneous in space [4]. The following sections deal with and overview of the hydrodynamic wave theory in combination with stochastic approach applied to linear wave fields.

2.2   Theoretical description of linear ocean waves

Under the frame of the linear theory (see appendix A), the solution of the vertical wave displacement η over the mean sea level is given by the equation $z = \eta(\mathbf{r}, t)$, where $\mathbf{r} = (x, y)$ is the sea surface location and t denotes the time. A monochromatic solution for $\eta(\mathbf{r}, t)$ is given by

$$\eta(\mathbf{r}, t) = a \cos\left(\mathbf{k} \cdot \mathbf{r} - \omega t + \varphi\right) = \frac{a}{2} e^{j(\mathbf{k} \cdot \mathbf{r} - \omega t + \varphi)} + \text{c.c.} \tag{2.1}$$

where a is the amplitude, $\mathbf{k} = (k_x, k_y)$ is the wave number vector, ω is the angular frequency, and φ is the phase. The expression $c.c.$ stands for the complex conjugate, being $\mathrm{j} = \sqrt{-1}$. Often the phase φ is combined with the amplitude a in the so-called complex amplitude $c = a\,\mathrm{e}^{\mathrm{j}\varphi}/2$. Taking into account the linear wave approach, a more general solution of the wave elevation is regarded as the superposition of different monochromatic wave components

$$\eta(\mathbf{r}, t) = \sum_n c_n \mathrm{e}^{\mathrm{j}(\mathbf{k}_n \cdot \mathbf{r} - \omega_n t)} + \text{c.c.} \tag{2.2}$$

where each monochromatic component is labeled with the index n. In principle, equation (2.2) does not consider that the monochromatic components $n = 1, 2, \ldots$ are harmonics. Figure 2.2 shows and scheme of the linear superposition of individual monochromatic waves to reconstruct the sea surface elevation η.
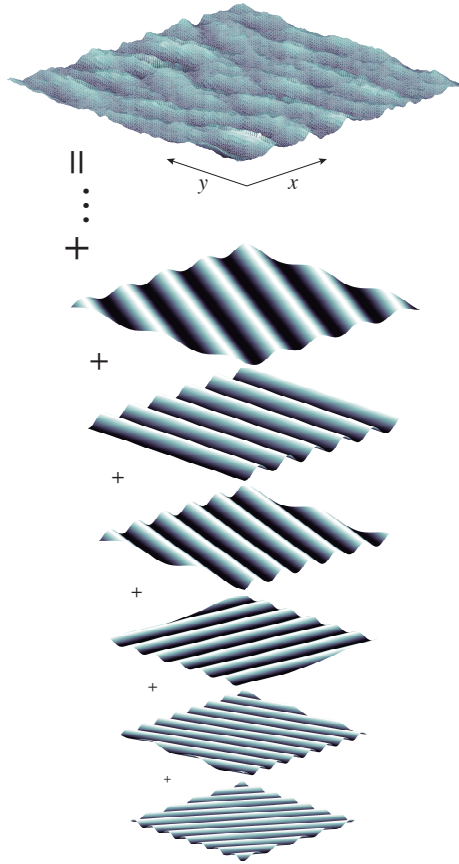
Figure 2.2:   Reconstruction of the sea surface elevation $\eta(\mathbf{r})$ at a given time t from the superposition of different monochromatic wave components. Adapted from [5].

2.2.1   Dispersion relation

The spatial evolution of ocean waves is related to the temporal evolution through the so-called *dispersion relation.* Thus, under the frame of the linear wave theory, ocean waves are dispersive and the dispersion relation, $\omega = \varpi(\mathbf{k})$, is given by [6]

$$\omega = \varpi(\mathbf{k}) = \sqrt{gk\tanh(kd)} + \mathbf{k} \cdot \mathbf{U} \tag{2.3}$$

where $k = |\mathbf{k}|$, g is the acceleration of the gravity, d is the water depth and $\mathbf{U} = (U_x, U_y)$ is the so-called *current of encounter* that can be due to a geophysical currents (e.g. tides, etc.) or due to a relative motion between the wave field and the observer (e.g. the sensor) [7]. In equation (2.3), the surface tension of water are neglected because the typical wavelengths of ocean waves are bigger enough, covering the range from some meters until several hundred meters. For deep water ($kd \to \infty \Rightarrow \tanh(kd) = 1$) the dispersion relation can be simplified as:

$$\omega = \varpi(\mathbf{k}) = \sqrt{gk} + \mathbf{k} \cdot \mathbf{U} \tag{2.4}$$

It can be seen in equation (2.3) that the relationship between ω and $\mathbf{k}$ is not linear. Therefore, ocean waves are dispersive, having different values of the phase $v_p = \omega/k$ and group velocity $v_g = \mathrm{d}\omega/\mathrm{d}k$ for each monochromatic wave component. In addition, $v_p \neq v_g$.

2.2.1.1   Dispersion shell

The dispersion relation (2.3) forms a manifold in the $(\mathbf{k}, \omega)$-space, which is commonly known as *dispersion shell* [8]. The dispersion shell can be presented as the equation (2.3):

$$\omega = \varpi(\mathbf{k}) = \sqrt{gk\tanh(kd)} + \mathbf{k} \cdot \mathbf{U}$$

As there is an important connection between the angular frequency ω and the wave number $\mathbf{k}$, it is necessary to know the effect on the dispersion relation when the current of encounter $\mathbf{U} = (U_x, U_y)$ or the depth d change.

- Effect of the current of encounter

    Taking into account a constant depth, if the current is considered as $\mathbf{U} = 0$, the function of the dispersion $\varpi(\mathbf{k})$ depends only on the modulus of the wave number. If the wave number increases, the dispersion relation $\varpi(\mathbf{k})$ increases as well. Therefore, for a plane of $\omega = $ constant, the level curves depending on (k_x, k_y) are be concentric circumferences and the radius of the circumference increases when ω increases. The figure 2.3 presents the thee-dimensional dispersion shell $\omega = \varpi(\mathbf{k})$ when the current is absent.

    However, the figure 2.4 shows the current effect in the three-dimensional dispersion shell $\omega = \varpi(\mathbf{k})$ when the current of encounter is presented and its value is equal to
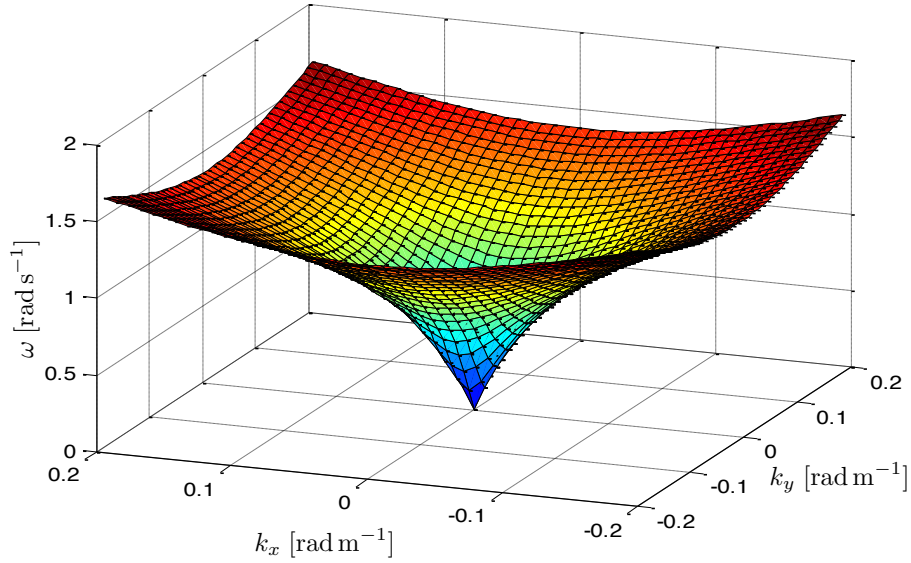
Figure 2.3: Dispersion shell $\omega = \varpi(\mathbf{k})$ with lack of current of encounter.
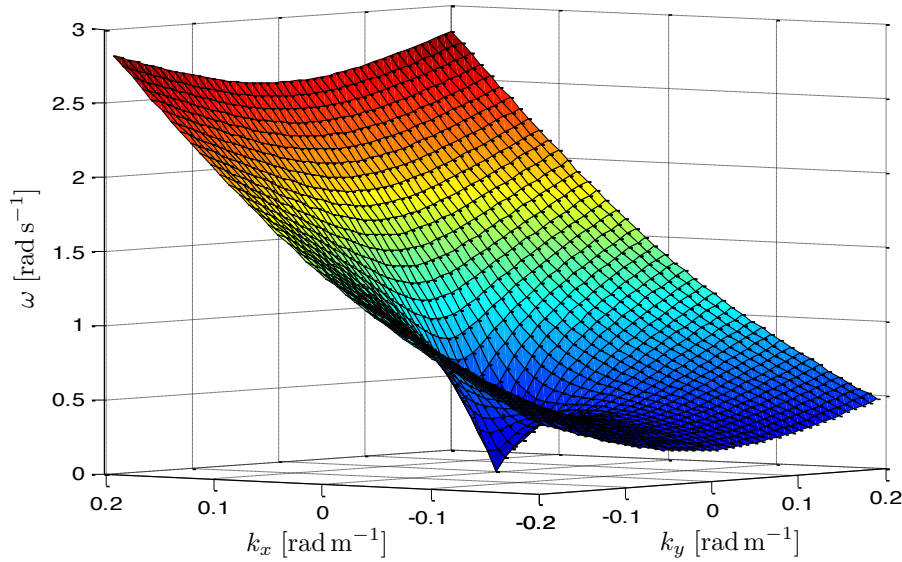
Figure 2.4: Dispersion shell $\omega = \varpi(\mathbf{k})$ for a current of encounter $\mathbf{U} = (6, 0)\,\mathrm{m\,s}^{-1}$.

$\mathbf{U} = (6, 0)\,\mathrm{m\,s}^{-1}$. In this case, the angular frequency increases only when the term $\mathbf{k}\cdot\mathbf{U} > 0$. Whereas if the term $\mathbf{k} \cdot \mathbf{U} < 0$, the function of ω decreases in the another direction. Thus, if the current $\mathbf{U}$ increases, the semi-plane corresponding to $\mathbf{k} \cdot \mathbf{U} > 0$ goes to the origin. Nevertheless the other semi-plane moves away from the origin. When $k_x < 0$ and there is a current $\mathbf{U} \neq 0$, the curves decrease quickly, even changing the sign in its derivative and giving two possible solutions for $k_x < 0$ for the same ω. The second k_x solution is far away from the origin and useless for the ocean waves study. This effect with the current is represented in the figure 2.6.
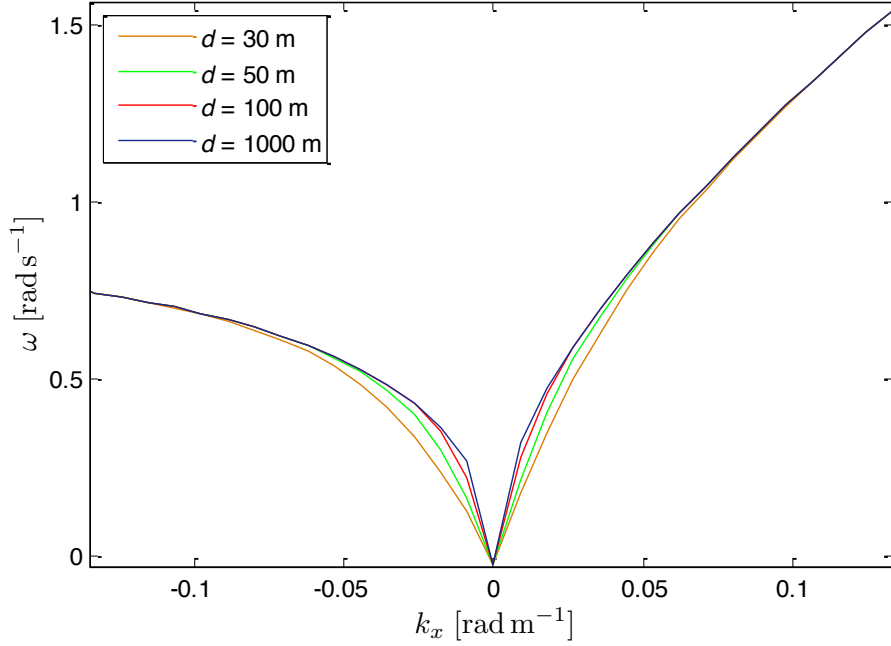
Figure 2.5: Dispersion shell transect $\omega = \varpi(k_x, 0)$ for different values of depth, being the current of encounter $\mathbf{U} = (3,\, 0)\,\mathrm{m\,s^{-1}}$.

- Depth effect

  The dependency of the dispersion function $\omega = \varpi(\mathbf{k})$ with depth is not so strong in comparison with the effects of the current $\mathbf{U}$. Figure 2.5 displays the relation between the dispersion shell and the water depth d. The reason for this weak dependency is due to the $\tanh(kd)$, because it approaches quickly to 1 as the product of kd is high enough.

2.3   Stochastic description of sea states

The real ocean waves are a complex chaotic physical phenomenon. Hence, the hydrodynamic theory (see appendix A) that derived the superposition given by (2.2) is a limited model to described the spatio-temporal properties of the sea surface elevation η. Therefore, it is necessary to add additional theoretical assumptions that permit a better description of the wave elevation of the free sea surface. Hence, assuming valid the frame of the linear wave theory, the theory of stochastic processes is taking into account as well. Under these considerations, the wave elevation $\eta(\mathbf{r}, t)$ is regarded as a stochastic process, which is a solution of the linearized wave hydrodynamic equations. From this stochastic approach the above mentioned concept of sea state arises. A sea state is defined as a wave field which is statistically stationary in time and homogeneous in space [4].

2.3.1 Spectral representation of sea states

Assuming the concept of sea state through the stochastic approach, to describe wave fields $\eta(\mathbf{r}, t)$ may be expressed by the following spectral representation [9]

$$\eta(\mathbf{r}, t) = \int_{\Omega_{\mathbf{k},\omega}} e^{j(\mathbf{k}\cdot\mathbf{r}-\omega t)} \, dZ(\mathbf{k}, \omega), \tag{2.5}$$

where each spectral monochromatic wave component is identified by its wave number $\mathbf{k}$ and angular frequency ω. The integration in equation (2.5) is defined in terms of a Riemann-Stieltjes integral [10], $dZ(\mathbf{k}, \omega)$ is known as *spectral random measure*, and it plays a similar role than the complex amplitude c_n in the expression (2.2). As $\eta(\mathbf{r}, t)$ is a real-valued process, $dZ(\mathbf{k}, \omega) = dZ^*(-\mathbf{k}, -\omega)$, where the upper index * indicates the complex conjugate. $dZ(\mathbf{k}, \omega)$ is a zero-mean complex Gaussian process, which are statistically uncorrelated for different wave components $(\mathbf{k}, \omega)$ [9]:

$$\mathsf{E}[dZ(\mathbf{k}, \omega)] = 0 \quad \forall\, (\mathbf{k}, \omega) \tag{2.6}$$

$$\mathsf{E}[dZ(\mathbf{k}, \omega)\, dZ^*(\mathbf{k}', \omega')] = 0 \quad (\mathbf{k}, \omega) \neq (\mathbf{k}', \omega') \tag{2.7}$$

where E is the expectation operator. The integration domain $\Omega_{\mathbf{k},\omega}$ in equation (2.5) is defined from the admissible range of wave numbers $\mathbf{k}$ and angular frequencies ω corresponding to ocean waves (i.e. wavelengths from 1 m to 300 m and wave periods from 0.5 s to less than 20 s approximately). In practice, the domain $\Omega_{\mathbf{k},\omega}$ is commonly limited by the spatio-temporal resolution of the measuring sensor. Hence $\Omega_{\mathbf{k},\omega}$ is regarded as the Cartesian product

$$\Omega_{\mathbf{k},\omega} = \Omega_{\mathbf{k}} \times \Omega_{\omega} \tag{2.8}$$

being

$$\Omega_{\mathbf{k}} = [-k_{x_c}, k_{x_c}) \times [-k_{y_c}, k_{y_c})$$

and

$$\Omega_{\omega} = [-\omega_c, \omega_c) \times [\omega_c, \omega_c)$$

where k_{x_c}, k_{y_c} and ω_c are the Nyquist limits for k_x, k_y and ω respectively.

Hence, taking into account the expression (2.5), the reconstruction of the sea surface illustrated in figure 2.2 can be understood as a superposition of different stochastic spectral components.

Assuming the model given by the equation (2.5), the wave elevation of the free sea surface η respect to a reference level is Gaussian distributed with mean $\mu_\eta = 0$ and standard deviation σ_η. Hence, the probability density function of η is given by

$$p(\eta) = \frac{1}{\sigma_\eta^2 \sqrt{2\pi}} e^{-\frac{\eta^2}{2\sigma_\eta^2}} \tag{2.9}$$

This model is useful for symmetric ocean waves, in deep water. In shallow waters ocean waves are asymmetrical (higher than deeper) and the Gaussian model (2.5) is not valid.

2.3.2   Three-dimensional wave spectrum

From the equation (2.5) the three-dimensional (3D) power spectral density (or 3D wave spectrum) is defined as [10]

$$F^{(3)}(\mathbf{k}, \omega) \, \mathrm{d}^2 k \, \mathrm{d}\omega = \mathsf{E}\left[\mathrm{d}Z(\mathbf{k}, \omega)\mathrm{d}Z^*(\mathbf{k}, \omega)\right] = \mathsf{E}\left[|\mathrm{d}Z(\mathbf{k}, \omega)|^2\right], \tag{2.10}$$

where $\mathrm{d}^2 k \equiv \mathrm{d}k_x \mathrm{d}k_y$. As η is a real-valued stochastic process, the spectral density $F^{(3)}$ presents an even dependence on the spectral variables $(\mathbf{k}, \omega)$

$$F^{(3)}(\mathbf{k}, \omega) = F^{(3)}(-\mathbf{k}, -\omega) \tag{2.11}$$

The spectrum $F^{(3)}(\mathbf{k}, \omega)$ must hold the dispersion relation (2.3). Figure 2.6 illustrates the 2D transect of the location of the $(\mathbf{k}, \omega)$ components of the wave field within the domain $\Omega_{\mathbf{k}, \omega}$.
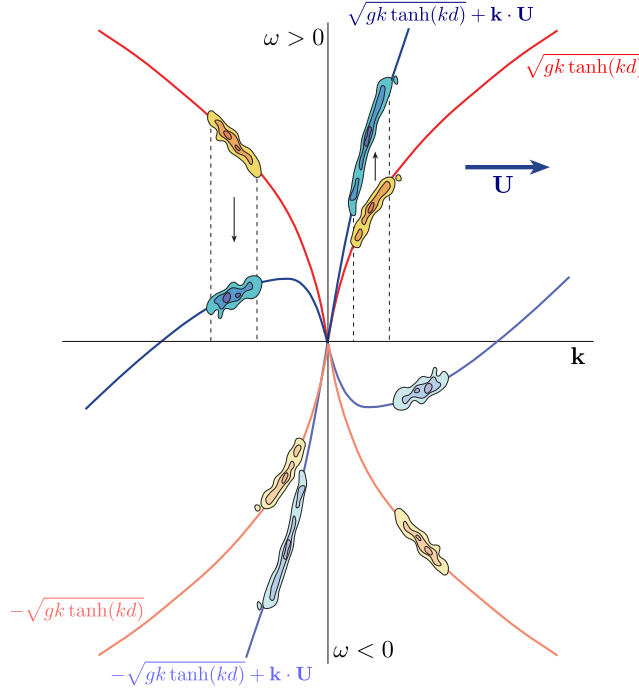
Figure 2.6: Two-dimesional example showing the distribution of the spectral wave components of the three-dimensional wave spectrum $F^{(3)}(\mathbf{k}, \omega)$ given by eq. (2.21) and the modifications due to the existence of a current $\mathbf{U}$. Adapted from [11].

The spectral density $F^{(3)}(\mathbf{k}, \omega)$ provides information about the amplitudes of the waves, but not about the phase lag between each wave spectral component. This phase is usually considered a random variable uniformly distributed in the interval $[-\pi, \pi)$. In addition, the spectral density $F^{(3)}(\mathbf{k}, \omega)$ describes the statistical and spectral properties of the stochastic process $\eta(\mathbf{r}, t)$ and it derives the variance of the wave elevation of the free sea surface associate with the spectral set

$[k_x, k_x + \mathrm{d}k_x) \times [k_y, k_y + \mathrm{d}k_y) \times [\omega, \omega + \mathrm{d}\omega)$. Furthermore, $F^{(3)}(\mathbf{k}, \omega)$ is related to the meteorological and dynamic condition of the wave field [6].

Considering the stochastic model described above in section 2.3 where the mean is equal to 0 and the standard deviation is the equation (2.9), it is possible to get the variance attending to the spectral density $F^{(3)}(\mathbf{k}, \omega)$:

$$\sigma_\eta^2 = \int_{\Omega_{\mathbf{k},\omega}} F^{(3)}(\mathbf{k}, \omega) \, \mathrm{d}^2 k \, \mathrm{d}\omega \tag{2.12}$$

Because of the mean $\mu_\eta = 0$, the standard deviation σ_η is equivalent to the root mean squared of the wave elevation of the sea state:

$$\eta_{rms} = \sigma_\eta = \sqrt{\mathsf{E}\left[\eta^2(\mathbf{r}, t)\right]} \tag{2.13}$$

2.3.3 Parameters obtained from the three-dimensional spectral density

The 3D spectral density $F^{(3)}(\mathbf{k}, \omega)$ is an important and useful magnitude. From $F^{(3)}(\mathbf{k}, \omega)$ other useful spectral parameters can be obtained, such as

- Spectral moments m_n:
  They inform about the ocean waves characteristics [6]. The spectral moment of order n^{th}, m_n, is defined as

$$m_n = \frac{1}{(2\pi)^n} \int_{\Omega_{\mathbf{k},\omega}} \omega^n F^{(3)}(\mathbf{k}, \omega) \, \mathrm{d}^2 k \, \mathrm{d}\omega \; ; \quad n = 0, \pm 1, \pm 2, \ldots \tag{2.14}$$

  For practical applications, the most relevant spectral moments are m_{-1}, m_0, m_1 and m_2 [4]. I.e. the zeroth order moment m_0 is used to estimate the significant wave height H_s, which is an important parameter to characterise wave fields, as well as for design of marine structures. Table 2.1 shows some of the wave heights and periods derived from the spectral moments.

- The mean energy density per unit area of sea state parameter $\overline{\xi}$ is written as [6]:

$$\overline{\xi} = \rho_w g \int_{\Omega_{\mathbf{k},\omega}} F^{(3)}(\mathbf{k}, \omega) \, \mathrm{d}^2 k \, \mathrm{d}\omega = \rho_w g m_0 \tag{2.15}$$

  being ρ_w the sea water density.

- Mean moment per unit of area [6]:

$$\overline{\mathcal{M}} = \int_{\Omega_{\mathbf{k},\omega}} F^{(3)}(\mathbf{k}, \omega) \frac{\mathbf{k}}{\omega} \, \mathrm{d}^2 k \, \mathrm{d}\omega \tag{2.16}$$

- Mean action per unit of area [6]:

$$\overline{\mathcal{A}} = \rho_\omega g \int_{\Omega_{\mathbf{k},\omega}} \frac{F^{(3)}(\mathbf{k}, \omega)}{\omega} \, \mathrm{d}^2 k \, \mathrm{d}\omega \tag{2.17}$$

- Mean constant of the movement: in general, from $F^{(3)}(\mathbf{k}, \omega)$ it is possible to construct a dynamic constant of the movement $\overline{\mathcal{I}_{\boldsymbol{\Gamma}}}$ as [6]

$$\overline{\mathcal{I}_{\boldsymbol{\Gamma}}} = \int_{\Omega_{\mathbf{k},\omega}} F^{(3)}(\mathbf{k}, \omega)\boldsymbol{\Gamma}(\mathbf{k}, \omega)\, \mathrm{d}^2 k \, \mathrm{d}\omega \tag{2.18}$$

where the function $\boldsymbol{\Gamma}(\mathbf{k}, \omega)$ can be a vector or a scalar magnitude.

Table 2.1: Wave heights and periods got from moments of the wave spectrum

Significant wave height	$H_S = 4.004\sqrt{m_0}$
Mean wave height	$\bar{H} = 2.507\sqrt{m_0}$
Root-mean-squared wave height	$H_{rms} = 2.828\sqrt{m_0}$
Period of the energy	$T_e = m_{-1}/m_0$
Mean period ($m01$-estimator)	$T_{m01} = m_0/m_1$
Mean period ($m02$-estimator)	$T_{m02} = \sqrt{m_0/m_2}$

2.3.4   Alternative spectral representations

Based on three-dimensional spectral density $F^{(3)}(\mathbf{k}, \omega)$, various forms of spectral densities can be obtained [12]. All of these must preserve the variance σ_η^2 (i.e. preserving the total volume of the spectrum).

1. Frequency spectrum $S(\omega)$: It depends only on the angular frequency ω, which is associated with the time dependence of sea state. It is useful to analyse the measurements of the anchored buoys:

$$S(\omega) = \int_{\Omega_{\mathbf{k}}} F^{(3)}(\mathbf{k}, \omega)\mathrm{d}^2 k \tag{2.19}$$

2. Directional spectrum: In this case, there is a directional vector associated to the spectra, in Cartesian or Polar coordinates.

   - Unambiguous wave number spectrum $F^{(2)}(\mathbf{k})$:
     This spectral density function is obtained integrating three-dimensional spectral density $F^{(3)}(\mathbf{k}, \omega)$ over the set of positive frequencies $\omega \geq 0$.

$$F^{(2)}(\mathbf{k}) = 2 \int_0^{\omega_c} F^{(3)}(\mathbf{k}, \omega)\, \mathrm{d}\omega \tag{2.20}$$

     Under the assumption of linear wave theory and taking into account the dispersion relation (see equation (2.3)), the three-dimensional wave spectrum can be written from $F^{(2)}(\mathbf{k})$ as (see figure 2.6):

$$F^{(3)}(\mathbf{k}, \omega) = \frac{1}{2}\left[F^{(2)}(\mathbf{k})\delta(\omega - \varpi(\mathbf{k})) + F^{(2)}(-\mathbf{k})\delta(\omega + \varpi(-\mathbf{k}))\right] \tag{2.21}$$

     Therefore, the spectral components are distributed in the $\Omega_{\mathbf{k},\omega}$ domain with the dispersion shell defined by the dispersion relation $\omega = \varpi(\mathbf{k})$.

- Wave number spectrum in polar coordinates $\widetilde{F}^{(2)}(k,\theta)$:
  If it considers the Polar coordinates given by k and the propagation direction θ of each wave component:

$$\widetilde{F}^{(2)}(k,\theta) = F^{(2)}(\mathbf{k}(k,\theta))k \tag{2.22}$$

  where k is the Jacobian needed from the coordinate transform $(k_x, k_y) \mapsto (k,\theta)$.
  From $\widetilde{F}^{(2)}(k,\theta)$ the one-dimensional wave number spectrum $F(k)$ is derived by integrating $\widetilde{F}^{(2)}(k,\theta)$ over all the wave propagation directions θ:

$$F(k) = \int_{-\pi}^{\pi} \widetilde{F}^{(2)}(k,\theta) \, \mathrm{d}\theta \tag{2.23}$$

- Directional spectral density $E^{(2)}(\omega,\theta)$:
  If in the above expression the dispersion relation $\omega = \varpi(\mathbf{k})$ is imposed, the directional spectral density $E^{(2)}(\omega,\theta)$ is obtained as

$$E^{(2)}(\omega,\theta) = \widetilde{F}^{(2)}(k(\omega),\theta)\frac{\mathrm{d}k}{\mathrm{d}\omega} \tag{2.24}$$

  where $\mathrm{d}k/\mathrm{d}\omega = v_g^{-1}$ is the Jacobian needed for the transformation $k \mapsto \omega$. From the equation (2.24), the scalar spectrum $S(\omega)$ can be got again by integrating over all directions:

$$S(\omega) = \int_{\pi}^{\pi} E^{(2)}(\omega,\theta) \, \mathrm{d}\theta \tag{2.25}$$

The $E^{(2)}(\omega,\theta)$ function can be factored as follow:

$$E^{(2)} = S(\omega)D(\omega,\theta) \tag{2.26}$$

where $D(\omega,\theta)$ is the so-called *directional spreading function* [4].

The figure 2.7 shows the different spectral measurements commented above.

$$F^{(3)}(\mathbf{k}, \omega)$$

$$S(\omega) = \int_{\Omega_{\mathbf{k}}} F^{(3)}(\mathbf{k}, \omega) \mathrm{d}^2 k$$

$$F^{(2)}(\mathbf{k}) = 2 \int_0^{\omega_c} F^{(3)}(\mathbf{k}, \omega) \mathrm{d}^2 k$$

$$\tilde{F}^{(2)}(k, \theta) = F^{(2)}(\mathbf{k}(k, \theta)) k$$

$$E^{(2)}(\omega, \theta) = \tilde{F}^{(2)}(k(\omega), \theta) \frac{\mathrm{d}k}{\mathrm{d}\omega}$$

$$S(\omega) = \int_{-\pi}^{\pi} \tilde{E}^{(2)}(\omega, \theta) \mathrm{d}\theta$$
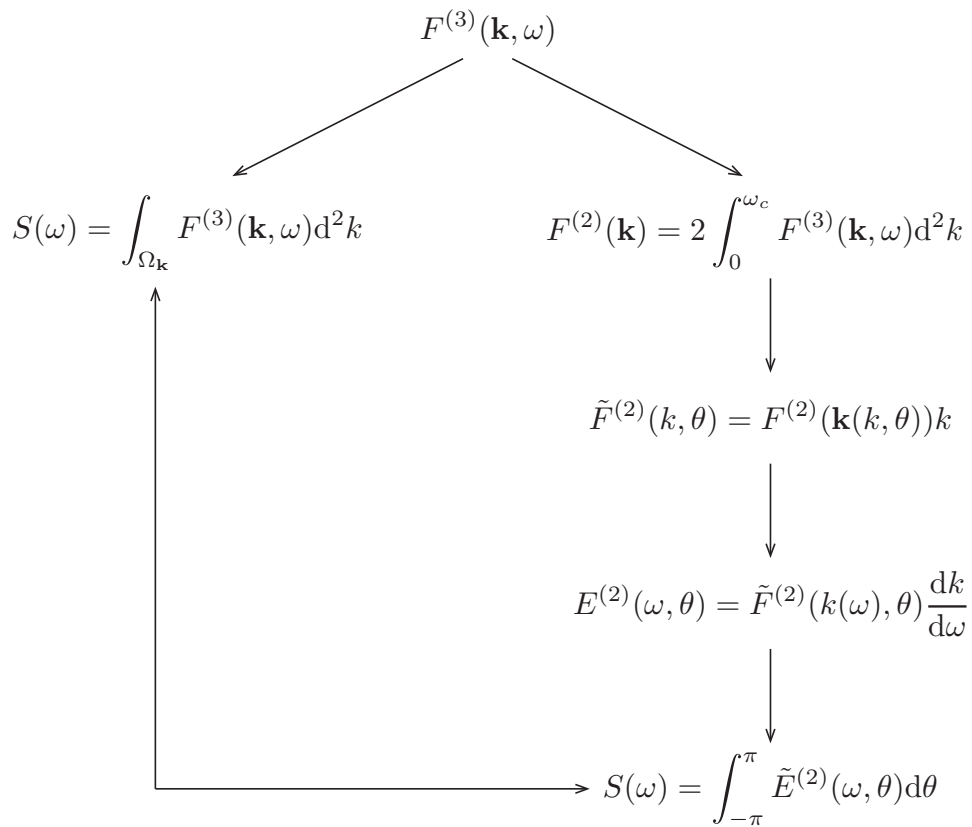
Figure 2.7: Dependence among the different spectral densities defined from sea state. Adapted from [12]

Chapter 3

Marine Radar Image Processing

The radar transmits electromagnetic signals towards the sea surface and the echoes are received by the receiving antenna of the radar. The marine radar measures the roughness of the sea surface and the roughness is related to the existence of wind in the sea state. The marine radar images not only depend on wind, but there are more factors that affect the images such as physico-chemical properties of the sea water [13]. Firstly, the radar theory and the main common characteristics are going to be presented, to focus lately in the marine radar and in the processes to manage the radar images.

3.1 Brief description of the pulsed radar theory

The term Radar is an acronym of English words *Radio Detection And Ranging.* Radar is an electromagnetic system that can detect and locate moving or static objects. The radar is not capable to distinguish well-defined features, like colour or shape, but however the radar can detect targets, giving its position all the time, in adverse conditions such as rain, fog and snow. The first use of the radar was in the Second World War to detect enemy airplanes. Nowadays it is used on countless daily activities. The radar emits a certain type of electromagnetic wave, focused on a very narrow beam. This electromagnetic wave is reflected in all directions by the target, but only the echo signal sent back in the radar direction is important. For a pulsed radar, the transmitted electromagnetic wave is usually a narrow rectangular pulse train. When the radar emits a pulse, it must wait long enough time to receive the echo signal before emitting the next pulse. The time between pulses is determined by the desired maximum range. The wave reflection changes according to the electromagnetic wavelength λ_{em} and the shape and roughness of the target. If the wavelength λ_{em} is smaller than the size of the target, the electromagnetic wave will bounce. However, if the wavelength λ_{em} is bigger than the target, the electromagnetic wave will polarize. Nevertheless, military planes use magnetic substances that absorb the electromagnetic radar waves, reducing the reflection [13, 14].

The diagram shown in figure 3.1 shows the performance of a radar. Transmitter is the main element of the radar. The synchronizer generates a series of narrow pulses with a particular
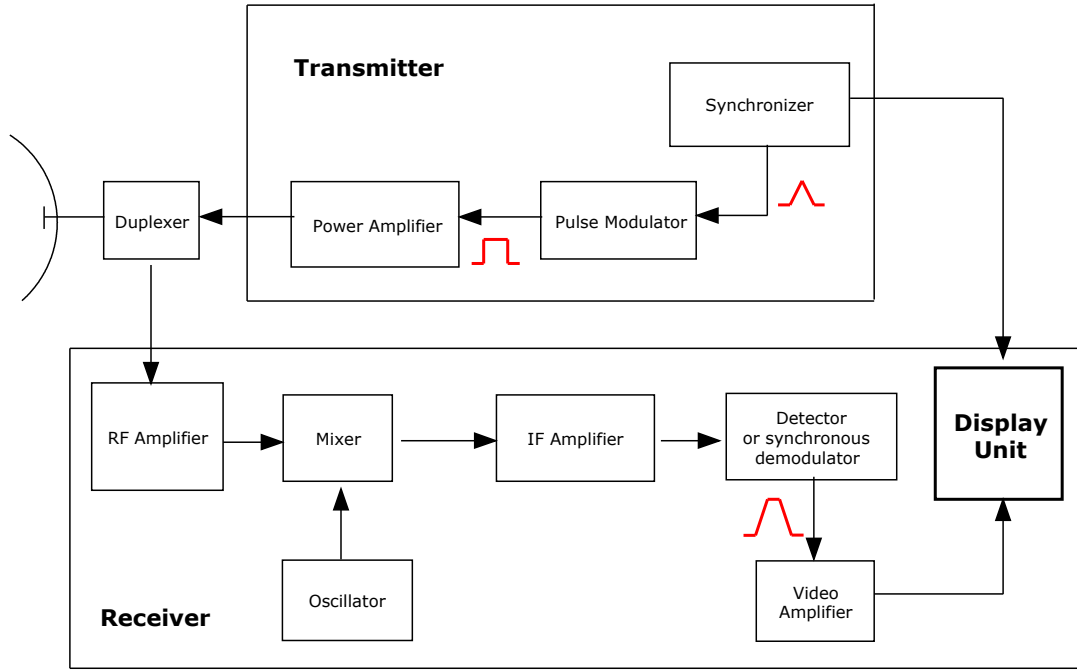
Figure 3.1: Scheme of a radar system.

pulse repetition frequency, these pulses excite a modulator, which triggers the transmitter. This modulated pulse travels along the transmission line to the antenna, which is radiated to space. The mission of the duplexer is to protect the receiver from the damage caused by the high power transmitter. Also it directs the returning echo to the receiver and not to the transmitter. Some receivers have a first stage with a radio frequency amplifier (RF). In the second stage is used a mixer and an oscillator to convert the RF signal to an intermediate frequency signal (IF). The signal is filtered to be further amplified by a video amplifier, getting a suitable level for the display unit.

3.1.1   Radar characteristics

The main characteristics of a common radar are:

- *Range R*: R is the distance between the object and the transmitter. It is calculated by measuring the time τ that a pulse needs to reach the object and back to the receiver. Therefore, the range is given by the expression:

$$R = \frac{c\,\tau}{2} \tag{3.1}$$

where c is the speed of light ($c \approx 3 \cdot 10^8$ m s^{-1}). Thus, if the next pulse is emitted without receiving the echo pulse corresponding to the previous pulse, there will be ambiguities in the range measurement.

- Maximum unambiguous distance: When the radar emits a pulse, the radar waits the echo signal before the radar transmits the next pulse. If the *pulse repetition frequency* f_{PRF} is high, the echo signal could come back later than the next pulse emitted by the radar. The echoes which arrive to the radar later than the next pulse are called *Second-time-around echoes*. These echoes would be shorter and closer than the real measurement and they could occasion several mistakes. The maximum unambiguous distance is the more distant distance in which the echoes are *second-time-around echoes*, and this distance could be written as:

$$R_{un} = \frac{c\,T_{PRF}}{2} = \frac{c}{2\,f_{PRF}} \tag{3.2}$$

Where T_{PRF} is the pulse repetition period and f_{PRF} is the pulse repetition frequency. Therefore, a good detection in short and far range simultaneously is difficult. To detect in short range the pulse must be small and low power

- The emitted signal: It is usually a narrow rectangular pulse train. The mean power of the rectangular pulse train is:

$$P_{av} = \frac{\tau\,P_t}{T_{PRF}} = P_t\,\tau\,f_{PRF} \tag{3.3}$$

Where τ is the width of the pulse and P_t is the power emitted by the transmitter.

- Radar resolution: It provides the minimum distance between two targets for which is possible seeing the two targets separately. There are two different resolutions:

  - Range resolution: It is a radial resolution and is related to the width of the pulse τ emitted by the radar. Therefore, there will be an error in range ΔR:

$$\Delta R = \frac{c\,\tau}{2} \tag{3.4}$$

    If the width of the pulse τ is small, the range resolution will be better. But the value of τ is restricted and it could not be very small because the received power will decrease a lot.

  - Azimuth resolution: It is a resolution tangential to the antenna rotation direction and it is related to the horizontal width of the radar beam.

The main signals that take part in a radar system are:

- Signal: It is the desirable signal reflected by the target.

- Clutter: It is the unwanted echoes. Such echoes are typically returned from ground, sea, rain, animals, atmospheric turbulence, and can cause serious performance issues with radar systems.

- Noise: It is a non-desired electromagnetic signal that interferes in the receiver overlapping to the signal. The noise is aleatory and it could come from environmental source or even the electrical devices in the receiver.

The electromagnetic waves broadcast by the radar antennas are in the microwave domain. Table 3.1 collected the typical radar bands.

Table 3.1: Radar working band frequencies f_{em} and wavelengths λ_{em} in the microwave domain.

Band	Frequency f_{em} [GHz]	Wavelength λ_{em} [cm]
P-band	0.225 - 0.39	133 - 77
L-band	0.39 - 1.55	77 - 19
S-band	1.55 - 3.90	19 - 7.7
C-band	3.90 - 6.20	7.7 - 4.8
X-band	5.75 - 10.9	5.2 - 2.8
K_u-band	10.9 - 18.0	2.8 - 1.7
K-band	18.0 - 26.50	1.7 - 1.13
K_a-band	26.50 - 36.0	1.13 - 0.8
V-band	36.0 - 75.0	0.8 - 0.4
W-band	75.0 - 110.0	0.4 - 0.27

3.1.2 Radar equation

The radar equation relates the range R to the characteristic of the transmitter, the receiver, the antenna, the target and the environment. This equation allows for understanding the main factors that affect the efficiency of the radar. It is supposed that the antenna is an isotropic antenna, emitting in all directions a uniform power P_t. The *power density* registered in a point of distance R is:

$$\wp = \frac{P_t}{4\pi R^2} \tag{3.5}$$

The units of the power density are [W m^{-2}]. But it is an ideal situation, because in real life the antennas are not isotropic and they focus the energy in some directions to detect better the targets. The *gain of the antenna* or the *gain* describes how well the antenna converts input power into radio waves headed in a specified direction with respect to an isotropic one. Therefore, the power density radiated using a directive antenna with gain G can be rewritten as:

$$\wp = \frac{P_t G}{4\pi R^2} \tag{3.6}$$

The target blocks a part of the incident energy and reflects it in some directions. The *Radar Cross Section* (RCS), denoted σ as well, assesses the power density which returns to the radar depending on the incident power density on the target. Its unit is [m^2]. However, the RCS is not related to the physical size of the target, but the shape of the target. In theory, the received signal from a target is constant in time, but in fact the echo is never constant. These variations are due to the meteorological conditions, the antenna radiation diagram or changes in the RCS. Therefore the power reflected by the target is:

$$P_{\text{target}} = \sigma \wp = \sigma \frac{P_t \, G}{4\pi R^2} \tag{3.7}$$

The power density reflected by the target in the receiver direction is:

$$\wp_r = \frac{P_t \, G \, \sigma}{(4\pi)^2 R^4} \tag{3.8}$$

The receiving antenna is usually the same that the antenna used in broadcast. Due to reciprocity, the gain of any antenna when receiving is equal to its gain when transmitting. The receiving antenna takes a portion of the energy that reaches the receiving antenna. The *antenna aperture* or *effective area*, A_{eff}, is a measure of how effective an antenna is at receiving the power of radio waves. The effective area is the multiplication of the area of the antenna A and its efficiency η, so $A_{\text{eff}} = A \cdot \eta$. Therefore, the power received for the radar in watts [W] will be:

$$P_r = \wp_r \, A_{\text{eff}} = \frac{P_t \, G \, \sigma \, A_{\text{eff}}}{(4\pi)^2 \, R^4} \tag{3.9}$$

There is a maximum range where the targets can not be detected. This restricted distance is represented by $R_{\max}$ and at this point the power received by the radar from the echo P_r is equal to the minimum signal detectable $S_{\min}$ by the radar or *sensitivity*, therefore:

$$R_{\max} = \left[\frac{P_t \, G \, \sigma \, A_{\text{eff}}}{(4\pi)^2 \, S_{\min}} \right]^{\frac{1}{4}} \tag{3.10}$$

The equations (3.9) and (3.10) are the main equations to characterise a radar. But there are other possible ways to represent the maximum range if the gain of the antenna is considered like:

$$G = \frac{4\pi \, A_{\text{eff}}}{\lambda_{\text{em}}^2} \tag{3.11}$$

Where λ_{em} is the wavelength of the electromagnetic signal of frequency f_{em} (i.e. $\lambda_{\text{em}} = c/f_{\text{em}}$). Therefore, the maximum range is expressed as:

$$R_{\max} = \left[\frac{P_t \, G^2 \, \sigma \, \lambda_{\text{em}}^2}{(4\pi)^3 \, S_{\min}} \right]^{\frac{1}{4}} \tag{3.12}$$

$$R_{\max} = \left[\frac{P_t \, A_{\text{eff}}^2 \, \sigma}{4\pi \, \lambda_{\text{em}}^2 \, S_{\min}} \right]^{\frac{1}{4}} \tag{3.13}$$

3.2 The marine radar

Marine radars often work in X or S band. The X-band has a higher resolution and greater sensitivity to the capillary waves caused by the wind. S-band is less effective than X because
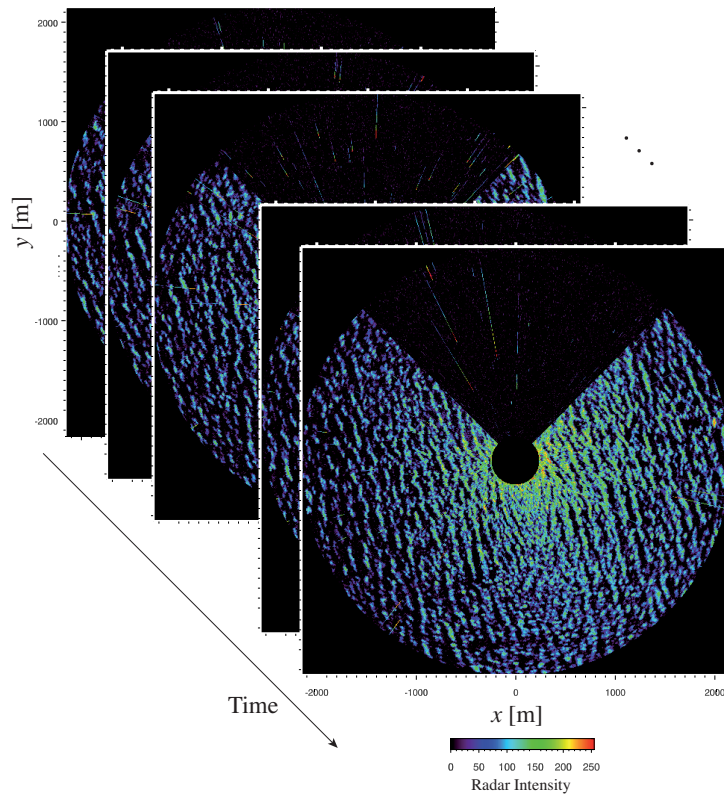
Figure 3.2: Example of temporal sequence of sea clutter images taken by FINO 1 platform.

S-band needs more local wind. This type of radar uses horizontal polarization, both in emission and reception. Marine radars have an incoherent logarithmic amplifier and they lack frequency agility. The main limitation of marine radar consists of the range, in the area in which the wave height measurements are carried out, is less than other radars. The electromagnetic fields generated in the sea surface are the sources that create the radar images on the display unit. In case of studying the ocean free surface, the radar image provided by the display unit is the right one. However, if the study is focus in particular targets, the energy coming from the sea surface is considered as a *sea clutter* or even noise for other purposes like coastal surveillance, and the intensity of the sea clutter is low. So the signal in which is going to be focused this work is in this low power signal come from the sea surface.

The values of the image are coded in different grey levels, which depend on the specific configuration that the radar has in a certain moment. Therefore, it cannot know absolute values of parameters related to the return electromagnetic energy, such as backscatter.

In marine radar, the transmitter spins around with constant speed. The typical speed for these transmitters is between 20 and 30 r.p.m. The rotation of the antenna is synchronised with the display unit, therefore the relative direction of a particular target can be known. Most of the marine radar systems incorporate a compass signal, which is useful to refer all the directions with the geographic North.

The marine radar needs roughness in the sea surface, because if sea is completely flat and calm, the electromagnetic waves emitted by the radar will be reflected like a mirror without echoes coming back the receiving antenna. The roughness is owing to the capillary waves, which are produced by the local wind and the existence of sea foam [15]. But the roughness is altered by other phenomena such as chemical substance in the water, currents, waves originating from wind sea and whatever phenomenon that affects the grouping and the shape of the capillary waves. In [15] it is commented that final radar images consider the energy scattered by the capillary waves and the modulation of other anomalies developed on the sea surface, which will be presented in 3.3.

3.2.1 WaMoS II System

WaMoS II system (*Wave Monitoring System*) is a high-speed video digitalization and storage device that can operate with any conventional navigation radar X-band. It is marketed by the German company *Ocean Waves GmbH* to take measurements of the wave spectrum in real time. Its main advantage lies in the continued availability of data with the sea rough, severe weather and at night. It can also be installed in both ground stations and on ships.
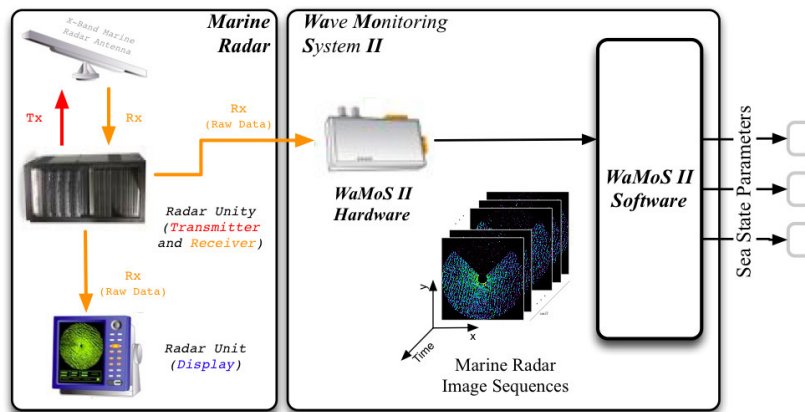
Figure 3.3: Scheme of a WaMoS II installation.

The figure 3.3 shows the measuring system, that consists of a conventional navigation radar, a high-speed video digitizer, and a standard computer. The analogue radar video signal is read out and digitised into a scale 256 grey levels. This information is transferred and stored on a computer where the wave analysis software carries out the computation of the sea state parameters in real time. The system uses three signals from X-band radar to determine the parameters of waves and surface currents in near real time. These signals are: the *video signal*, which is converted to digital data useful for the computer, the *trigger signal* used to sample the data and the *heading signal* that indicates when the antenna passes through the origin of rotation. The software of

the system controls the radar, data storage and presentation of them. The system generates text files according to the coordinates. But the main drawback is that WaMoS is effective when the wave height exceeds one meter. The measures are based on the backscatter from the sea surface. The backscatter shows the propagation patterns followed by waves and it determines the structure of the ocean clutter.

3.3 Physical phenomena in the marine radar imaging

The final image shows by the radar is not a direct mapping image of the ocean surface. The image displays the energy scattered by the sea surface and the addition of another energy due to other still not well-known phenomena, which distort the free ocean surface images. Some of these phenomena modulate the electromagnetic backscatter inducing additional modulations:

- Wave tilt modulation: It is related to the effective slopes of the waves. The incident angle θ_0 of the electromagnetic radiation changes with respect to the plane of the wave slope considered at the scale of the spatial resolution. Because of this, the facets orientated close to the antenna direction produce higher backscatter than the others. Therefore, additional spectral components are introduced in domain of high wave numbers $\mathbf{k}$, increasing the spectral energy for those high wave numbers $\mathbf{k}$ [16, 15]. So this modulation depends on the position of the radar antenna and the slope of the waves, being very important in marine radars.

- Hydrodynamic modulation: This modulation is related to the interaction of the capillary waves (which are affected by the surface tension) and the long waves. The most of the capillary waves are inner surface of the long waves and they propagate faster for shorter wavelengths. For this reason, the electromagnetic energy dispersion is modified, but for marine radars this distortion is not so strong.

- Orbital modulation: It is caused by the motion of particles of the water during the time in which the wave is under the radar beam. This modulation is very important for *Synthetic Aperture Radar* (SAR), or Doppler radars in general which are more sensitive with the movements of the targets.

- Shadowing modulation: It happens when the higher waves hide the lower waves from the radar beams. This effect introduces in the radar image spectrum additional components of high wave number $\mathbf{k}$ and frequency ω, and it is stronger when the angle of incidence of the radar beam on the ocean surface is near to 90º. This modulation has a very impact in marine radars because the height of the antenna over the sea is small [15].

All of these modulations spoil the spectra of the radar images introducing noise for frequencies greater than or equal to *peak frequency* f_p, that is the frequency related to the spectral maximum.

These phenomena are not the unique effects that distort the spectrum. The final radar image depends, as well, on:

Shadowing Modulation

Radar Antenna

Sea Level

Shadowed Areas

Tilt Modulation

$\theta_0 > \theta_0'$

θ_0

θ_0'

Hydrodynamic Modulation

Wave Direction

Orbital Modulation
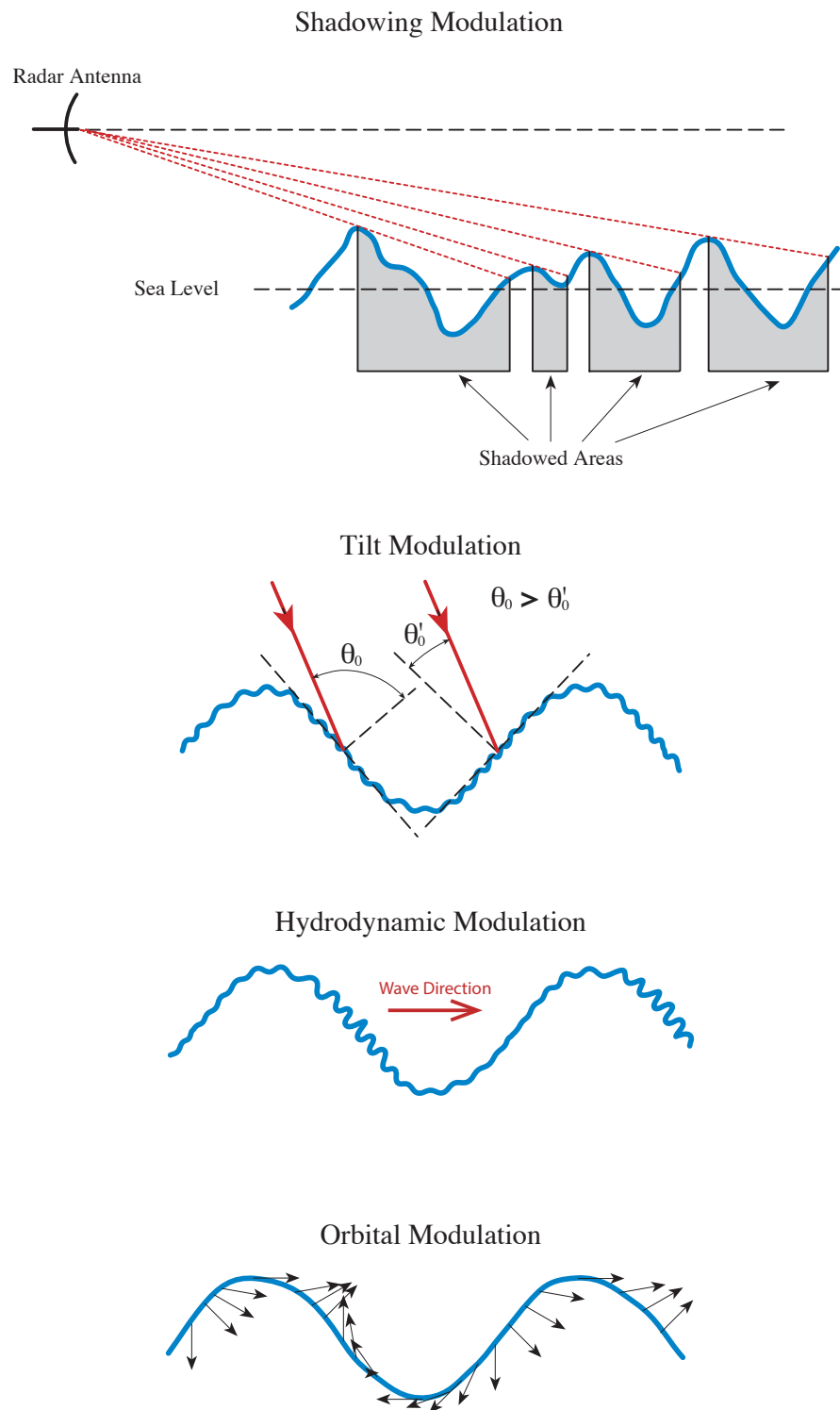
Figure 3.4: Modulations of the interaction of the electromagnetic waves with free sea surface [15].

- Range dependence: The more far away from the radar, the weaker the signal is. The power received by the radar is inversely proportional to the distance between the target and the

radar. So for far range, the intensity of the signal is faint. Therefore, this dependence introduces a no-homogeneous and static pattern in the radar wave spectrum [9].

- Azimuthal dependence with the wind direction: The wind action is very important because the intensity of the images depends on the wind direction. The return is greater in the direction where the wind is coming from [17].

- Azimuthal dependence with the wave propagation direction: The radar wave image is stronger up and down wave than perpendicular to the wave propagation direction [18].

- Wind speed dependence: When the wind grows, the image intensity increases [17].

All phenomena insert in the image spectrum additional $(\mathbf{k}, \omega)$ components, which do not belong to the wave field. The shadowing and tilt modulations introduce additional energy in high wave numbers and frequencies. However, the range dependence causes a static pattern in the sea clutter time series producing a high spectral energy in the low frequency domain.

3.4   Wave spectrum estimation from the radar images

In marine radars, the main technique to analyse wave fields is based on the acquisition of a temporal sequence of N_t consecutive images of the ocean clutter. The antenna rotation period is that provides the sampling time Δt of the time sequence of images. While the spatial resolution (Δx and Δy) of each image depends on the azimuth and range resolution of the radar system. These images are provided by the WaMoS II system.
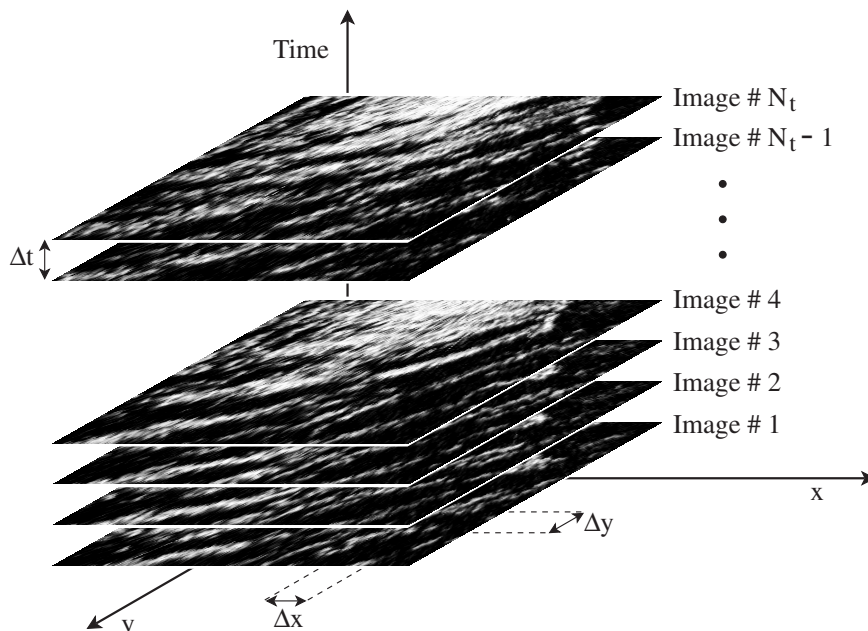
Figure 3.5: Example of marine radar data set (adapted from [11]).

The measurement of ocean waves with marine radars is based on the spatial and temporal structure analysis of the sea surface radar images. These radar images are caused by the interaction of the electromagnetic waves transmitted by the radar antenna with the sea surface ripples caused by the local wind [11, 19, 20, 21]. This interaction produces a backscatter of the electromagnetic fields and, therefore, an image pattern in the radar display unit. This image pattern is commonly known by sailors as *sea clutter*, and it is considered as noise for navigation purposes. However, in this study it will not be considered as noise. Hence, using temporal sequences of consecutive sea clutter images, the spatial and temporal variability of the sea surface is analised to estimate wave field spectral properties [22, 23], as well as related sea state parameters. But there are some phenomena that affect the dispersion of electromagnetic fields by the ripples. These effects produce modulations and signal distortion, introducing noise and spoiling the spectrum, that causes that the radar return is not a true and direct sea surface image, which should be considered in the radar image. These phenomena are presented before in the section 3.3.

Applying the three-dimensional Fourier decomposition of the sea clutter time series, the so-called *three-dimensional image spectrum* $F_\psi^{(3)}(\mathbf{k}, \omega)$ is obtained. The different radar imagery phenomena can be identified in the $(\mathbf{k}, \omega)$-components of $F_\psi^{(3)}(\mathbf{k}, \omega)$.

The figure 3.6 shows an example of image spectrum estimated from a temporal sequence of radar images measured in the Northern Coast of Spain.

These phenomena are generally nonlinear, causing distortion and signal modulation, introducing noise, especially in high wave numbers. This brings out additional components which do not belong to the image of the radar wave field.

Therefore, the wave spectrum estimation is carried out by using *the inversion modelling technique* of time series of images provided by the WaMoS II system and the analysis of *the spectral density of background noise* (BGN), providing additional information to the inverse modelling technique.

3.4.1 Analysis of ocean waves from temporal sequences of X-band radar images of the sea surface

It is a well known the fact that in the near range of ordinary X-band marine radars, the sea surface ripples induced by the local wind produce a strong radar signal. Electromagnetic fields are broadcast by the transmitting antenna and these ripples cause a backscatter of these electromagnetic fields, received by the receiving antenna. Furthermore, the backscattering pattern is modulated by long ocean waves, such as swell or wind sea. As a result of all those phenomena, a strong radar signal can be observed in the radar screen. This signal is commonly known by radar operators as *sea clutter* and is an undesirable effect for navigation purposes. But if the purpose is the study of waves, ocean behaviour, currents, etc. this *sea clutter* will be the right signal and the center of the study. On the other hand, the temporal evolution of
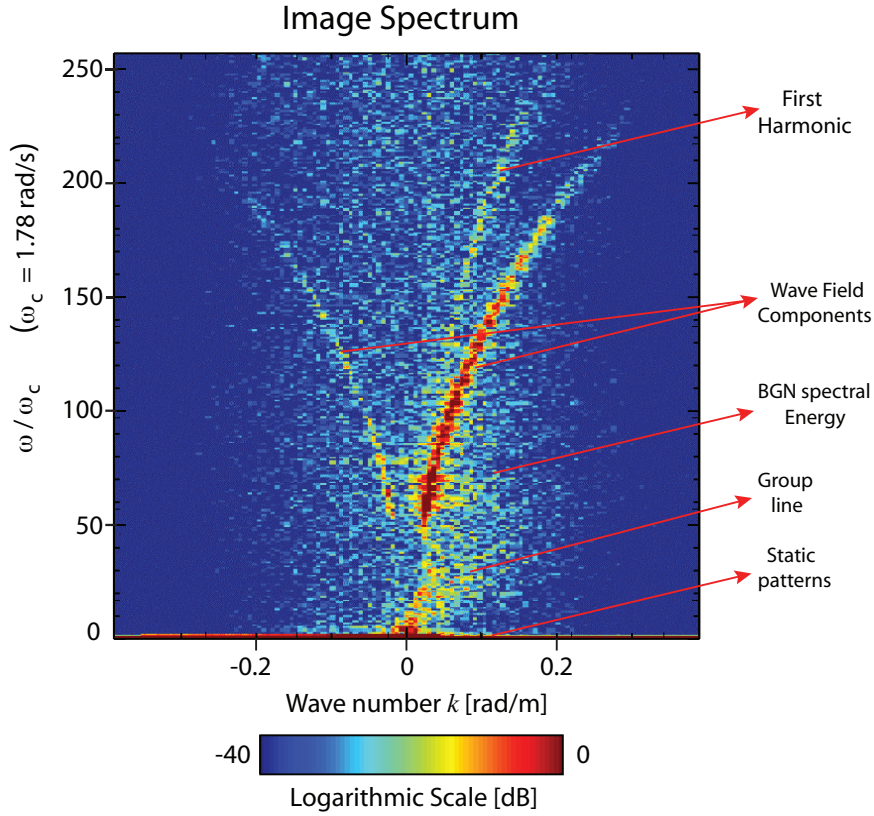
Figure 3.6: Example of image spectrum. The plot corresponds to a two-dimensional transect $(\mathbf{k_p}, \omega)$, where $\mathbf{k_p}$ indicates the wave number vector projection along the wave propagation direction (adapted from [24]).

the sea clutter contains information about the sea surface and its evolution in space and time. Therefore, the analysis of temporal sequences of radar images of the sea surface can be used to analyse ocean wave fields.

3.4.2 Inversion modelling technique

The digitised data are transformed into the spectral domain by means of a three-dimensional discrete Fourier transform to estimated the image spectrum $F_{\psi}^{(3)}(\mathbf{k}, \omega)$. Once the three-dimensional image spectrum $F_{\psi}^{(3)}(\mathbf{k}, \omega)$ is calculated, the inversion modelling technique can be applied. In [23, 24] this technique is presented and follows these steps:

1. Applying a low-pass filter
   $F_{\psi}^{(3)}(\mathbf{k}, \omega)$ needs to be filtered to eliminate the non-stationary and non-homogeneous trends in the radar image time series. For practical applications, the threshold frequency of the high-pass filter is $\omega_{\text{th}} = 2\pi \cdot 0.04$ rad s^{-1} because of lower frequencies may not be considered

as swell or wind sea. The transfer function of the filter is:

$$\mathcal{F}_{\text{th}}(\mathbf{k}, \omega) = \begin{cases} 0 & \text{if } (\mathbf{k}, \omega) \in \Omega_{\text{th}} \\ 1 & \text{otherwise} \end{cases} \tag{3.14}$$

$$F_{\text{th}}^{(3)}(\mathbf{k}, \omega) = F_{\psi}^{(3)}(\mathbf{k}, \omega) \mathcal{F}_{\text{th}}(\mathbf{k}, \omega), \tag{3.15}$$

where Ω_{th} is the set in the three-dimensional spectral domain and is defined:

$$\Omega_{\text{th}} = \{\mathbf{k} \mid k \leq \kappa(\omega_{\text{th}})\} \times [-\omega_{\text{th}}, \omega_{\text{th}}] \tag{3.16}$$

where $\kappa(\omega_{\text{th}})$ denotes the wave number solution of the dispersion relationship without current for the frequency ω_{th}. Now, the image spectrum $F_{\psi}^{(3)}(\mathbf{k}, \omega)$ has not got the non stationary spectral energy. The two main effects considered in low frequency are the static patterns originated by the long range dependence on the sea clutter images, and the *group line*. The group line is due to the intermodulations between different wave field components and it will be one of the targets to be studied in this work.

2. Estimation of the current of encounter
   The estimation of the current of encounter $\mathbf{U} = (U_x, U_y)$ is not a superficial current, but the weighted average of the all currents existing in the superficial layer of the ocean affected by the wave dynamics, and the distribution of the energy of the $(\mathbf{k}, \omega)$-spectral components of the wave field [15]

$$\mathbf{U} = \frac{2}{\sigma_\eta^2} \int_0^{k_c} \int_{-d}^0 F(k) \, k \, \mathbf{U}_{\text{layer}}(z) \, \mathrm{e}^{2kz} \, \mathrm{d}z \, \mathrm{d}k \tag{3.17}$$

where z is the vertical variable associated to the depth, $\mathbf{U}_{\text{layer}}(z)$ is the superposition of different effects as relative motion between the observer and the wave field $\mathbf{U}_{\text{rel}}(z)$, induced current produced by tides $\mathbf{U}_{\text{tid}}(z)$, the current produced by wind $\mathbf{U}_{\text{wind}}(z)$, the current introduced by the wave field $\mathbf{U}_{\text{wave}}(z)$ and other currents associated by the oceanic circulation $\mathbf{U}_{\text{ocean}}(z)$

$$\mathbf{U}_{\text{layer}}(z) = \mathbf{U}_{\text{rel}}(z) + \mathbf{U}_{\text{tid}}(z) + \mathbf{U}_{\text{wind}}(z) + \mathbf{U}_{\text{wave}}(z) + \mathbf{U}_{\text{ocean}}(z) \tag{3.18}$$

The estimation of the current $\mathbf{U}$ from three-dimensional spectrum of the image $F_{\psi}^{(3)}(\mathbf{k}, \omega)$ is based on considering spatial points $(\mathbf{k}, \omega)$ in which spectrum energy is important. Therefore, the energy due to the wave field is only considered, refusing the spectral noise produced by the radar when the images are generated. N_r points $(\mathbf{k}, \omega)$ will be selected, and all of them will have an energy higher than 20% of the maximum value of $F_{\psi}^{(3)}(\mathbf{k}, \omega)$

$$(k_{x_n}, k_{y_n}, \omega_n) \quad ; \qquad n = 1, 2, \ldots, N_r \tag{3.19}$$

$$\omega_n - \varpi_0(k_{x_n}, k_{y_n}) = k_{x_n} U_x + k_{y_n} U_y \tag{3.20}$$

where ϖ_0 denotes the so-called intrinsic frequency, i.e. the dispersion relation (2.3) without current of encounter $\mathbf{U}$.

The current of encounter $\mathbf{U}$ can be estimated by minimizing the functional [23]:

$$\mathcal{V} = \sum_{n=1}^{N_r} [\omega_n - \varpi_0(k_{x_n}, k_{y_n}) - k_{x_n} U_x - k_{y_n} U_y]^2 \tag{3.21}$$

3. Filtering the spectral energy due to the dispersion shell

   The marine radar measurement introduces an additional energy in the three-dimensional spectral density, therefore the dispersion relation (2.3) does not check. It is necessary to apply a three-dimensional band-pass filter in the $(\mathbf{k}, \omega)$ domain to take only the wave field components which belong to the wave field [23, 8]. The energy related to waves must comply with the equation (2.3). So the three-dimensional spectral density $F_F^{(3)}(\mathbf{k}, \omega)$ is obtained as

$$F_F^{(3)}(\mathbf{k}, \omega) = \int_{\Omega_{\mathbf{k},\omega}} F_{th}^{(3)}(\mathbf{k}', \omega')\, \delta(\mathbf{k}' - \mathbf{k})\, \delta(\omega' - \varpi(\mathbf{k}'))\, \mathrm{d}^2 k'\, \mathrm{d}\omega' \tag{3.22}$$

4. Application of the modulation transfer function

   There is a difference between the image spectrum from marine radar imagery and the corresponding spectrum from in-situ sensors. This difference is due to the radar wave imaging mechanisms are not considered in the band-pass filter. This difference can be reduced if a modulation transfer function is used. This empirical modulation transfer function is related to the interaction of the ripple with long waves and this function is:

$$\mathcal{T}(\mathbf{k}) = k^\beta \tag{3.23}$$

   where the exponent β has been calculated empirically [24, 16]. The empirical value found for the β exponent is $\beta \approx -1.2$ [11]. Therefore the estimation of the three-dimensional wave spectrum $\widetilde{F}^{(3)}(\mathbf{k}, \omega)$ is obtained as

$$\widetilde{F}^{(3)}(\mathbf{k}, \omega) = \mathcal{T}(\mathbf{k})\, F_F^{(3)}(\mathbf{k}, \omega) \tag{3.24}$$

3.4.3   Significant wave height estimation

Significant wave height H_s can be derived from the wave spectrum $F^{(3)}(\mathbf{k}, \omega)$ as:

$$H_s = 4\sqrt{\int_{\Omega_{\mathbf{k},\omega}} F^{(3)}(\mathbf{k}, \omega)\, \mathrm{d}^2 k\, \mathrm{d}\omega} = 4\sqrt{m_0} \tag{3.25}$$

But the X-band marine radars do not provided values of physical parameters related to the backscatter phenomenon or wave elevation, but images coded in relative value of grey scales. Hence, the non-scaled spectra $\widetilde{F}^{(3)}(\mathbf{k}, \omega)$ does not provide wave height estimations directly. $\widetilde{F}^{(3)}$ and $F_\psi^{(3)}$ are different, due to the digitalization done by the WaMoS II to the grey-level values. These grey-level values are affected by some factors such as: the dynamical range of the WaMoS digitalization, the sea surface roughness, the marine radar features, the radar configuration for each installation, etc. If the structure of the image spectrum $F_\psi^{(3)}(\mathbf{k}, \omega)$ is analysed, H_s can be

estimated in a similar way than Synthetic Aperture Radar systems (SAR) [25]. Based on this assumption, the significant wave height has a linear dependence with the root squared of the Signal-to-Noise Ratio (*SNR*) [11, 24], that is defined as:

$$SNR = \frac{\displaystyle\int_{\Omega_{\mathbf{k},\omega}} \widetilde{F}^{(3)}(\mathbf{k}, \omega) \, \mathrm{d}^2 k \, \mathrm{d}\omega}{\displaystyle\int_{\Omega_{\mathbf{k},\omega}} F^{(3)}_{BGN}(\mathbf{k}, \omega) \, \mathrm{d}^2 k \, \mathrm{d}\omega} \tag{3.26}$$

where $F^{(3)}_{BGN}(\mathbf{k}, \omega)$ is the spectral energy of the background noise and it will be explained in the section 3.4.4.

Hence, the significant wave height can be expressed as

$$H_s = c_0 + c_1 \sqrt{SNR} \tag{3.27}$$

where c_0 and c_1 are calibrations constants, which are obtained empirically and depend on each specific installation. The three-dimensional wave spectrum $F^{(3)}(\mathbf{k}, \omega)$ can be calculated from H_s as

$$F^{(3)}(\mathbf{k}, \omega) = C \, \widetilde{F}^{(3)}(\mathbf{k}, \omega) \tag{3.28}$$

where C is a constant used to rescale the spectrum $\widetilde{F}^{(3)}(\mathbf{k}, \omega)$

$$C = \frac{H_s^2}{16 \displaystyle\int_{\Omega_{\mathbf{k},\omega}} \widetilde{F}^{(3)}(\mathbf{k}, \omega) \, \mathrm{d}^2 k \, \mathrm{d}\omega} \tag{3.29}$$

3.4.4 Three-dimensional spectral density of the background noise

A detail analysis of the values of the image spectrum $F^{(3)}_{\psi}$ reveals that there is a background noise that fills all the spectral domain $\Omega_{\mathbf{k},\omega}$ [15, 26]. This noise appears as well in other radar systems, as Synthetic Aperture Radars (SAR) [25], that operates under quite different incidence conditions. The background spectral noise (BGN) is the results of the convolution of the radar pulse $\Pi(R, \phi)$ sweeping the sea surface in range R and azimuth ϕ. $\Pi(R, \phi)$ is defined by the range and azimuthal resolutions (i.e. ΔR, $\Delta \phi$). Hence, the sea cutter image in polar coordinates (R, ϕ) can be expressed as

$$\psi(R, \Phi, t) = \left[\hat{\psi} * \Pi\right](R, \Phi, t) = \int_{R_{\min}}^{R_{\max}} \int_{\phi_{\min}}^{\phi_{\max}} \hat{\psi}(R', \phi', t) \, \Pi(R - R', \, \phi - \phi') \, R \, \mathrm{d}R' \mathrm{d}\phi', \quad (3.30)$$

where $R_{\min}$, $R_{\max}$, $\phi_{\min}$, and $\phi_{\max}$ define the angular sector of the sea surface, which is scanned by the radar. $\hat{\psi}(R', \phi', t)$ indicates the backscatter signal resulting of the different modulation mechanisms that affect the radar scanning of the sea surface. In equation (3.30) the time t corresponds to the temporal scale of the wave evolution, which is assumed to be much slower

than the scanning time scale of the radar. The factor R in the convolution integral (3.30) is responsible of the effective footprint of the radar (i.e. the so-called *facet*), $R\Delta R\Delta\phi$. Transforming the equation (3.30) in Cartesian coordinates (x, y) and applying the Fourier transform, the image spectrum measured by a radar system is given by

$$F_\psi^{(3)}(\mathbf{k}, \omega) = F_{\hat{\psi}}^{(3)}(\mathbf{k}, \omega) F_\Pi^{(3)}(\mathbf{k}, \omega), \tag{3.31}$$

where $F_{\hat{\psi}}^{(3)}$ is the spectrum of the backscatter signal, which is affected by the different modulation mechanisms, such as shadowing, wave tilting, etc., and $F_\Pi^{(3)}$ is the spectrum of the radar pulse shape, which is responsible of the spectral background noise. This noise is the resulting of the backscatter signal collected in the imaged facet. This signal is due to speckle noise caused by the sea surface roughness induced by the local wind [17]. In addition to the effect of the radar pulse, the thermal noise of the radar system is as well part of this noise [25]

$$F_\Pi^{(3)}(\mathbf{k}, \omega) = F_{BGN}^{(3)}(\mathbf{k}, \omega) + F_{\text{thermal}}^{(3)}(\mathbf{k}, \omega), \tag{3.32}$$

being $F_{BGN}^{(3)}$ the spectrum of the noise due to the radar pulse (i.e. the background noise due to the sea surface roughness), and F_{thermal} is the spectrum of the thermal noise, which is assumed as a white noise. Hence, $F_{\text{thermal}}^{(3)}(\mathbf{k}, \omega)$ has a constant value for each wave number $\mathbf{k}$ and frequency ω.

The spectral analysis of the background noise can report additional properties of sea clutter that can not be considered in the inverse modelling technique. BGN spectral components are related to the roughness of the sea surface, which is responsible for the speckle noise in radar images of ocean. Therefore, the energy spectrum of BGN is closely related to the hydrodynamic and meteorological phenomena, which affect the sea surface. The background spectral density is closely related to the sea clutter speckle caused by the sea surface roughness on short spatial scales. The background spectral energy is necessary to extract ocean wave height information from sea clutter time series. The *SNR* expression (3.26) considers the energy of the spectral components of the imaged wave field for the signal and the total spectral background energy of the $F_\psi^{(3)}(\mathbf{k}, \omega)$ for the noise contribution to *SNR*. Besides, the background noise spectra is related to the electromagnetic backscattering phenomena, which occur on the sea surface illuminated by the radar antenna. BGN spectral components are distributed almost throughout the entire domain of $\Omega_{\mathbf{k},\omega}$. The components of the wave components and higher harmonics are clearly identified in $\Omega_{\mathbf{k},\omega}$ because their spectral components are located very close to their respective dispersion relations

$$\omega_q = (q + 1)\sqrt{\frac{gk}{q + 1} \tanh\left(\frac{kd}{q + 1}\right)} + \mathbf{k} \cdot \mathbf{U} \tag{3.33}$$

where $q = 1, 2, \ldots$ indicates the order of the qth-harmonic. In practice only the first harmonic $(q = 1)$ has enough energy to be identified in the image spectrum domain. If q was equal to 0,

the equation (3.33) would be the relation dispersion of linear ocean waves.

The estimation of $F_{\Pi}^{(3)}$, or even $F_{BGN}^{(3)}$, cannot be achieved using the equations (3.31) and (3.32), because the spectrum $F_{\hat{\psi}}^{(3)}$ is unknown. In addition the internal features of the radar electronics responsible of the existence of $F_{\text{thermal}}^{(3)}$ are in most of the cases unknown as well. Assuming that the thermal noise is small, which is a reasonable assumption for operational radar system, and considering the BGN noise a stochastic process statistically independent of all the rest of the spectral contributions related with the wave field (dispersion relation , harmonisc, etc.), the BGN three-dimensional spectral density $F_{BGN}^{(3)}(\mathbf{k}, \omega)$ can be approximated as a function of the image spectrum $F_{\psi}^{(3)}(\mathbf{k}, \omega)$, the spectrum related to the wave components $F_{F}^{(3)}(\mathbf{k}, \omega)$ and the high harmonic spectrum $F_{HH}^{(3)}(\mathbf{k}, \omega)$, which is obtained in a similar way to $F_{F}^{(3)}(\mathbf{k}, \omega)$ but using the high harmonic dispersion relation given by the equation (3.33)

$$F_{BGN}^{(3)}(\mathbf{k}, \omega) \approx F_{\psi}^{(3)}(\mathbf{k}, \omega) - F_{F}^{(3)}(\mathbf{k}, \omega) - F_{HH}^{(3)}(\mathbf{k}, \omega) \tag{3.34}$$

The quasi-static patterns in equation (3.34) are caused by the long range dependence on the sea clutter image and the group line due to intermodulations between different wave field components not considered [11]. These spectral contributions are located in areas of low frequencies. For this reason, the equation (3.34) is an approach for those frequencies higher than a given threshold frequency ω_{th}. Therefore, the main low-pass filter made in the inversion modelling technique 3.4.2 is so important to remove these static patterns.

If constant values of the wave frequency ω are fixed, the dependence of $F_{BGN}^{(3)}(\mathbf{k}, \omega)$ is similar for different ω-planes, because of the fact that speckle noise at a specific sea surface location is uncorrelated for different antenna rotations. So the intensity of the BGN spectral components is independent of the frequency plane and dependent only on the wave number $\mathbf{k}$. An average two-dimensional BGN spectrum $F_{BGN}^{(2)}(\mathbf{k})$ due to the sea surface roughness can be estimated as

$$F_{BGN}^{(2)}(\mathbf{k}) = \frac{1}{\omega_c - \omega_{th}} \int_{\omega_{th}}^{\omega_c} F_{BGN}^{(3)}(\mathbf{k}, \omega) \, \mathrm{d}\omega \tag{3.35}$$

In this case, $F_{BGN}^{(2)}(\mathbf{k})$ presents high values for low wave numbers $\mathbf{k}$. This behaviour of the wave number dependence can be shown by the integration of the two-dimensional BGN spectrum $F_{BGN}^{(2)}(\mathbf{k})$ over all the wave number directions $\theta = \tan^{-1}(k_y/k_x)$:

$$F_{BGN}(k) = \int_0^{2\pi} F_{BGN}^{(2)}(\mathbf{k}(k, \theta)) k \, \mathrm{d}\theta \tag{3.36}$$

where the multiplicative factor k inside the integral is the Jacobian needed to change the Cartesian coordinates (k_x, k_y) to the Polar coordinates (k, θ) used to integrate along all the wave number directions θ.

The averaged one-dimensional frequency BGN spectrum $S_{BGN}(\omega)$ can be obtained from $F_{BGN}^{(3)}(\mathbf{k}, \omega)$ as

$$S_{BGN}(\omega) = \frac{1}{4k_{x_c}k_{y_c}} \int_{\Omega_{\mathbf{k}}} F_{BGN}^{(3)}(\mathbf{k}, \omega) \mathrm{d}^2 k \,, \quad \omega_{th} < \omega \leq \omega_c \tag{3.37}$$

where $\Omega_k \equiv [-k_{x_c}, k_{x_c}) \times [-k_{y_c}, k_{y_c})$ and the normalisation factor $4k_{x_c}k_{y_c}$ is the Ω_k area. Here again, the low frequencies are not considered to avoid the group line and the static patterns.

3.5   Description of the used data

In this work, data from two different locations in the North Sea have been analysed. The following sections deal with the description of these data sets.

3.5.1   Data acquisition

The radars of the FINO 1 platform and Hörnum have installed the WaMoS II system to measure waves and currents. But WaMoS II system needs a good calibration to measure correctly the parameters of wave height. This requires a reference sensor, in our case the sensor is a buoy, a *Datawell WaveRider* model. An analysis of the parameters collected by sea buoys and radar will be executed in this study.

3.5.2   FINO 1 Platform

The data used for the study are taken from the German research platform of FINO 1 (*German Hydrographic Institute* - BSH). FINO1 platform is located in the North Sea, near the German island of Borkum, at the mouth of the river Ems. It consists of a conventional navigation radar under a helicopter platform. The main objective of the platform is to improve the knowledge of hydrological and meteorological sea conditions for the development of wind turbine installations.

The radar located in this platform provides sea radar images. The main characteristic of these images is the temporal and spatial homogeneity that present most of the time. These images are caused by the interaction of the electromagnetic waves produced by the radar antenna with the sea surface ripples caused by the local wind.

3.5.3   Hörnum

Another source of data is the coastal monitoring radar in the German island of Sylt. This radar is working since 2002 for the German centre *Helmholtz-Zentrum Geesthacht*. This station works mainly for shallow water in the North Sea.
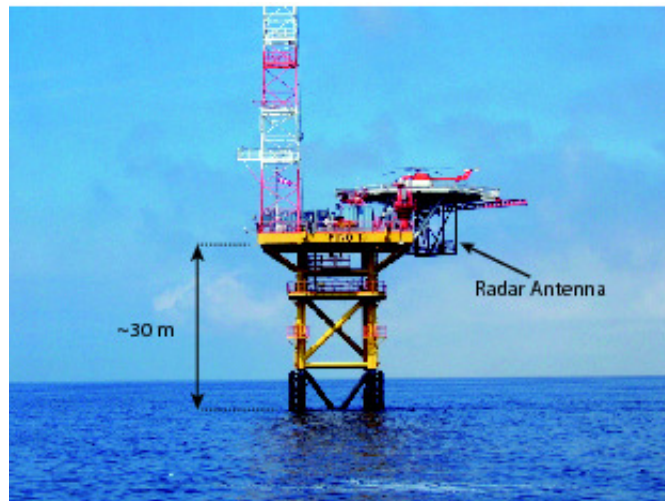
Figure 3.7: Image of the German research platform FINO 1.
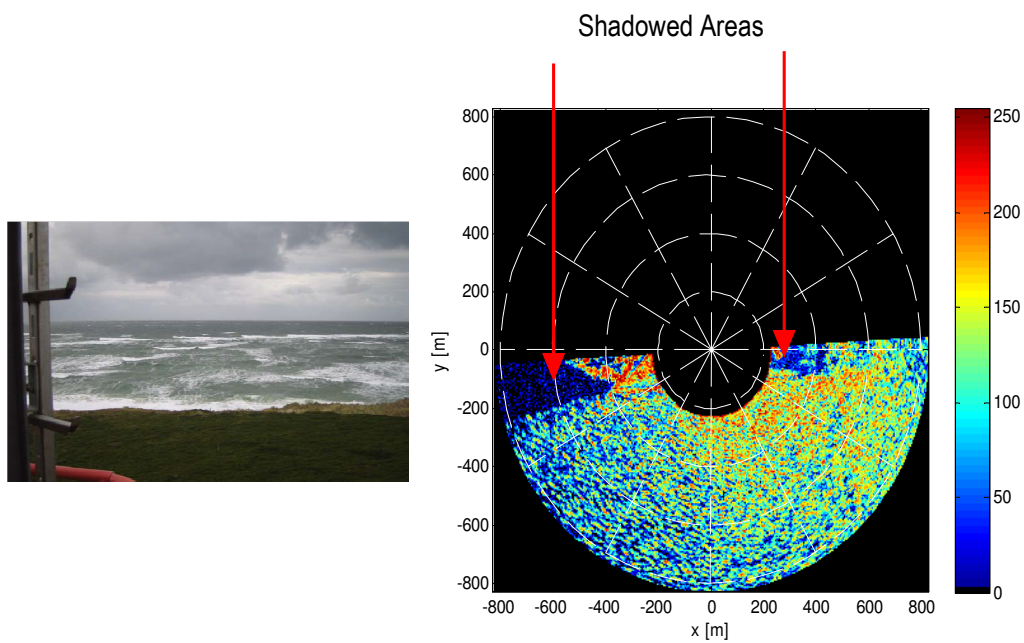
Figure 3.8: On the left, the image of the North Sea from the Hörnum station. On the right, an example of the image taken by the Hörnum radar.

In the figure 3.8, on the right, a Hörnum radar image is presented. This radar only provides the half of the complete radar sector, and there are two small shadowing areas in both sides of the radar.

Part II

Achieved Work: Analysis of Sea Surface Features from X-Band Radar

Chapter 4

Detection of the Dispersion Shell Depending the Radar Azimuth and Range

The main phenomenon related to the imaged wave field, which is visible in the image spectrum is the *dispersion shell* or *dispersion relation* and it will be one of the target in this chapter. The dispersion relation was presented in the section 2.2.1.1. The process followed to analyse the spectra of the radar images is the modelling technique presented in section 3.4.2. In this case, the data applied have been the data provided by the platform FINO 1. It is considered a temporal sequence of N_t consecutive images, where each image has $N_x \times N_y$ pixels. The spatial resolutions in the axes x and y are Δx and Δy, and the temporal interval (i.e. the sampling time of the image time series) is the antenna rotation period Δt.

Applying a three-dimensional *Discrete Fourier Transform* (DFT) to the temporal sequence of images, the image spectrum $F_\psi^{(3)}(\mathbf{k}, \omega)$ is estimated as

$$\hat{F}_\psi^{(3)}(k_{x_{m_1}}, k_{y_{m_2}}, \omega_{m_3}) = c \left| \sum_{n_1=0}^{N_x-1} \sum_{n_2=0}^{N_y-1} \sum_{n_3=0}^{N_t-1} \psi(x_{n_1}, y_{n_2}, t_{n_3}) \, \mathrm{e}^{-\mathrm{j}2\pi \left[\frac{m_1 n_1}{N_x} + \frac{m_2 n_2}{N_y} + \frac{m_3 n_3}{N_t} \right]} \right|^2 \tag{4.1}$$

being $m_1 = 0, 1, \ldots, N_x - 1$, $m_2 = 0, 1, \cdots, N_y - 1$ and $m_3 = 0, 1, \cdots, N_t/2$ and

$$k_{x_{m_1}} = -k_{x_c} + m\Delta k_x \quad ; \qquad \Delta k_x = \frac{2\pi}{N_x \Delta x} \tag{4.2}$$

$$k_{y_{m_2}} = -k_{y_c} + n\Delta k_y \quad ; \qquad \Delta k_y = \frac{2\pi}{N_y \Delta y} \tag{4.3}$$

$$\omega_{m_3} = m_3 \Delta\omega \quad ; \qquad \Delta\omega = \frac{2\pi}{N_t \Delta t} \tag{4.4}$$

being k_{x_c}, k_{y_c} and ω_c the Nyquist cut-off limits for each spectral variables. In equation (4.1), c is a constant of proportionality to keep the variance for a Gaussian process

$$c = \frac{1}{(N_x N_y N_t)^2 \, \Delta k_x \Delta k_y \Delta \omega} \tag{4.5}$$

$\hat{F}_\psi^{(3)}(k_{x_{m_1}}, k_{y_{m_2}}, \omega_{m_3})$ is not exactly the image spectrum $F_\psi^{(3)}(\mathbf{k}, \omega)$ because of the radar images are not a homogeneous Gaussian process and the values of the grey scales are not a Gaussian distribution. Once the $\hat{F}_\psi^{(3)}(k_{x_{m_1}}, k_{y_{m_2}}, \omega_{m_3})$ is calculated, the current of encounter $\mathbf{U}$ is estimated and then the dispersion shell is retrieved by a filter [7], separating the signal owing to the waves and the spectral background noise [24].

In this chapter, the dispersion shell is going to be presented for the whole radar image provided by the WaMoS II system and in an exhaustive study, called *Window analyse*, where the radar image is divided in several small rectangular piece of images, or *windows*, according to the range and azimuth.

4.1   Filter design to extract the dispersion shell

One of the steps in the inverse signal modelling technique is filtering to keep the spectral components $(\mathbf{k}, \omega)$ that hold the dispersion relation. As it was commented above, the background noise must be removed to separate the signal and the noise. The filter to extract the dispersion shell was created. This filter would consist of taking the specific points that obey the dispersion relation equation $\omega = \varpi(\mathbf{k}) = \sqrt{gk \tanh(kd)} + \mathbf{k} \cdot \mathbf{U}$ in the three-dimensional image spectrum $F_\psi^{(3)}(k_{x_m}, k_{y_n}, \omega_v)$. The data that have to be managed now are in $(\mathbf{k}, \omega)$ domain, so they are sampled in frequency and discrete wave number. Therefore, it is not possible to apply the dispersion relation point to point, but in associate intervals to the resolution of each spectral variables. Figure 4.14 shows an example of the dispersion shell.

4.1.1   Three-dimensional pass-band filter

The three-dimensional pass-band filter is the main part of the inverse modelling technique to get the dispersion shell. This filter is presented in [27] and it considers the dispersion shell for linear waves and the resolution of all spectral variables Δk_x, Δk_y and $\Delta \omega$ defined in Nyquist domain $\Omega_{\mathbf{k}, \omega}$:

$$\Omega_{\mathbf{k}, \omega} = [-k_{x_c}, k_{x_c}) \times [-k_{y_c}, k_{y_c}) \times [0, \omega_c) \tag{4.6}$$

being k_{x_c}, k_{y_c} and ω_c the Nyquist cut-off limits for each spectral variables. Hence, the equations (4.2), (4.3) and (4.4) are defined for Nyquist domain as well, being $k_{x_{m_1}} \in [-k_{x_c}, k_{x_c})$, $k_{y_{m_2}} \in [-k_{y_c}, k_{y_c})$ and $\omega_{m_3} \in [0, \omega_c)$.

The theoretical filter, represented by $\mathfrak{F}(m_1, m_2, m_3)$, is applied to the FFT estimation of the image spectrum for all the frequencies in the $\Omega_{\mathbf{k}, \omega}$ and all the waves numbers. The filter presents
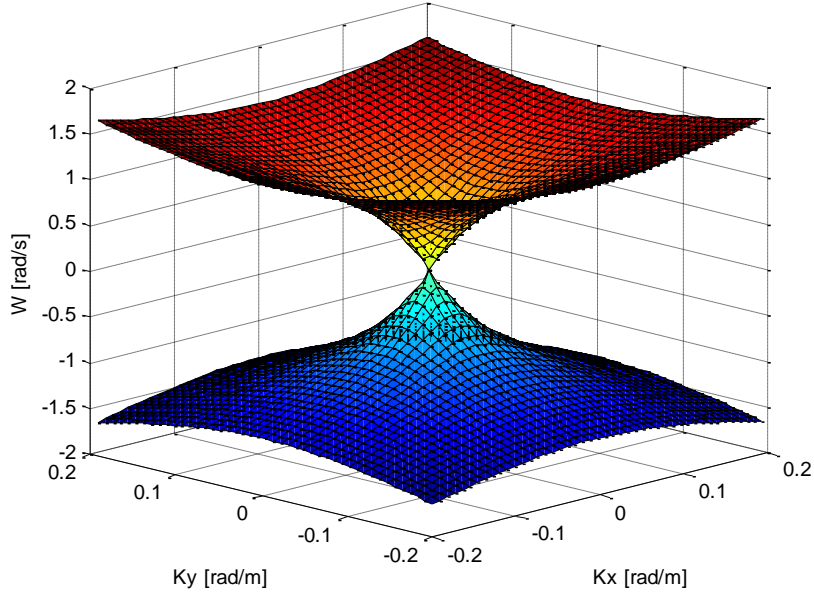
Figure 4.1: Example of the dispersion shell.

this function:

$$\mathfrak{F}(m_1, m_2, m_3) = \begin{cases} 1 & \text{if } m_3 \in \Omega_{m_1,m_2} \\ 0 & \text{otherwise} \end{cases} \tag{4.7}$$

being

$$\Omega_{m_1,m_2} \equiv \left\{ m_3 \mid \min \left(\omega_{m_1,m_2}^-, \omega_{m_1,m_2}^+, \hat{\omega}_{m_1,m_2}^- \right) \leq \omega_{m_3} \leq \max \left(\omega_{m_1,m_2}^-, \omega_{m_1,m_2}^+, \hat{\omega}_{m_1,m_2}^+ \right) \right\} \tag{4.8}$$

where

$$\omega_{m_1,m_2}^+ = \varpi(\mathbf{k}_{m_1,m_2} + n_1 \, \Delta \mathbf{k}) \tag{4.9}$$

$$\omega_{m_1,m_2}^- = \varpi(\mathbf{k}_{m_1,m_2} - n_1 \, \Delta \mathbf{k}) \tag{4.10}$$

$$\hat{\omega}_{m_1,m_2}^+ = \varpi(\mathbf{k}_{m_1,m_2}) + n_2 \, \Delta \omega \tag{4.11}$$

$$\hat{\omega}_{m_1,m_2}^- = \varpi(\mathbf{k}_{m_1,m_2}) - n_2 \, \Delta \omega \tag{4.12}$$

being n_1 the bandwidth of the filter in $\mathbf{k}$, n_2 the bandwidth of the filter in ω, $\mathbf{k}_{m_1,m_2} = (k_{x_{m_1}}, k_{y_{m_2}})$ and $\Delta \mathbf{k} = (\Delta k_x, \Delta k_y)$.

In the figure 4.2 a scheme of this filter is shown. Summarising, a pair of $(k_{x_{m_1}}, k_{y_{m_2}})$ is taken and its corresponding value of dispersion shell is calculated. If the value of the dispersion shell is in the margin between $[\omega_{\max}, \omega_{\min}]$, the filter will select this value as one.
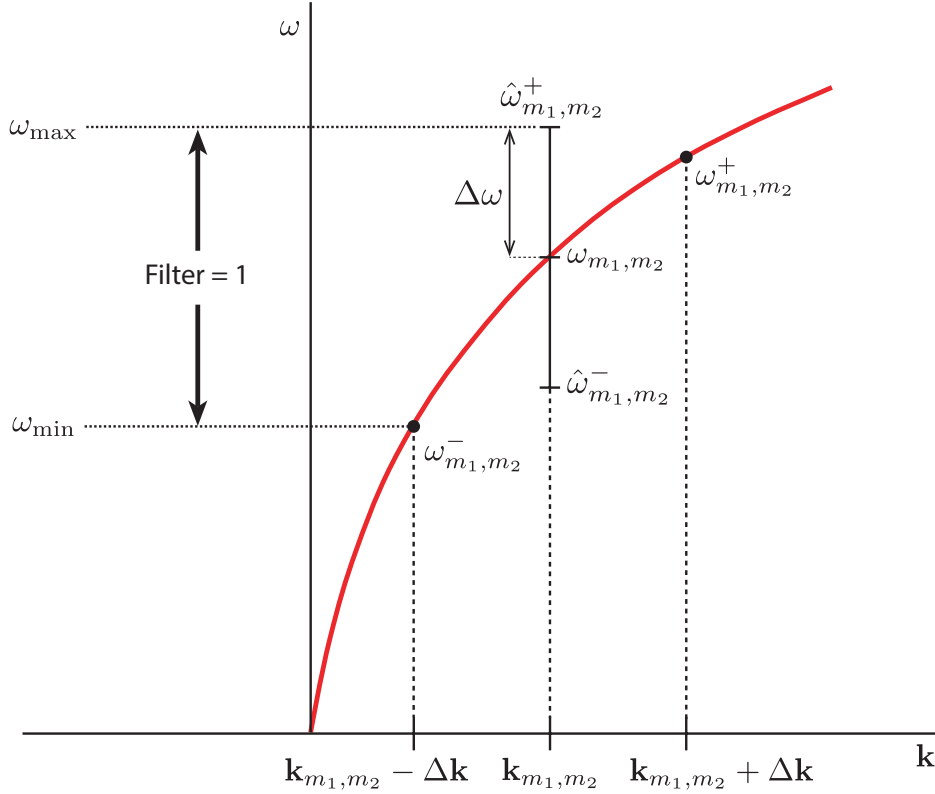
Figure 4.2: Scheme of the theoretical filter for $n_1 = 1$ and $n_2 = 1$.

4.1.2 Adaptive filter

The filter described above is the *theoretical representation* of the dispersion shell for a discrete
$(\mathbf{k}, \omega)$-domain, independently of the current of encounter $\mathbf{U}$ and the depth d, where all data inside
the dispersion relation should have similar values. However, in the reality it does not happen
because there are some regions with very high intensity values, and the rest of the dispersion
shell presents values similar to the background noise. Hence, a second filter or *adaptive filter*
was implemented to take only the values with more intensity. The process of this filter model is
divided in two steps:

1. The theoretical filter, described previously, is used to select the theoretical dispersion shell,
   which depends on the current of the encounter and the water depth.

2. The adaptive filter is used over the theoretical dispersion shell obtained before. This filter
   searches the maximum of the dispersion shell. Taking into account the ω-plane where
   the maximum of the image spectrum is located, the filter does a sweep in each ω-plane
   considering all the positions which have a energy proportional to the maximum. This
   proportion is not fixed, this proportion changes according to the ω-plane. The dispersion
   shell energy for low and high frequencies is low, however for middle frequencies, the energy
   is high.

In the figure 4.3 it is represented the theoretical dispersion shell filter for FINO 1 data with $U_x = -0.38$ m s^{-1}, $U_y = -0.40$ m s^{-1} in the wave direction, and $d = 30$ m. Using the same data, the adaptive filter is used to work over it, and the result is shown in the figure 4.4. It is easy to realise that the adaptive filter disregards quite irrelevant values.

4.2   Higher harmonics

The dispersion shell is not the only phenomenon produced by the waves. There are important harmonics to be study. The equation that manages these harmonics is (3.33)

$$\omega_q = (q+1)\sqrt{\frac{gk}{q+1}\tanh\left(\frac{kd}{q+1}\right)} + \mathbf{k} \cdot \mathbf{U} \quad ; \quad q = 0, 1, 2, \dots \tag{4.13}$$

It has already been commented, when $q = 0$ equation (4.13) becomes the dispersion shell. When the value of $q = 1$, the *first harmonic* is calculated. Figure 4.5 shows the first harmonic filtered by the theoretical filter for the same data than the figures above.

The first harmonic is presented for the higher frequencies and the rest of higher harmonics are not so important than the first. But there are other negative effects such as the *aliased first harmonic* and the *aliased dispersion relation*. Their values are not so intense and they can be observed in figure 4.6. Because of these low energy values presented in the study data, they do not interfere in the spectra and it is considered not to take into account in this work.

4.3   Additional tools to process the radar images of the sea surface

4.3.1   Adding speckle noise to the blanking areas

The radar image is not always a perfect image to be analysed, because in some of them there are parts without information due to the structure or the platform where the radar is installed, or even to the port if the radar is sited close to the coast. For this reason, these blanked parts are filled by *speckle noise* [28]. The speckle noise is a granular and multiplicative noise which is inherent in all radar systems and degrades the quality of the radar images, it is very common in synthetic aperture radar (SAR) as well. The speckle noise is produced when a electromagnetic wave interferes with objects or particles whose dimensions are similar to the electromagnetic wavelength, increasing the mean grey level of a local area.

In the figure 4.7 it is represented the same radar image in spatio-temporal domain but on the right, the speckle noise is introduced to filled all the blanked areas, like the center and the circular sector of the image. The speckle noise has been chosen to fill blanked areas because this noise is implicit in radar systems and it provides authenticity in radar images. The speckle noise is only introduced and considered for the study of the whole radar images 4.5. However
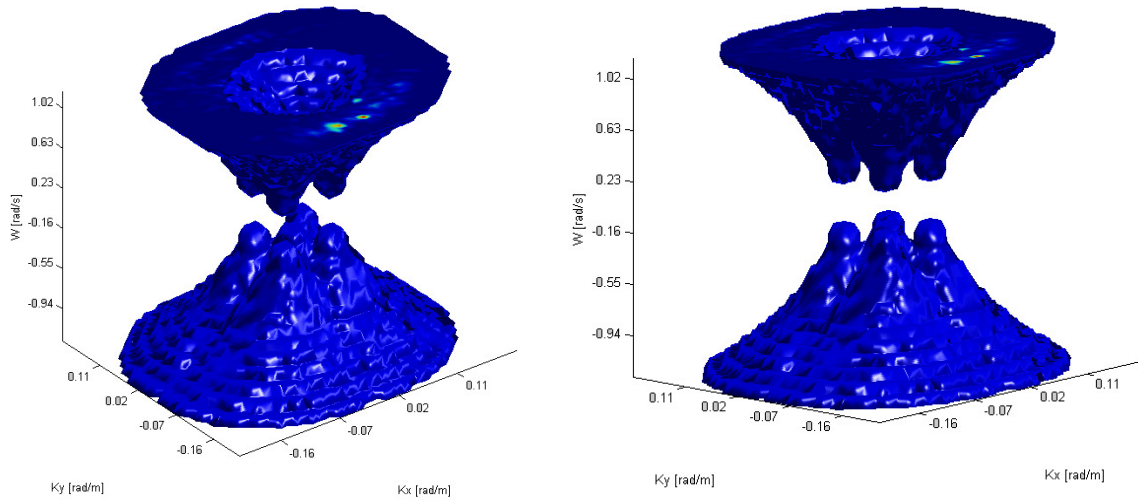
Figure 4.3: Dispersion shell filtered by the theoretical filter for FINO 1 data with $U_x = -0.38$ m s^{-1}, $U_y = -0.40$ m s^{-1} and $d = 30$ m.
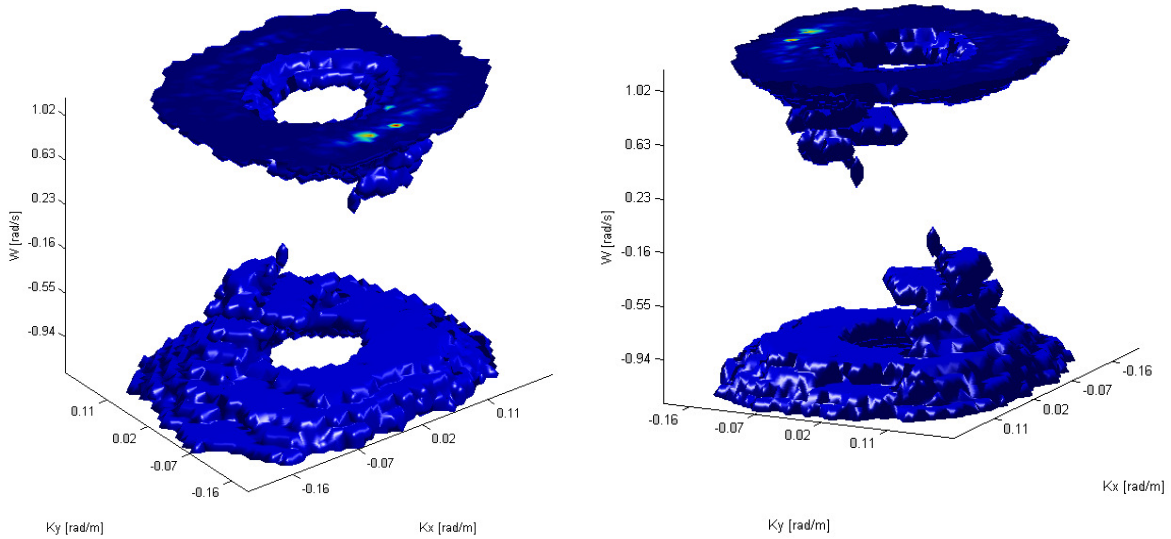
Figure 4.4: Dispersion shell filtered by the adaptive filter for the previous FINO 1 data, corresponding to the figure 4.3, with $U_x = -0.38$ m s^{-1}, $U_y = -0.40$ m s^{-1} and $d = 30$ m.

for windows detailed study 4.6 the blanked areas have not been considered.
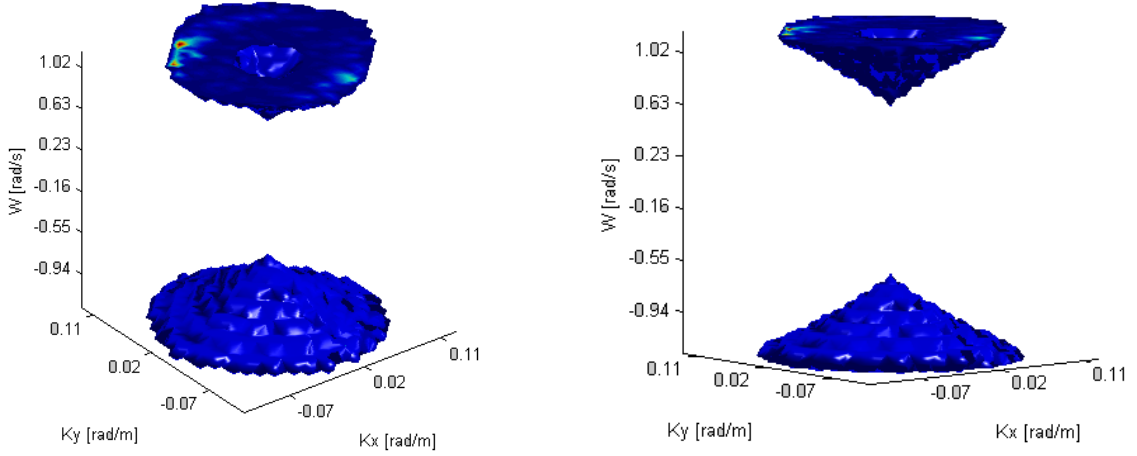
Figure 4.5: The first harmonic filtered by the theoretical filter for FINO 1 data with $U_x = -0.38$ m s^{-1}, $U_y = -0.40$ m s^{-1} and $d = 30$ m.
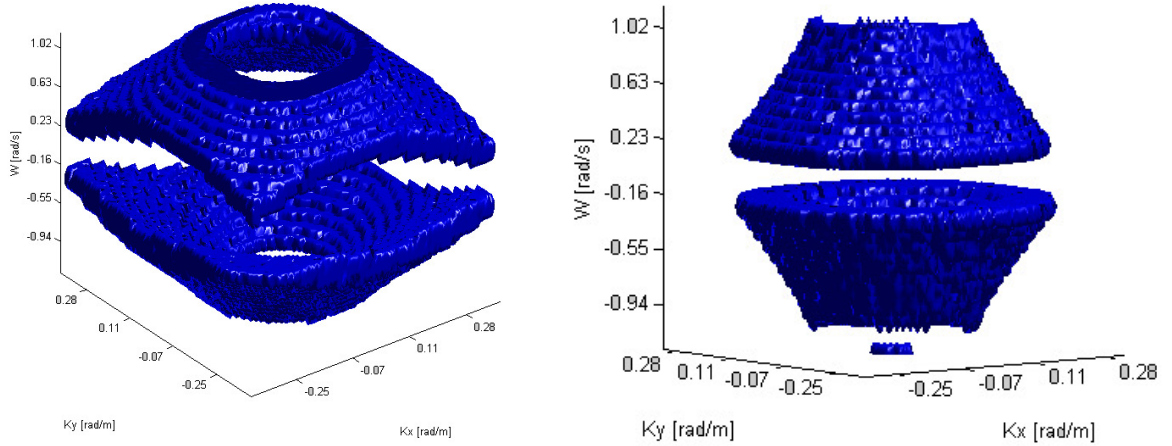
Figure 4.6: On the left, there is the aliased dispersion relation and on the right, the aliased first harmonic is presented, filtered by the theoretical filter for FINO 1 data with $U_x = -0.38$ m s^{-1}, $U_y = -0.40$ m s^{-1} and $d = 30$ m.

4.3.2   The interpolation

Once the dispersion shell and the rest of the phenomena (the first harmonic and the group line) are extracted from the $\hat{F}_\psi^{(3)}(k_{x_{m_1}}, k_{y_{m_2}}, \omega_{m_3})$, the background noise is the result. In [9] there are presented two different methods to carry out the interpolation of the background, getting good results for both of them. These methods are *linear interpolation in ω-domain* and *least squared fit in $\mathbf{k}$-domain*. But in this work, the interpolation is carried out in ω-domain but randomly. It
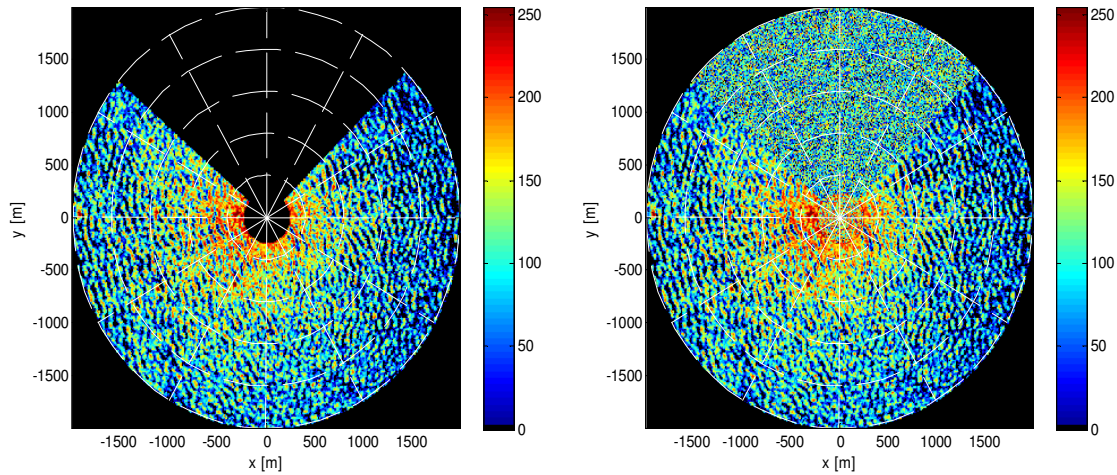
Figure 4.7: On the left, it is the real radar images provided by the WaMoS II system. On the right, it is the same radar images on the left with speckle noise in blanked areas.

means, it is going to be taken a ω and it is going to be considered the points (k_x, k_y) close to the area to be interpolated, but these points (k_x, k_y) will be put randomly, if it were noise.

In the figure 4.8, it is represented an example of interpolation, where the left image represents the original spectrum of one small window of the radar image. The more intense pixels show the dispersion shell for the plane $\omega = -0.55$ rad s^{-1}. The image on the right represents the same spectrum than the left one, but in this image the dispersion shell and the first harmonic were removed and the interpolation was done.
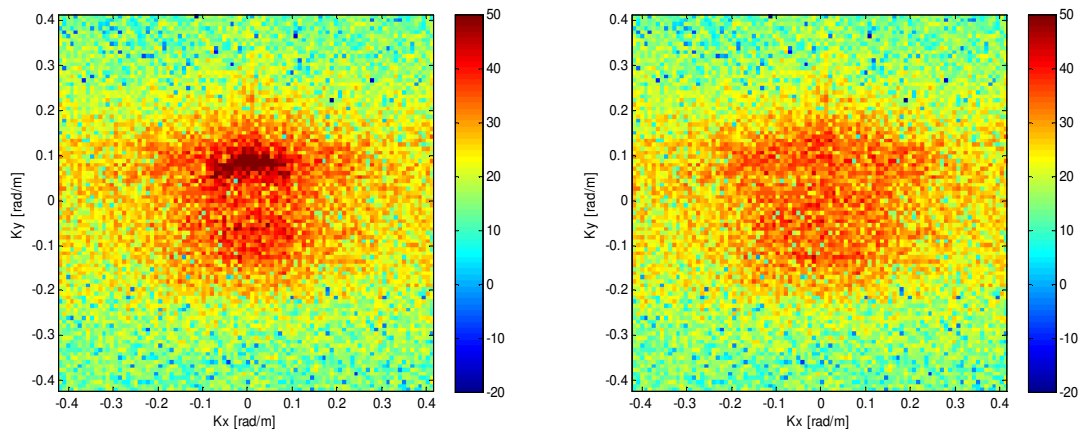
Figure 4.8: On the left, it is the spectrum of the radar images. On the right, it is the same spectrum after doing the interpolation.

4.4   Signal to Noise Ratio

Signal to Noise Ratio (*SNR*) is one of the most important parameter to be considered. For this case, as it was commented before, *Signal* will be the dispersion relation owing to the waves. Nevertheless *Noise* will be the background noise. The main problem is that, in the spectrum, there are more phenomena caused by the waves, such as the first harmonic and the group line. Therefore, some different *Signals* and *Noises* will be studied according to these phenomena and the interpolation. The different *SNR*s estimated for this work will be presented with more details in chapter 6.

4.5   Processing of the whole radar images
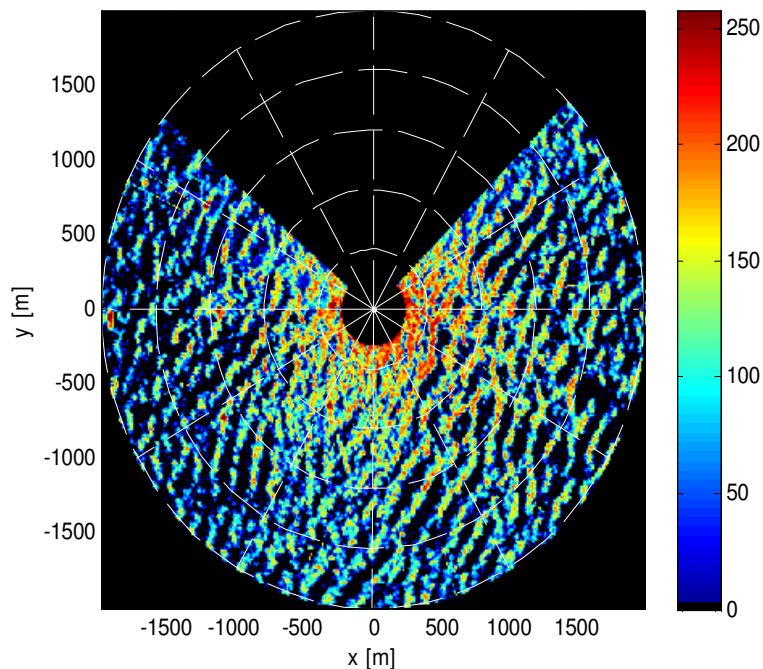
Figure 4.9: Image of one of the instants of the time series of the X-band marine radar for FINO 1 data set.

The whole radar images sequences are evaluated and the process followed to manage it is:

- The WaMoS II system provides the radar images in Polar coordinates, therefore the first step is transforming the Polar coordinates to Cartesian.

- Filling the blanked parts with speckle noise as it is discussed before in section 4.3. The figure 4.7 is an example of the kind of image which is going to be used in this process.

- The Fast Fourier Transform is applied in the 32 images, which compose a data set.

- The dispersion shell, the first harmonic and the group line are extracted.

- The interpolation is carried out in the parts that have been removed, such as the dispersion shell, the first harmonic and the group line, as it is discussed before in section 4.3. The figure 4.8 is an example of the interpolation performed.

- The Inverse Fast Fourier Transform is done to obtain the resulting radar images.

- The Signal to Noise Ratio calculation is done considering different factors, how will be presented in detail in the chapter 6.
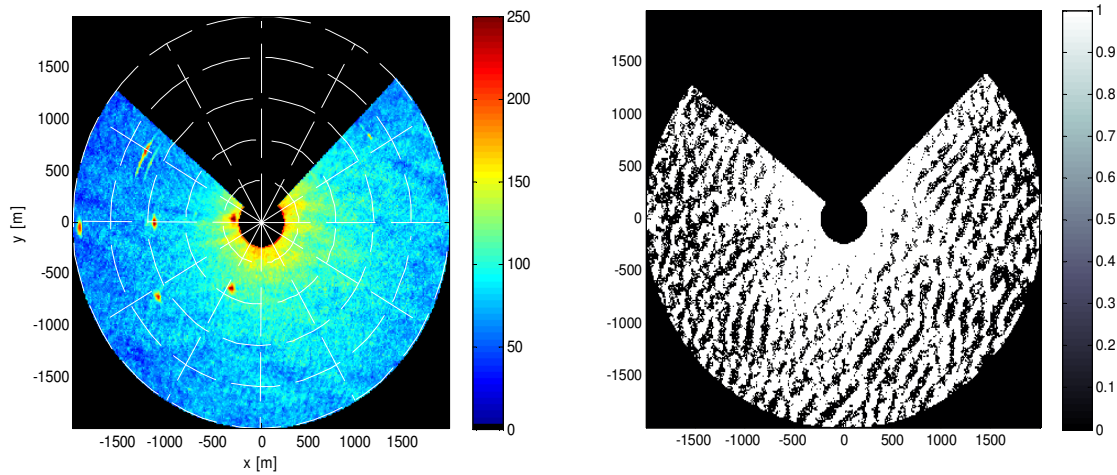
Figure 4.10: The mean of all the 32 images recorded for the data set depicted in the figure 4.9 on the left. On the right, the mask for the same instant of time than the picture 4.9.

Similar results have been obtained for these data which present in their radar images visible waves. In these cases the significant wave height is higher than 2.5 m.

The data used like a model of results is a FINO 1 file recorded the 31st of January in 2013, at 3 a.m. In the figure 4.9 the sea surface for this set of data is represented. It is very clear to sea the front of the waves. The main characteristics provided by the sensors are:

- Mean wave direction ($MDIR$): 301º

- Significant wave height (H_s): 6.42 m

- X component of the current (U_x): 0.63 m s^{-1}

- Y component of the current (U_y): -0.27 m s^{-1}

- Modulus of the current (U): 0.69 m s^{-1}

- Peak period (T_p): 11.11 s

- Mean period (T_{m02}): 9.06 s

The radar imagery have been averaged for all the 32 images, and the mean of all of these is represented in figure 4.10 on the left. It is possible to observe 6 points on the left in the image which intensity is high and they are supposed to be wind turbine installed in the sea. The image on the right in the figure 4.10, the mask of the radar image for the same instant of time than the picture 4.9 is depicted. Black colour indicates the shadowing of the waves, and white colour represents the part of the wave illuminated by the radar.

Once the radar signal has been prepared and shown (i.e. the mean of all the images of the data set, the illumination mask and following filling the blanking areas by speckle noise), the spectra of the images are going to be studied focus on the dispersion relation. The FFT is applied in all the data set. The vector $\mathbf{k}$, the value of the current and the 3D-spectrum $\hat{F}_{\psi}^{(3)}(k_x, k_y, \omega)$ are obtained. With these parameters it is possible to get the three-dimensional pass-band filter (4.1.1) and then employed the adaptive filter (4.1.2) to extract the dispersion relation of the spectrum. Figure 4.11 represents a comparison between the three-dimensional pass-band filter and the original 3D-spectrum before being filtering. The filter is represented by 4 colours according to the phenomenon displayed, being the orange colour which represents the dispersion relation, in green colour the aliased of the dispersion relation, in light blue the first harmonic and in dark blue the aliased first harmonic. For both three-dimensional pass-band filter and spectrum, three different axis transects have been shown, being the $k_x = 0$ rad m^{-1} the first transect represented. In this transect the dispersion relation in the spectrum can be observed clearly and in the same positions of the theoretical dispersion shell shown by the filter. Then $k_y = 0$ rad m^{-1} axis cut is represented but in this case the spectrum does not show the dispersion relation properly. The last cut is for $\omega = -0.94$ rad s^{-1} and in this plane the dispersion relation and the first harmonic are visible in the spectrum.

The following step is filter the spectrum, first by the three-dimensional pass-band filter and then by the adaptive filter. In figure 4.12 it is depicted the extraction of the dispersion relation. Hence the same three cuts for k_x, k_y and ω of the spectrum are shown but the dark blue colour represents the positions of the dispersion shell that have been removed. For the planes k_x and ω the dispersion shell extraction is precise.

The adaptive filter have taken the highest values of the spectrum bound to the dispersion relation. Figure 4.14 shows the shape of the dispersion relation that have been retrieved by the filtered process from the spectrum. The dispersion shell presents symmetry how can be seen in the picture.

The positions in the spectrum that have been removed, such as the values corresponding to the dispersion shell, the first harmonic and the group line, must be replaced how it was commented in the subsection 4.3.2. The interpolation is carried out in ω-domain randomly and the result is shown in figure 4.13. The same transects $k_x = 0$ rad m^{-1}, $k_y = 0$ rad m^{-1} and $\omega = -0.94$ rad s^{-1} are depicted to show the good results obtained in the interpolation process.
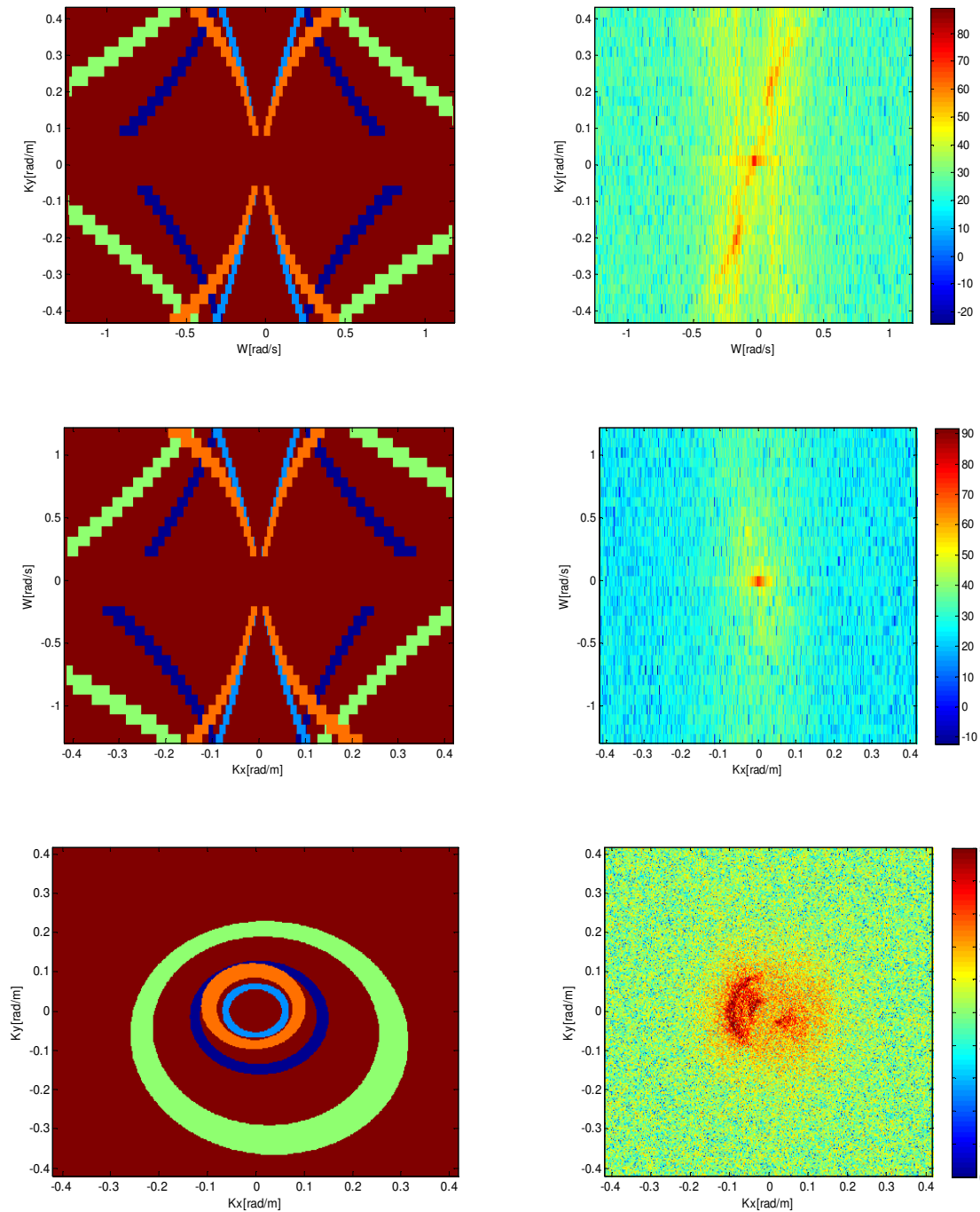
Figure 4.11: Pictures on the left represent the three-dimensional pass-band filter. The pictures on the right represent the spectra before being filtering. The first row depicts a cut in the 3D-spectrum for $k_x = 0$ rad m^{-1} axis, the second row represents a cut in the 3D-spectrum for $k_y = 0$ rad m^{-1} axis and bottom row depicts a cut for $\omega = -0.94$ rad s^{-1}.
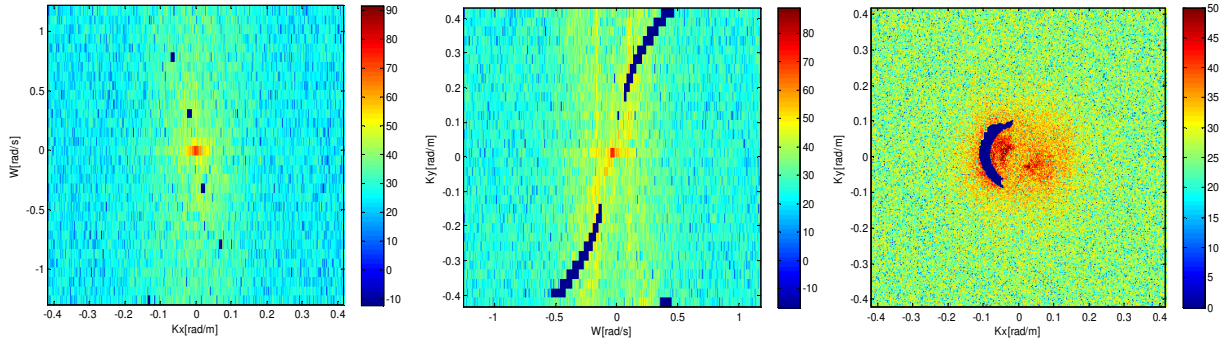
Figure 4.12: The different transects $k_x = 0$ rad m^{-1}, $k_y = 0$ rad m^{-1} and $\omega = -0.94$ rad s^{-1} for 3D-spectrum without the dispersion shell.
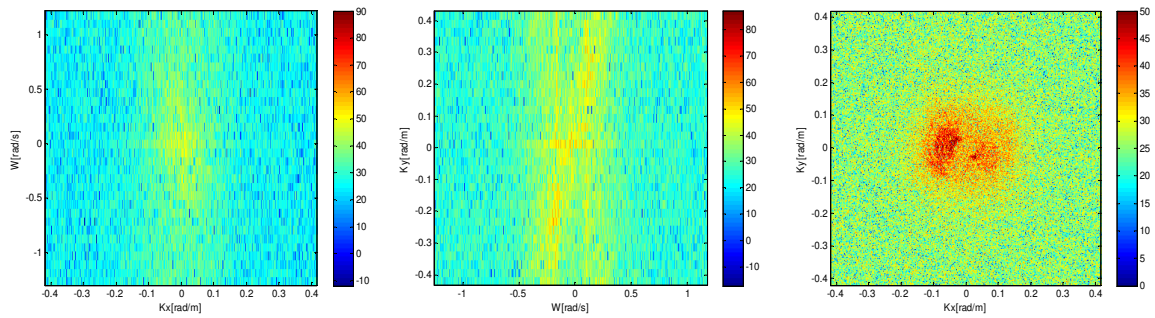
Figure 4.13: Interpolation made in the spectrum, in this case are represented the transects $k_x = 0$ rad m^{-1}, $k_y = 0$ rad m^{-1} and $\omega = -0.94$ rad s^{-1}.

4.6 Window analysis of the radar images

This section collects an exhaustive study of the radar images. The whole radar image is divided in several squared windows according to the range and azimuth of the radar. The size of each window is approximately 700 m × 700 m.

Five ranges are contemplated, from near range (300 m) until far range (1900 m), covering in each range 700 m. There is a small overlap between two consecutive ranges, hence the whole range is covered efficiently.

Not all the azimuths are useful. The possible azimuths under study are included in the interval [69º - 285º], and the rest of the angles (it means, from 0º to 68º and from 286º to 359º) belongs to the blanked areas. The angles sweep done for the azimuth takes the angles separated 15º from the wave direction provided by the WaMoS II system. The number of windows for each range will be between 13 and 15. It is owing to the fact that the window does not consider the blanked areas, and for this analysis, the blanked parts are not filled by speckle noise, but the blanked areas are ignored.
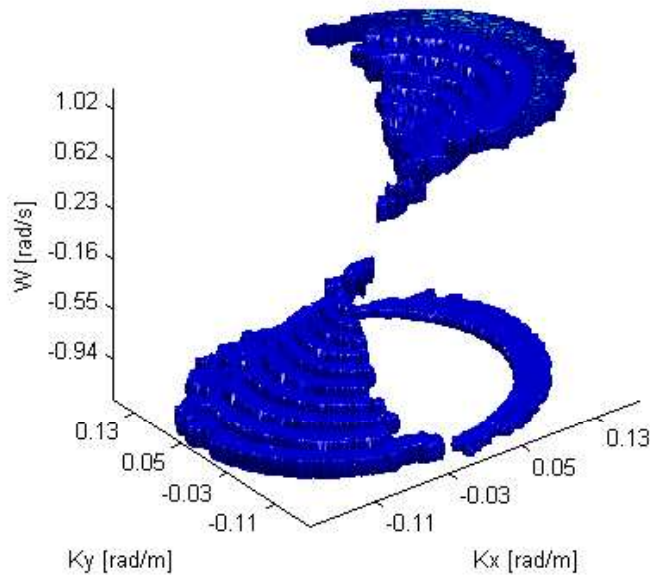
Figure 4.14: Dispersion shell removed from the spectrum after the filtered process.

All windows are normalised conforming to a selected value. This selected value is fixed for each set of data because this value corresponds to the maximum value of the dispersion shell contained by the window in wave direction for middle range (750 m - 1450 m).

For each window, the dispersion relation, the group line and the *SNR* are studied. But in this chapter the dispersion relation and the mean intensity of the signal and the spectra will be asserted, being the group line the target in the next chapter 5 and Signal to Noise Ratio in chapter 6. The main characteristics under study in each window will be:

- The mean intensity of the radar signal.

- The mean intensity contained in the 3D spectrum of the dispersion shell.

- The mean intensity contained in the 3D spectrum of the group line.

- The mean of the 3D spectrum.

- The mean of the 2D spectrum.

- Signal to Noise Ratio for both filters.

The steps made for windows analysis are the following:

- Positioning the azimuth in the direction under study. The WaMoS II system provides the radar images in Polar coordinates and turning the Polar images is easier than in Cartesian, hence changing the azimuth will be performed in Polar coordinates.

- Transforming the radar images in Polar coordinates to Cartesian.

- Taking the window under study, for a particular range and for an azimuth already positioned.

- The Fast Fourier Transform is applied in the 32 images, which compose a data set.

- The dispersion shell, the first harmonic and the group line are extracted from the window under study.

- The interpolation is carried out in the parts that the dispersion shell, the first harmonic and the group line have left empty, following the way described before in section 4.3.

- The Inverse Fast Fourier Transform is done to obtain the resulting window radar images.

- The Signal to Noise Ratio calculation is done considering different factors, how will be presented in detail in the chapter 6.

Firstly, the research about the behaviour of the dispersion shell with the range will be examined. Then, the dispersion shell will be evaluated according to the azimuth.
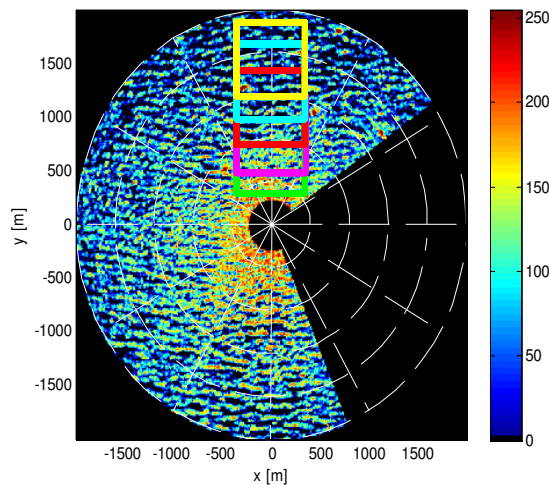
Figure 4.15: These are the five windows considered for each range (green window for $R1$, pink window for $R2$, red window for $R3$, blue colour for $R4$ and yellow window for $R5$) in the wave direction.

4.6.1   Range study

The whole radar image has been demarcated according to the range in five different regions:

- $R1$: It is the nearest range to the radar. It covers the distance 300 m - 1000 m from the radar.

- $R2$: It is the following range and it covers the distance 500 m - 1200 m from the radar.

- $R3$: It is middle range and the distance covered is 750 m - 1450 m from the radar.

- $R4$: In this range the distance covered is 1000 m - 1700 m.

- $R5$: It is far range, the furthest distance from the radar covering from 1200 m - 1900 m.

In figure 4.15 the five windows to be analysed are presented. The overlap among the windows is visible in the figure as well. In this study, only the azimuth corresponding to the wave direction is considered, or by default, like in this case, the azimuth of the opposite direction to the waves because the azimuth corresponding to wave direction is in the blanked area. Hence is going to be considered the *coming-from criterion*. Therefore, the azimuth prearranged will be equal to 121º (301º - 180º).

The results obtained are collected in the following table 4.1, where the characteristics under study in this chapter are:

- I_{signal}: The mean intensity of the radar signal.

- $I_{\text{dispersion}}$: The mean intensity contained in the 3D spectrum of the dispersion shell.

- I_{3D}: The mean of the 3D spectrum.

- I_{2D}: The mean of the 2D spectrum.

Table 4.1: Results in range study.

Ranges	I_{signal} [dB]	I_{3D} [dB]	I_{2D} [dB]	$I_{\text{dispersion}}$ [dB]
R1 (300 m - 1000 m)	20.14	-34.77	-14.38	35.57
R2 (500 m - 1200 m)	19.39	-35.75	-25.66	35.19
R3 (750 m - 1450 m)	18.55	-34.99	-17.33	34.67
R4 (1000 m - 1700 m)	17.72	-36.42	-18.93	33.97
R5 (1200 m - 1900 m)	17.03	-35.91	-20.38	33.29

Figure 4.16 shows easily the data collected in the table 4.1. In all the analysed data, the mean intensity of the radar signal is higher for near range and lower in far range. And the same happens with the intensity of the dispersion relation. However the mean intensity of the spectrum in 3D presents very close values but it is not always higher in near range, and the same occurs for the mean intensity of the spectrum in 2D for $\mathbf{k}$ in the direction of the maximum ($\mathbf{k}_{max}$).

In the figure 4.17 it is observed that the intensity of the dispersion relation is more intense in near range than in far range. For this azimuth, the dispersion relation is defined for each ranges.

4.6.2 Azimuth study

The whole radar image has been demarcated according to the azimuth among 13 to 15 windows for each range ($R1$, $R2$, $R3$, $R4$ and $R5$). Therefore the maximum number of windows to be
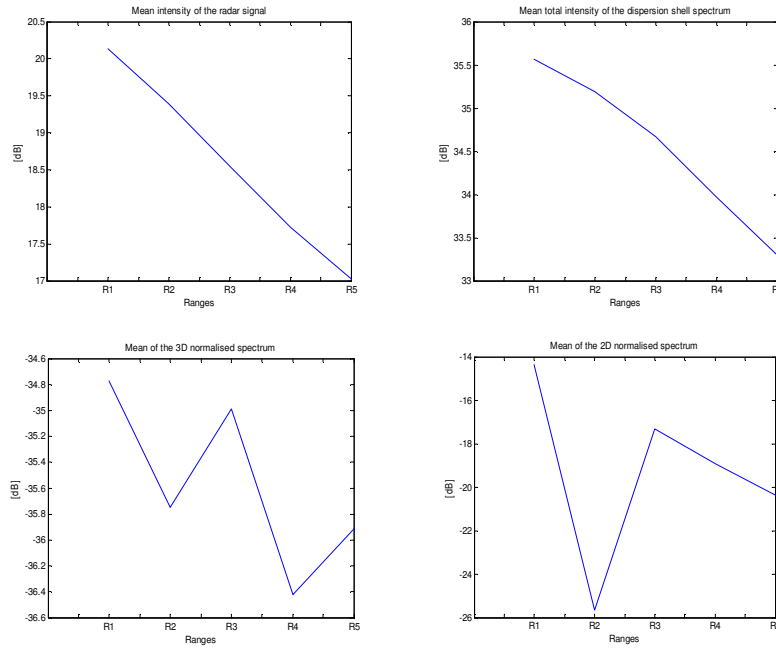
Figure 4.16: The graphic above on the left, is the mean intensity of the radar signal. Above on the right, it is the mean intensity contained in the 3D spectrum of the dispersion shell. Down on the left, it is the mean of the 3D spectrum, and on the right it is the mean of the 2D spectrum.

evaluated in each radar file are 75. In the figure 4.18 all these windows are presented. For $R1$ and $R2$ the essential limits are in the blanked areas, which are not considered in this study. The windows are not in the same position for all radar files. Azimuths are calculated from the wave direction for each radar file, considering 15º of difference between one window and the adjacent. Overlaps can be observed among the windows as well, but this fact allows a deep recognition.

To evaluate the main characteristics of the dispersion shell according to the azimuth, it is going to be explain exhaustive for all the azimuths for only one range, and then, a comparison between all the azimuth for all ranges will be presented. Therefore, the range prearranged will be the middle range $R3$ (750 m - 1450 m). How it was commented before, for this specific data set, the wave direction is in the blanked area, so it is considered the coming-from criterion, being the main direction the azimuth corresponding to the opposite of the wave direction (121º in this case).

A similar table 4.2 than 4.1 is presented but for all azimuth for the range $R3$. The parameters under study are the same than the previous subsection 5.3.1.

Figure 4.19 shows the data collected in the table 4.2. The mean intensity of the radar signal is slightly higher close to the main direction 121º and the descending tendency of the curve happens close to the wave direction 301ºand cross to the wave direction. The dispersion relation is higher close to the main direction as well and lower in cross direction respect to the main direction. If it was possible to represent all the azimuths, there would be another maximum in the wave direction. The mean intensity of the spectrum in 3D presents the maxima values near
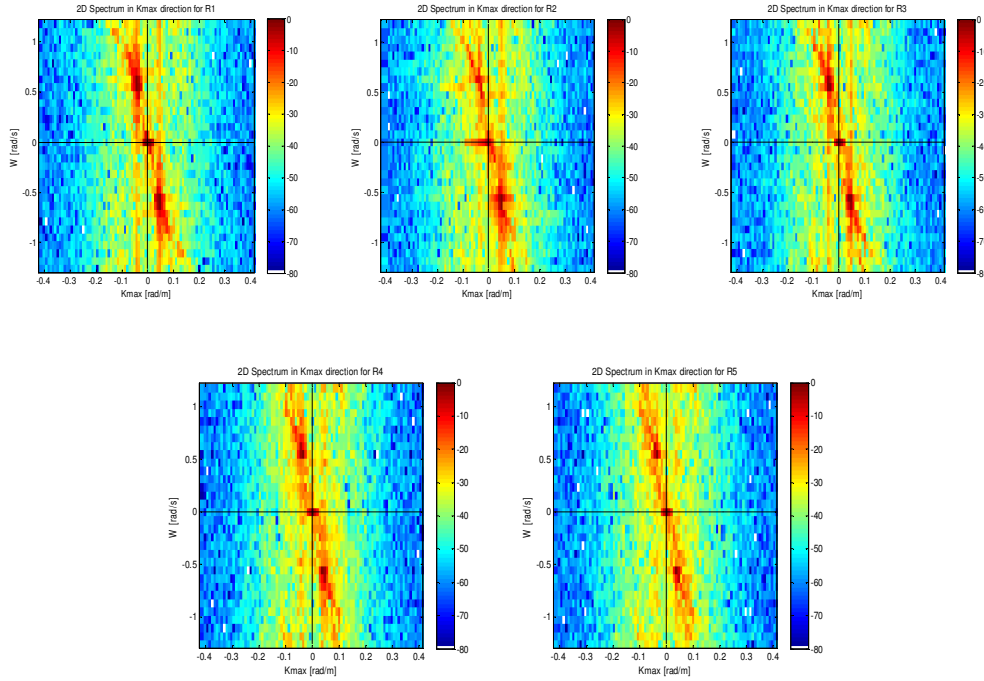
Figure 4.17: 2D spectra for **k** in the direction of the maximum for the 5 different ranges.

to the cross direction 211º respect to main direction, and the minima values are nearby the main direction. For the mean intensity of the spectrum in 2D for **k** in the direction of the maximum ($\mathbf{k}_{max}$) the descending tendency of the curve happens nearby the wave direction 301º.

In the figures 4.20 and 4.21 all the spectra in $\mathbf{k}_{max}$ direction are depicted. The intensity of the dispersion shell is greatest in the main direction (121º) and, it is supposed in the wave direction (301º) as well. The visibility of the dispersion relation is defined in the main direction (121º) and, it is supposed in the wave direction (301º) as well. However, in cross direction the dispersion shell is not defined and the intensity is weak, and even the background is more intense in these azimuths. Sometimes is not possible to extract the dispersion relation in cross direction, or only removing a small part of it.

This study for all the azimuths has been done for each range, from $R1$ to $R5$ and the results are shown in the figure 4.22. Five curves are presented, each curve represents the results obtained for each range for all the azimuths under study. It means, the pink curve represents the values obtained for all azimuths for short range $R1$, the yellow curve is the study done for $R2$, the blue colour describes the results for all azimuths in middle range (i.e. corresponding to the detailed study presented before), the green colour indicates the values got for range $R4$ and red colour for far range $R5$. In this figure are depicted 4 subimages. The first subimage, above on the left, is the mean intensity for all azimuths and ranges. It can be observed that the intensity is greatest in short range and it decreases for far range. The biggest oscillations between maximum and minimum values happen for far ranges, the rest of the curves are more or less flat except when the curves start to descent nearby wave direction 301º. The second subimage, above on the right, represents the mean intensity contained in the 3D spectrum of the dispersion shell. For
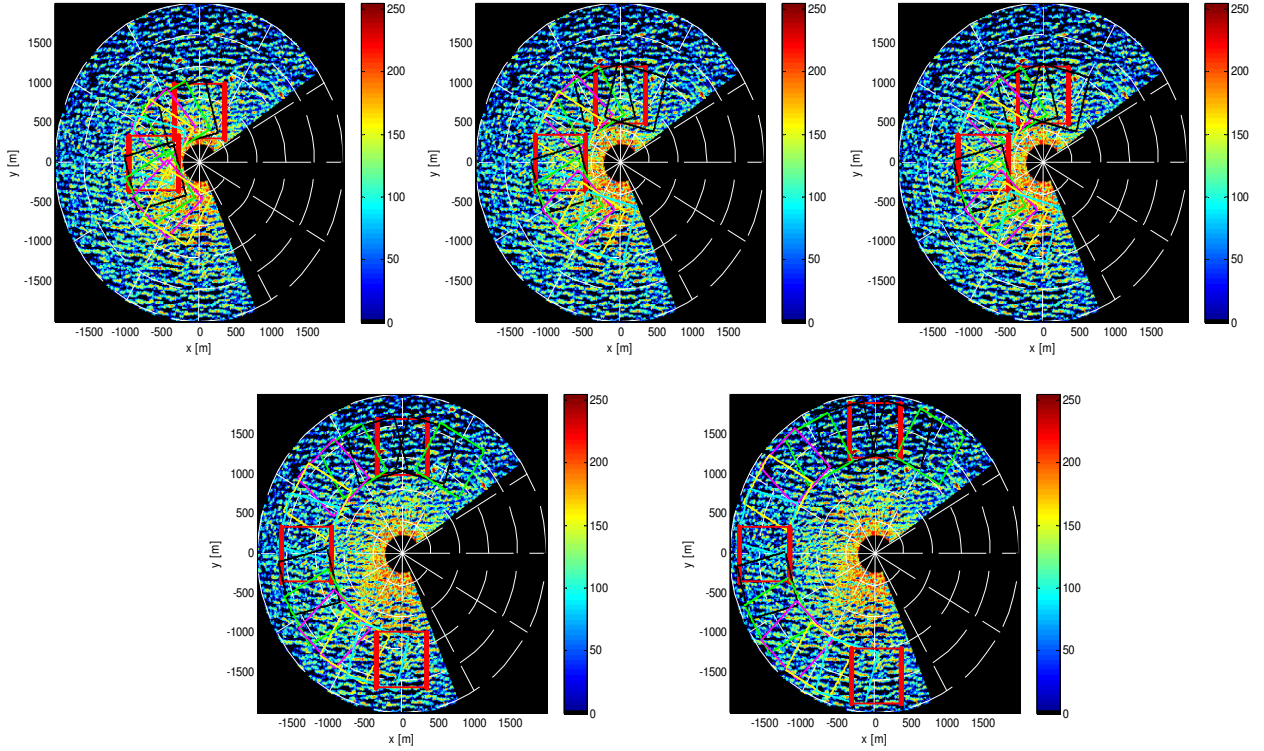
Figure 4.18: Example of all the windows to be evaluated for each radar image.

short range $R1$ the intensity collected is higher than in the rest, and the behaviour of the curves are similar, being maxima in the main direction 121º and minima in cross direction respect to the main direction or the wave direction. Seen the tendency of the curves, it can be said that the other maxima are in wave direction as well. The mean of the 3D spectrum is represented by the picture down on the left in 4.22 and the greatest curve correspond to short range $R1$ and the maxima values for all the curves are nearby cross direction (211º) respect to the wave direction, the background in this azimuths have more intensity and the dispersion shell is not define properly. In the last subimage, down on the right, there is the mean of the 2D spectrum in $\mathbf{k}_{max}$ direction. In all data set analysed has been found the same fact, that is that the result for range $R2$ are unexpected because it has not the same bahaviour than the rest of the curves, for some random azimuths the curve declines a lot. However, the rest of the curves are similar being the mean of the spectrum higher in short range $R1$ and poorest in far range $R5$. Following the tendency of the curve, it can be said that the minima will get in wave direction.

Table 4.2: Results obtained for all the azimuths for a fixed range $R3$.

Azimuths	I_{signal} [dB]	I_{3D} [dB]	I_{2D} [dB]	$I_{\text{dispersion}}$ [dB]
76º	18.33	-36.65	-18.01	34.74
91º	18.37	-37.53	-17.50	34.79
106º	18.58	-35.53	-17.28	34.62
121º	**18.55**	**−34.99**	**−17.33**	**34.67**
136º	18.49	-35.55	-17.71	34.31
151º	18.54	-35.79	-17.39	34.19
166º	18.53	-37.20	-17.58	33.52
181º	18.52	-35.11	-17.50	32.74
196º	18.52	-35.46	-17.85	31.91
211º	18.42	-31.53	-18.13	31.91
226º	18.32	-32.17	-18.14	31.99
241º	17.95	-31.72	-18.85	32.50
256º	17.64	-36.13	-18.98	32.93
271º	17.53	-37.51	-19.41	32.85
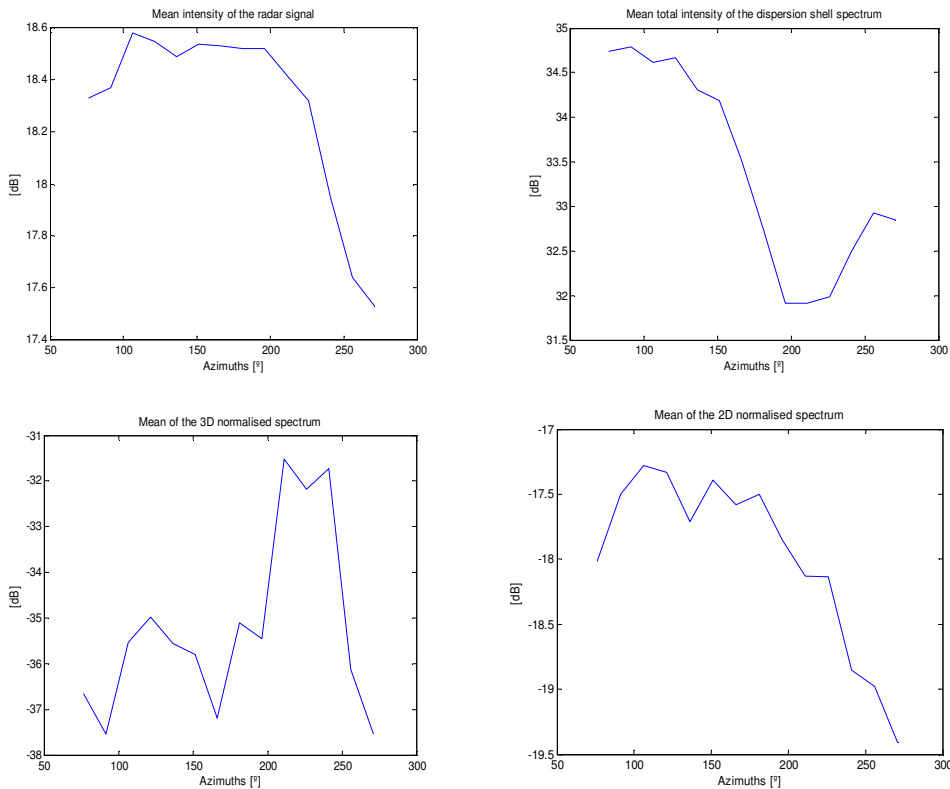
Figure 4.19: The graphic above on the left, is the mean intensity of the radar signal. Above on the right, it is the mean intensity contained in the 3D spectrum of the dispersion shell. Down on the left, it is the mean of the 3D spectrum, and on the right it is the mean of the 2D spectrum.
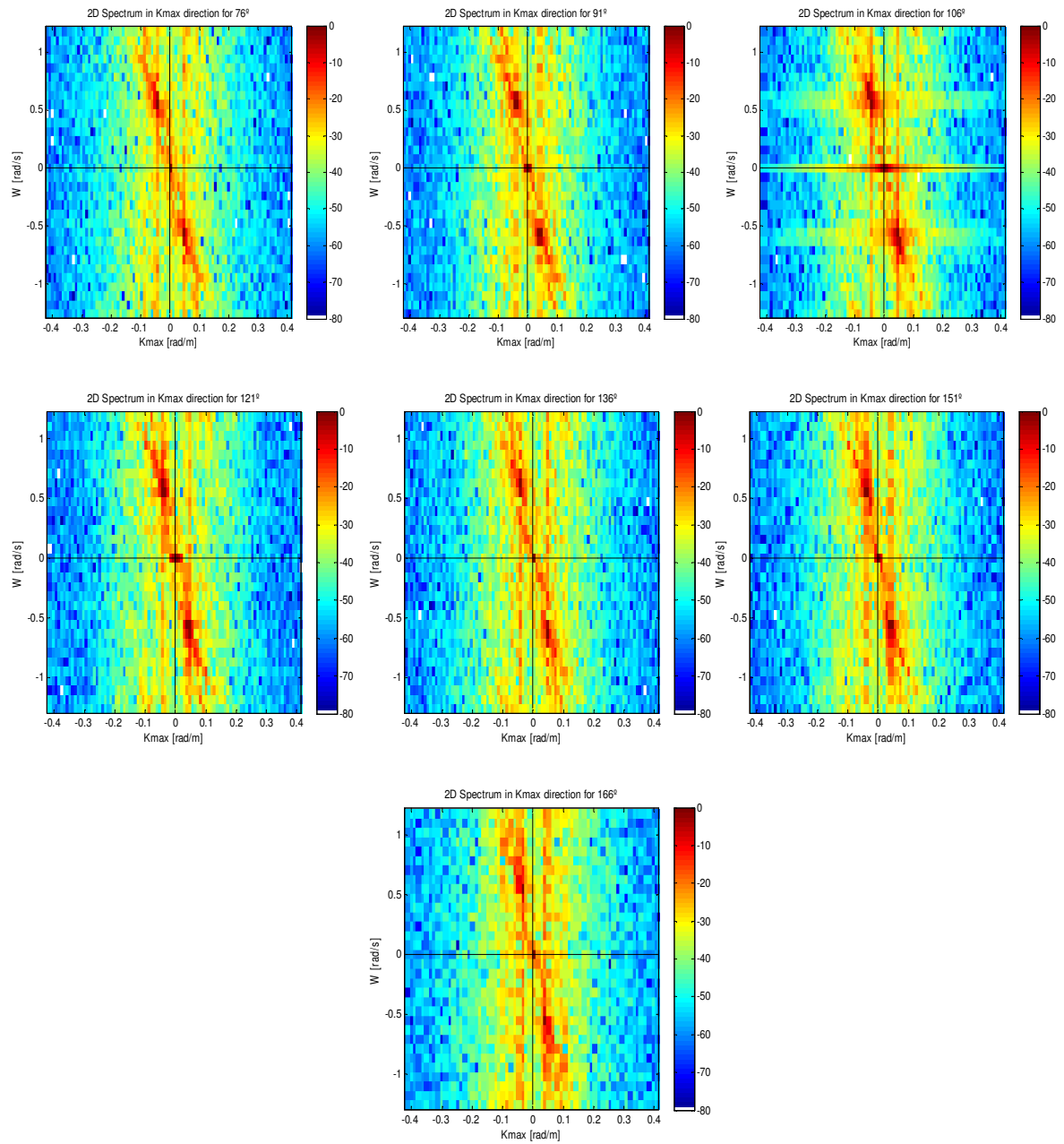
Figure 4.20: 2D spectra for **k** in the direction of the maximum for the azimuths between 76º and 166º for the R3 range.
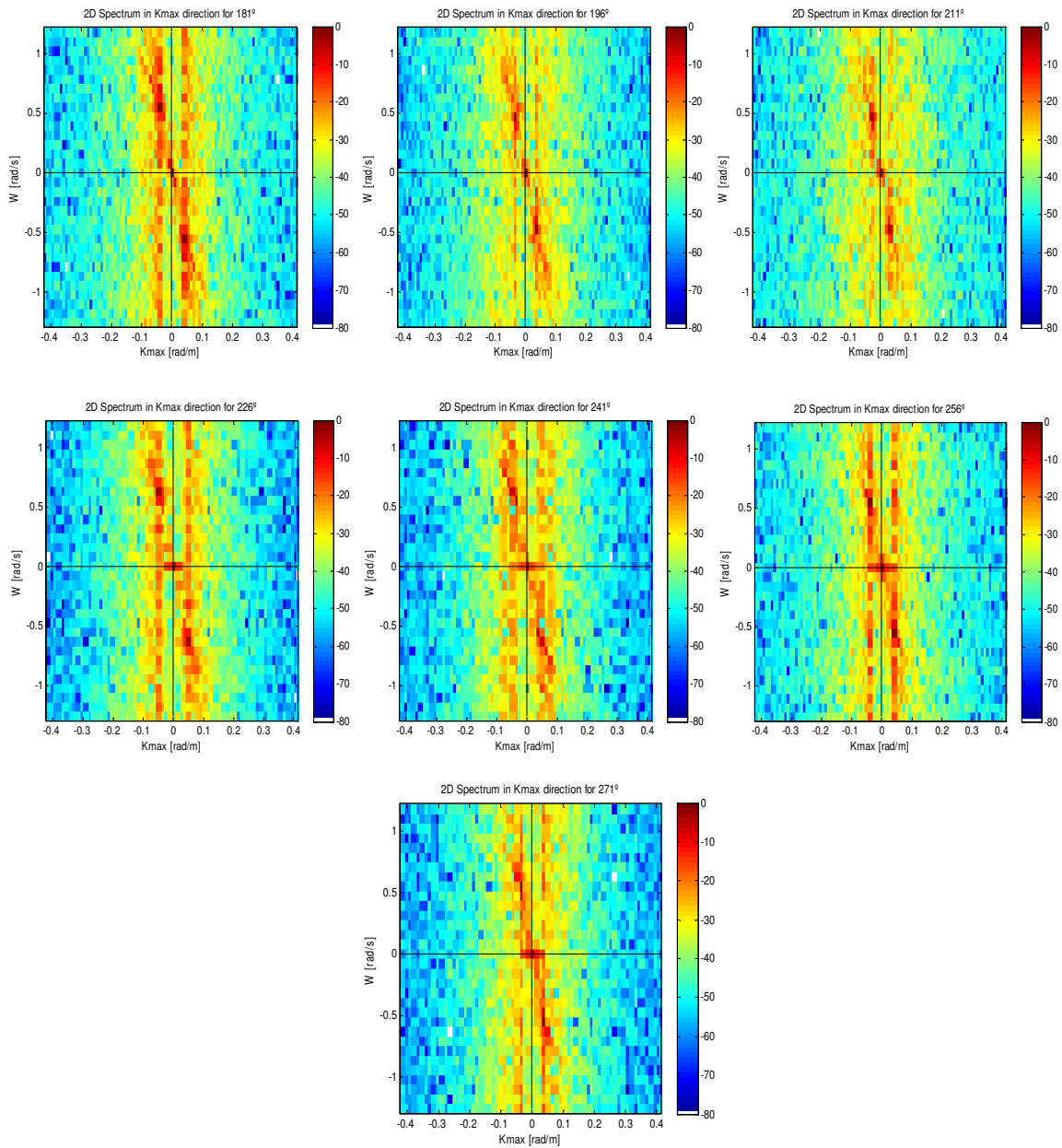
Figure 4.21: 2D spectra for **k** in the direction of the maximum for the azimuths between 181º
and 271º for the $R3$ range.
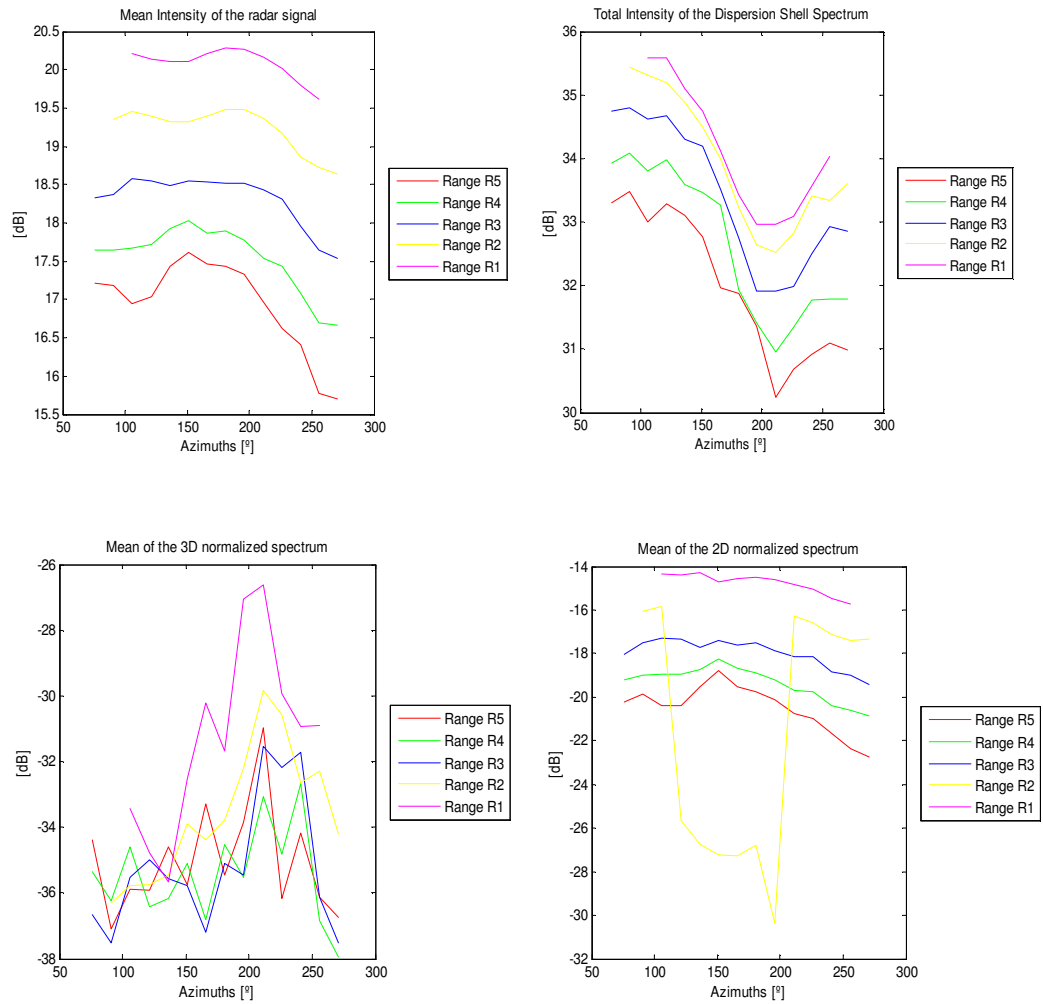
Figure 4.22: Comparison for all ranges and all azimuths under study. Each curve represents one range for all its azimuths.

Chapter 5

Group Line Dependence on the Radar Azimuth and Range Changes

This chapter is based on the previous one 4 but the target of the study is the one of the features in the image spectrum that are not yet well understood. In the context of the radar measurement of the sea surface, this feature is known in the literature as *group line* [29, 30]. The theoretical and adaptive filter, the interpolation, the background spectral noise, etc. explained in chapter 4, will be considered as well in this chapter and in the following 6.

5.1   Group line definition

There is not a conclusive definition of the group line, because still now the origin of the group line is unknown. Some scientists assert that the group line is caused by the capillary waves and other effects such as sea foam, bubbles, etc. However there are more opinions regarded to waves and dispersion shell. In addition of those phenomena that can cause the existence of the group line, some non linear features of the wave field dynamics appear as well where the group line is located [31]. Furthermore, as it is shown in further chapter 8, the shadowing modulation induces additional spectral features on form of subharmonics of the dispersion relation, which is the location of the group line. The group line is an evident phenomenon visible in the image spectra, which is located for very low angular frequencies. The intensity and the position of this spectral feature are different according to the wave direction and the strength of the waves. How it was before seen, in figure 3.6 all the visible phenomena in the spectrum are depicted, and the group line as well. Hence, the group line is an important feature that appear in the image spectrum that should be analysed for a better understanding of the microwave backscattering phenomenon on the sea surface at grazing incidence conditions.

In the same way that a filter to extract the dispersion shell and the first harmonic have been implemented, a filter to take out the group line was carried out as well. In this case, the filter works with the original spectrum of the radar image $\hat{F}_{\psi}^{(3)}(\mathbf{k}, \omega)$ without the contributions

of the dispersion shell and the first harmonic. So, the maximum reminded in the spectrum is related to the group line. Hence, the filter searches the maximum of the group line for $\omega \in [-0.2, 0.2]$ rad s^{-1}. Taking into account the ω-plane where the maximum is, the filter does a sweep in each ω-plane considering all the positions which have a energy proportional to the maximum. This proportion is not fixed, this proportion changes according to the ω-plane.
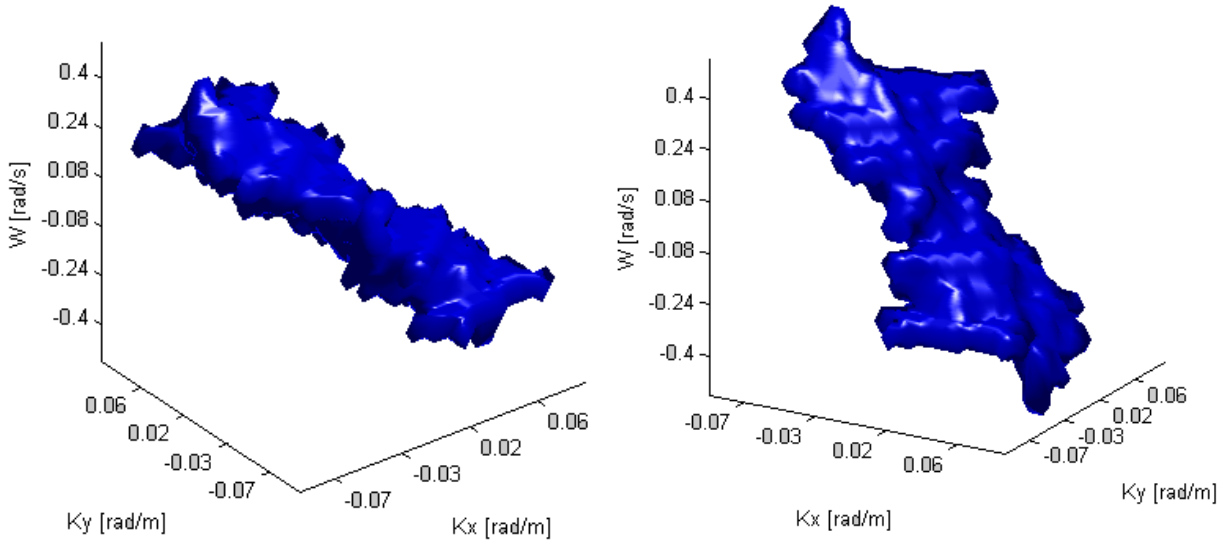
Figure 5.1: Example of group line extracted in a analysed window for FINO 1 data with $U_x = -0.38$ m s^{-1}, $U_y = -0.40$ m s^{-1} and $d = 30$ m.

The group line energy for low and high frequencies in this interval is low, however for frequencies close to 0 ($\omega \approx 0$), the energy is high. But sometimes the group line extraction is not very easy, because it depends of the wave direction and the range respect to the radar. In some directions, the extraction of the group line is impossible. And sometimes, the size of the group line exceeds the limits of the previous interval, being very close to the ω's belonged to the dispersion shell. These peculiarities are shown in section 5.3. An example of group line can be seen in figure 5.1. In this image the group line is bigger than the supposed ω's interval.

5.1.1   Group line as a nonlinear phenomenon

The uncertainty of the group line origin and the different versions about it make difficult its study. As the group line is a subharmonic of the dispersion relation (i.e. the fundamental mode), this work proposes that the group line could be obtained by subtracting the different $(\mathbf{k}, \omega)$-components belonging to the wave field, which are located within the dispersion shell. Therefore, two frequencies of the wave field (ω_1 and ω_2) and their corresponding wave numbers ($\mathbf{k}_1$ and $\mathbf{k}_2$), where $\omega_1 = \varpi(\mathbf{k}_1)$, $\omega_2 = \varpi(\mathbf{k}_2)$, interact nonlinearly between each other by their corresponding differences. Hence, the spectral components of the group line ($\mathbf{k}_{GL}, \omega_{GL}$) are derived as

$$\mathbf{k}_{GL} = \mathbf{k}_2 - \mathbf{k}_1 = (k_{x_2} - k_{x_1}, k_{y_2} - k_{y_1}) \tag{5.1}$$

$$\omega_{GL} = \omega_2 - \omega_1 \tag{5.2}$$

being

$$\omega_1 = \sqrt{gk_1 \ \tanh(k_1 d)} + \mathbf{k}_1 \cdot \mathbf{U}$$

$$\omega_2 = \sqrt{gk_2 \ \tanh(k_2 d)} + \mathbf{k}_2 \cdot \mathbf{U}$$

In figure 5.2 the subtraction of the two frequencies of the wave field belonged to the dispersion relation is represented in green colour and the subtraction coincides with the group line in two-dimensional. In the most of the cases, or windows under study, the group line can be considered
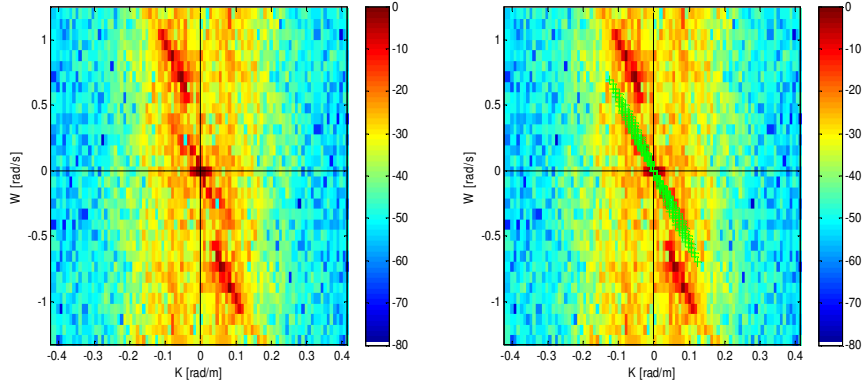
Figure 5.2: Example of group line considered as a subharmonic of the dispersion relation. On the left, the two-dimensional spectrum for a window under study. On the right, the same figure on the left but with the group line calculated as it is described on the text.

as a subharmonic, but in some directions referred to the wave direction, this assumption is not possible. In section 5.3 this consideration will be examined carefully.

5.2 Processing of the whole radar images

The whole radar images sequences are evaluated following the same process presented in 4.5 for the dispersion shell. The figures 4.9 and 4.10 in the chapter 4 are the starting points as well, because the same data set used before in the previous chapter 4 are going to continuous employed in this chapter and in the next to estimate the SNR.

At this point, the spectrum of the data set is obtained and the dispersion relation and the first harmonic has been removed. Then the spectrum of the radar image $\hat{F}_\psi^{(3)}(\mathbf{k}, \omega)$ will be subjected again for another filter to take out the group line, how it was commented previously in section
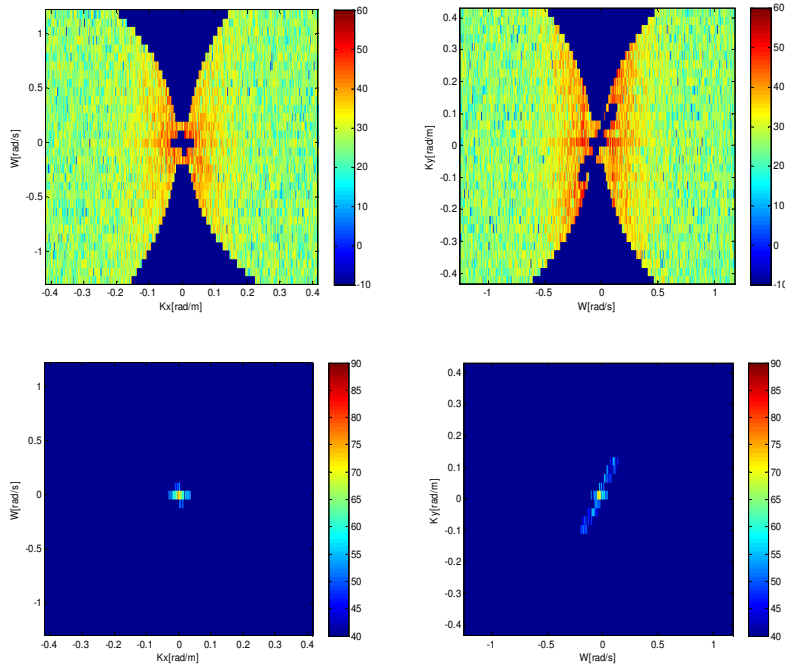
Figure 5.3: Extraction of the group line from the spectrum of the radar images. The picture in the first row, on the left, depicts a cut in the 3D-spectrum for $k_y = 0$ rad m^{-1} axis, and the picture on the right represents a cut in the 3D-spectrum for $k_x = 0$ rad m^{-1} axis. The second row shows the group line for the same cuts than above row.

5.1. In figure 5.3 it is depicted the extraction of the group line, the dark blue colour in the upper row represents the positions of the group line that have been removed. Two different axis transects are shown, being the $k_y = 0$ rad m^{-1} the first transect represented and the second transect is $k_y = 0$ rad m^{-1}. In the bottom row it is represented only the group line that have been extracted for the same transects, where the group line can be observed clearly.

Figure 5.4 represents the group line extracted from the whole radar image spectrum. The group line is located for low values of ω.

The last step is doing the Inverse Fast Fourier Transform to the interpolated spectrum to obtain the resulting radar images. The resultant radar signal has a poor intensity level in compare with the original radar signal. In the figure 5.5 three different radar signal images are presented. The first picture on the left is the signal of the radar without dispersion shell, without group line and without the first harmonic, but in this case the interpolation has not been done. The picture of the centre is the same than the previous one but the interpolation has been carried out. And the last picture on the right represents the mean of all the 32 images without dispersion shell, without group line and without the first harmonic, but with the interpolation done. It means, the mean of all the 32 images for the picture in the centre. Even after doing the complete process, it is possible to see some waves in the radar imagery.
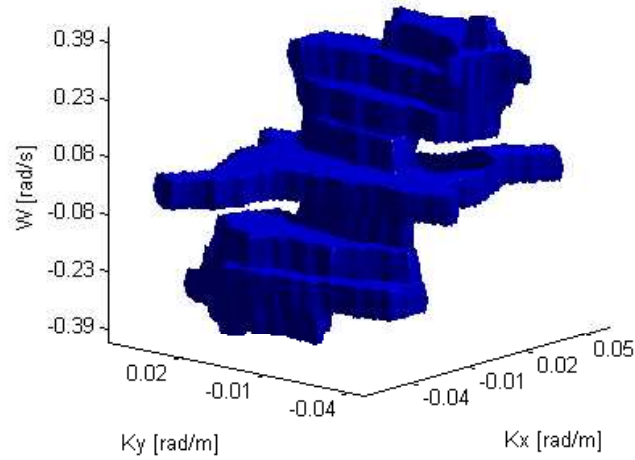
Figure 5.4: Group line removed from the spectrum after the filtered process.
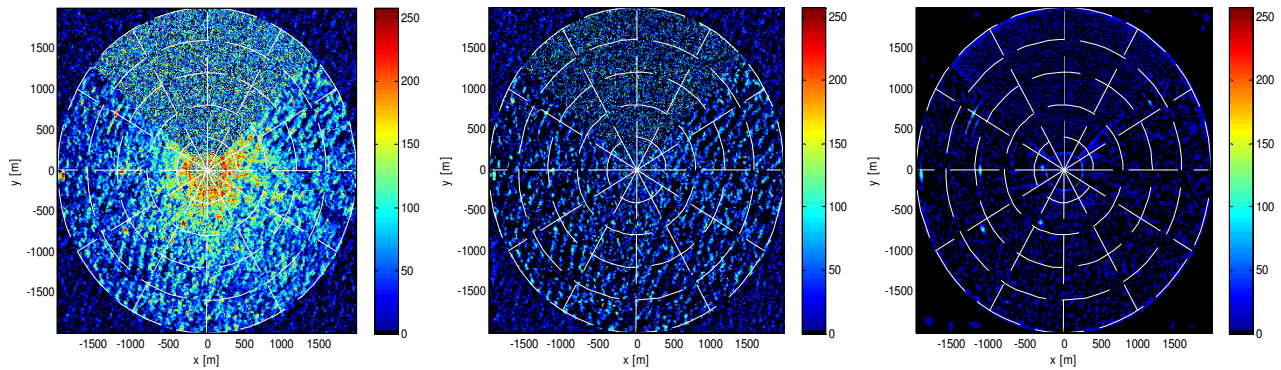
Figure 5.5: On the left, the output radar image in the same instant of time than 4.9 without doing the interpolation. In the picture of the centre, the output radar image for the same instant of time after all the process, interpolation included. On the right, the mean of all the 32 output radar images with interpolation process done.

5.3   Window analysis of the radar images for the group line

This section is a continuation of the section 4.6 in chapter 4 but focus on the study of the group line. In a briefly way, five ranges are contemplated, from near range (300 m) until far range (1900 m), covering in each range 700 m. There is a small overlap between two consecutive ranges, hence the whole range is covered efficiently. The possible azimuths under study are included in the interval [69º - 285º], and the rest of the angles (it means, from 0º to 68º and from 286º to 359º) belongs to the blanked areas. The angles sweep done for the azimuth takes the angles separated 15º from the wave direction provided by the WaMoS II system. For this

analysis, the blanked parts are not filled by speckle noise, but the blanked areas are ignored.

For each window, the group line is studied and the main characteristic is the mean intensity contained in the 3D spectrum of the group line.

Firstly, the research about the detection of the group line with the range will be examined. Then, the group line will be evaluated according to the azimuth.

5.3.1   Range study

How it was commented before in chapter 4, the whole radar image has been demarcated according to the range in five different regions: $R1$ (300 m - 1000 m), $R2$ (500 m - 1200 m), $R3$ (750 m - 1450 m), $R4$ (1000 m - 1700 m) and $R5$ (1200 m - 1900 m).

The figure 4.15 shows this five windows, one in each direction, where the group line is analysed. The table 5.1 collects the values of the mean intensity contained in the 3D spectrum of the the group line for each window in different ranges.

Table 5.1: The mean intensity contained in the 3D spectrum of the group line for the different ranges.

R1	R2	R3	R4	R5
40.98 dB	39.58 dB	38.22 dB	36.93 dB	35.79 dB
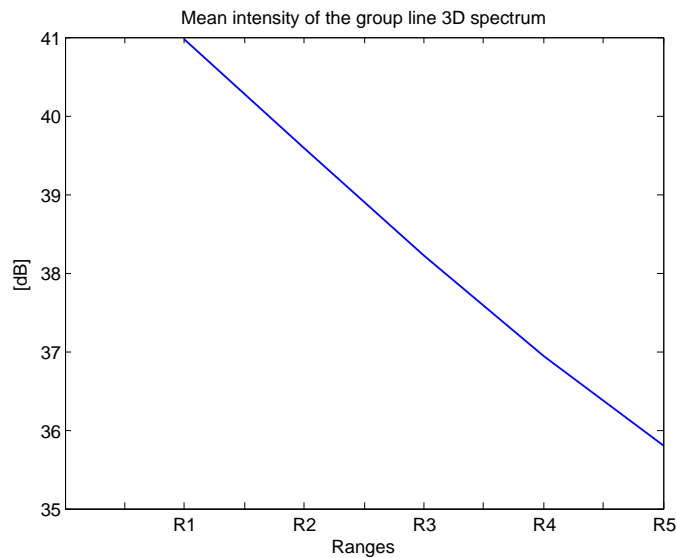
Figure 5.6: The mean intensity contained in the 3D spectrum of the group line for the different ranges under study.

The table 5.1 can be represented as the figure 5.6. In both of them, it can be realised that the mean intensity of the 3D spectrum the group line is greater in short range $R1$ and lower in far range $R5$. The closer it is, the more intensity group line has. Remembering the figure 4.17

where the mean intensity of the spectrum in 2D for $\mathbf{k}$ in the direction of the maximum ($\mathbf{k}_{max}$) is presented, the group line is clearly define in far range $R5$, however in short range $R1$, the group line and the dispersion shell seem united. The main problem in short range is to extract the group line without taking small piece of energy of the dispersion shell.

5.3.2 Azimuth study

Table 5.2: The mean intensity contained in the 3D spectrum of the group line for all the azimuths for a fixed range $R3$.

Azimuths	I_{GL} [dB]
76º	37.34
91º	37.27
106º	37.87
121º	**38.22**
136º	38.10
151º	37.97
166º	38.05
181º	38.08
196º	37.72
211º	36.98
226º	36.67
241º	36.24
256º	36.07
271º	36.01

As it was done previously for the azimuth analysis for the dispersion relation in 4.6.2, the figure 4.18 represents all these windows where the group line is going to be analysed as well. Taking into account the same considerations in 4.6.2, the range $R3$ will be prearranged to carry out the development in all the azimuths. How it was commented before, for this specific data set, the wave direction is in the blanked area, so it is considered the coming-from criterion, being the main direction the azimuth corresponding to the opposite of the wave direction (121º in this case).

A similar table 5.2 than 5.1 is presented but for all azimuth for the range $R3$. The characteristic under study is the mean intensity of the 3D spectrum contained in the group line. The figure 5.7 represents the values included in the table 5.2. The tendency of curve is maximum nearby the main direction 121º and decreases from the azimuth belonging to the cross direction, getting a minimum nearby wave direction 301º.

In the figures 5.9 and 5.10 all the spectra $\hat{F}_{\psi}^{(3)}(\mathbf{k}_{max}, \omega)$ in the direction of the maximum are depicted. In all of them the theoretical dispersion shell, in red line, and the group line calculated as a subharmonic, in green colour, have been superimposed. This shows that the group line can be considered as a subharmonic of the dispersion relation ($\omega_{GL} = \omega_2 - \omega_1$). The intensity of
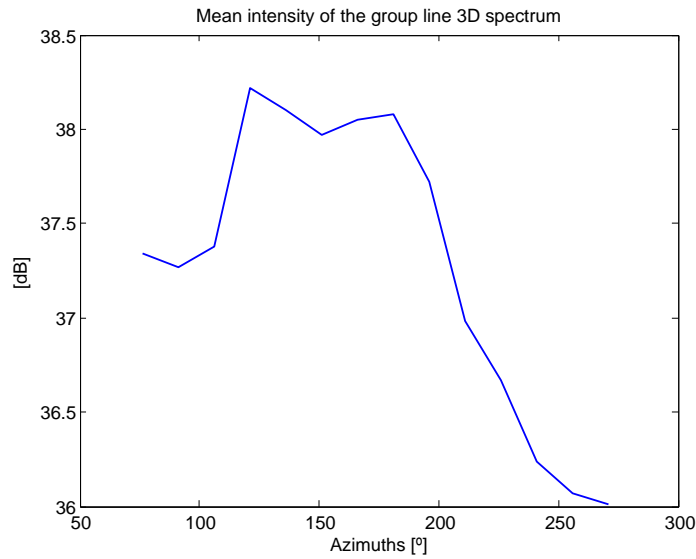
Figure 5.7: The mean intensity contained in the 3D spectrum of the group line for all the azimuths for a fixed range $R3$.

the group line is greatest in the main direction (121º) and, it is supposed in the wave direction (301º) as well. The visibility of the group line is defined in the main direction (121º) and, it is supposed in the wave direction (301º) as well. However, in cross direction the group line is not defined and the intensity is weak, and even the background is more intense in these azimuths. Sometimes it is not possible to extract the group line in cross direction, or only removing a small part of it.
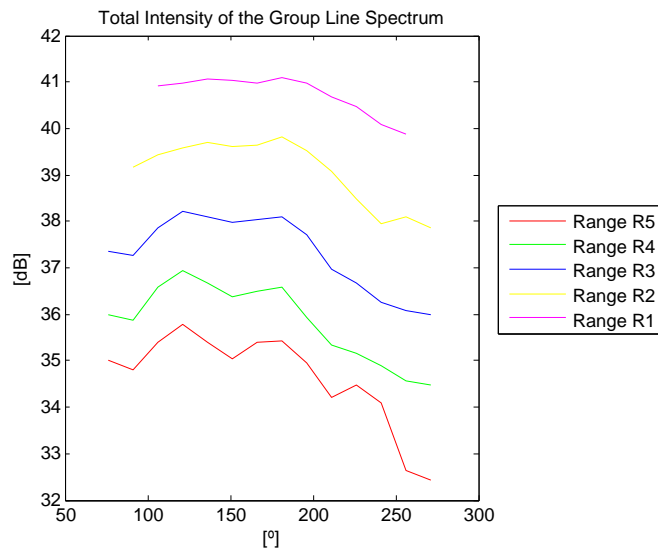
Figure 5.8: Comparison of the group line for all ranges and all azimuths under study. Each curve represents one range for all its azimuths.

This study for all the azimuths has been done for each range, from $R1$ to $R5$ and the results are shown in the figure 5.8. Five curves are presented, each curve represents the results obtained for each range for all the azimuths under study. It means, the pink curve represents the values obtained for all azimuths for short range $R1$, the yellow curve is the study done for $R2$, the blue colour describes the results for all azimuths in middle range (i.e. corresponding to the detailed study presented before), the green colour indicates the values got for range $R4$ and red colour for far range $R5$. The figure 5.8 represents the mean intensity contained in the 3D spectrum of the group line. For short range $R1$ the intensity collected is higher than in the rest, and the behaviour of the curves are similar, being maxima nearby the main direction 121º and decreasing in cross direction respect to the main direction or the wave direction. Seen the tendency of the curves, it can be said that the minimum is close to the wave direction.

In chapter 4 the aim of the study is the dispersion shell and in this chapter the target is the group line. But both them have a comparable energy inside of their spectra. That is why in figure 5.11 is depicted the subtraction of the mean of the intensities included in the 3D spectra of the group line minus the dispersion shell. The mean intensity of the spectrum of the group line is higher than the mean intensity of the spectrum of the dispersion relation. For far range $R5$ the subtraction is fewer than for short range $R1$. Besides, all the curves have the same tendency, where the minima are nearby the azimuths corresponding to main direction and wave direction. However, the maxima values are close to the azimuths around cross direction.
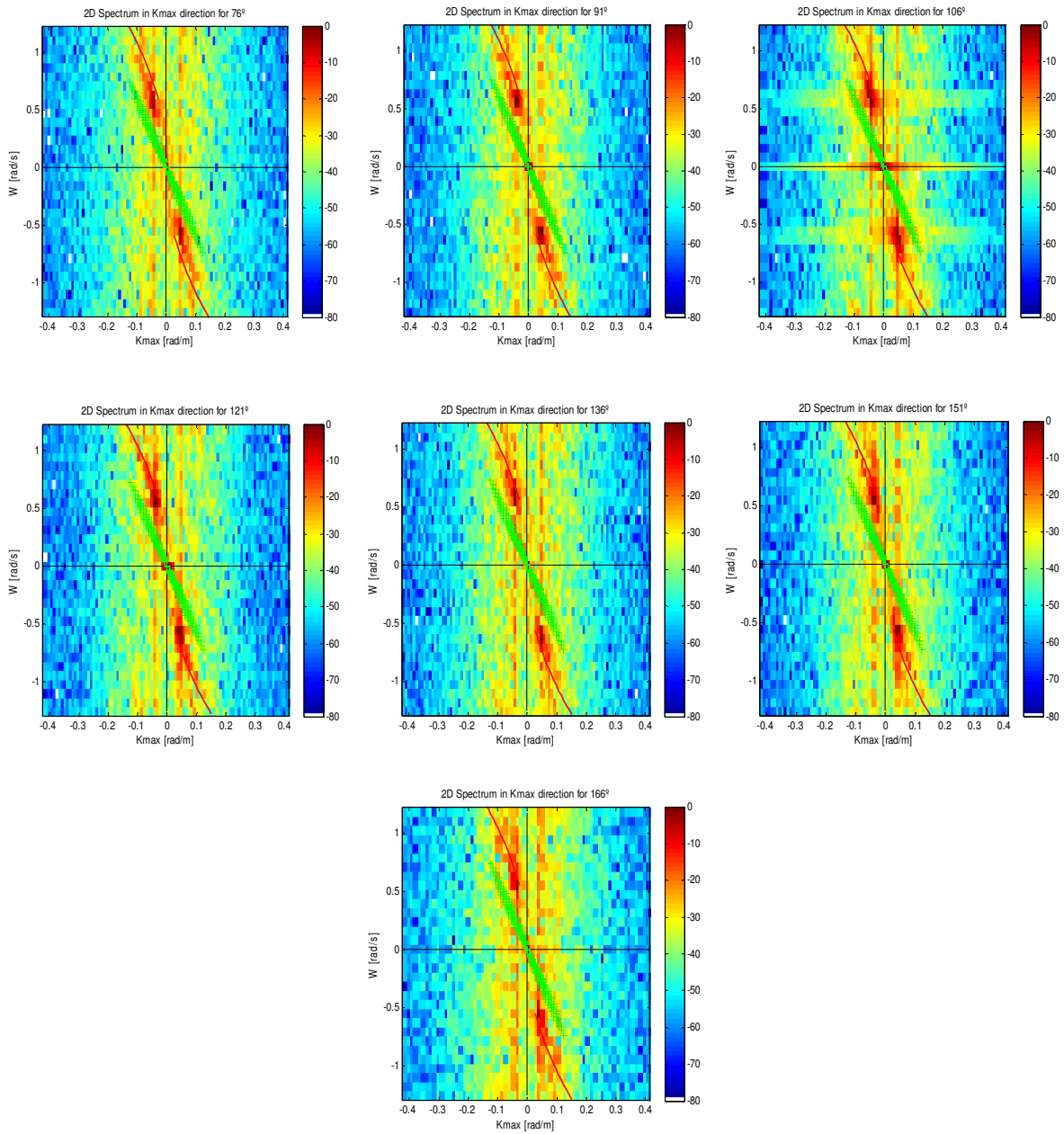
Figure 5.9: 2D spectra for the direction of the maximum **k** for the azimuths between 76º and 166º for the $R3$ range.
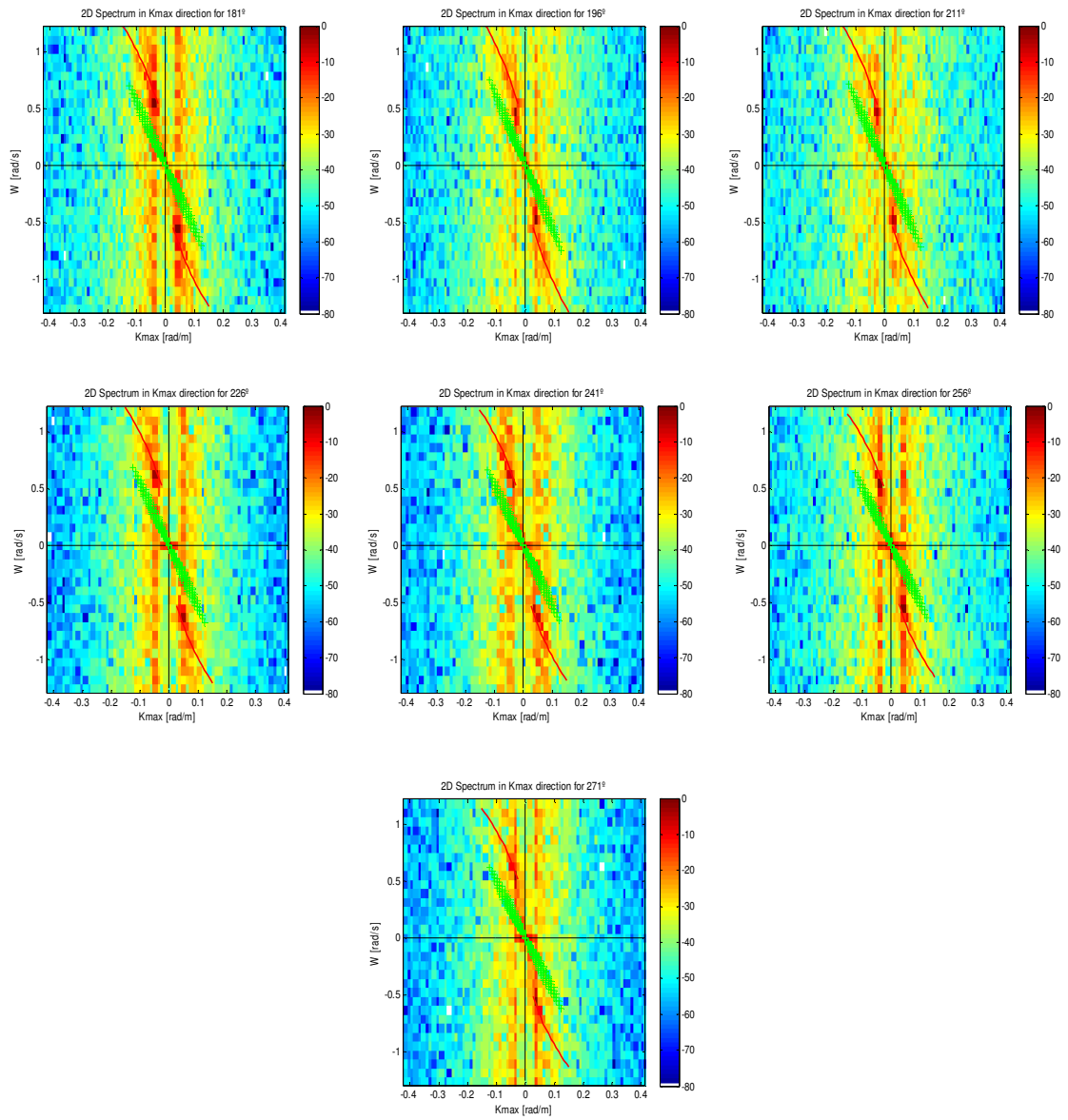
Figure 5.10: 2D spectra for the direction of the maximum **k** for the azimuths between 181º and 271º for the $R3$ range.
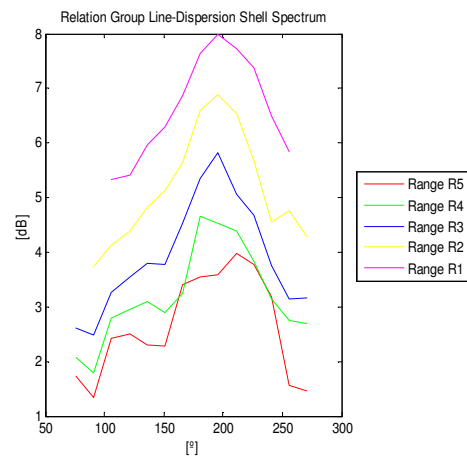
Figure 5.11: Subtraction of the group line minus the dispersion relation.

Chapter 6

Signal to Noise Ratio Behaviour According to the Azimuth and Rage of the Radar

This chapter is focus on the behaviour of the *Signal to Noise Ratio* (*SNR*) conforming to the azimuth and the range, in a similar manner than the chapters 4 and 5 for the dispersion shell and the group line. But firstly the importance of *SNR* in radar data and images is going to be shown.

6.1   The significance of Signal to Noise Ratio

The *SNR* is one of the most important parameter in radar because of the usefulness to estimate the *significant wave height* (H_s). In section 3.4.3 the estimation of H_s is calculated with the linear model as:

$$H_s = c_0 + c_1\sqrt{SNR}$$

Where the *SNR* expression (3.26) takes, for the signal, the energy of the spectral components of the wave field image and for the noise, the total spectra background energy of the three-dimensional image spectrum:

$$SNR = \frac{\displaystyle\int_{\Omega_{\mathbf{k},\omega}} \widetilde{F}^{(3)}(\mathbf{k},\omega)\,\mathrm{d}^2k\,d\omega}{\displaystyle\int_{\Omega_{\mathbf{k},\omega}} F_{BGN}^{(3)}(\mathbf{k},\omega)\,\mathrm{d}^2k\,\mathrm{d}\omega}$$

But by the moment, there is not a perfect filter to extract perfectly the signal and considering the rest as noise. This is the reason because the value got for H_s is not so accurate and the essential motive to try to determine the H_s using *artificial neural networks* (ANN) from the data and images provided by the WaMoS II software.

In [12, 32] an estimator of H_s based on artificial neural networks is proposed. The ANN can implement a proper non-linear function between the input space (sea states parameters) and the output space (the target, H_s). The estimator takes the corresponding sea state parameters given by the WaMoS II system, being the most important:

- Peak wavelength (λ_p): This is the wavelength related to the wave number $k_p = 2\pi/\lambda_p$, where the spectrum $F(k)$ is maximum.

- Peak period (T_p): This is the wave period associated to the frequency $\omega_p = 2\pi/T_p$, where the spectrum $S(\omega)$ is maximum.

- Mean period (T_{m02}): This is calculated as:

$$T_{m02} = \sqrt{\frac{m_0}{m_2}}$$

  The parameters m_0 and m_2 are the zeroth and second order moments of the wave spectrum (section 2.3.3).

- Wave age (WA): It is a general measurement that expresses the conditions of the waves and their development. This parameter can be calculated as [33]:

$$WA = \frac{g}{2\pi \cdot f_p \cdot U_{10}}$$

  where g is the acceleration of gravity, f_p is the peak frequency ($f_p = 1/T_p$) and U_{10} is the wind speed measured at 10 m over the mean sea level.

- Signal to Noise Ratio ($\sqrt{SNR_R}$): In this case, this SNR_R depends on the integration thresholds. There are four different estimations of SNR, and this magnitude is distinct than the SNR expected.

The data used are provided by two different platforms supplied by the WaMoS II system: FINO and Ekofisk. To complement the sea state parameters derived from the WaMoS II system, DataWell WaveRider buoys are used as well. The buoys are moored in the vicinity of each platform saving waves elevation series and other sea states parameters synchronised.

The ANN employed are the *Multilayer Perceptrons* (MLPs) because they can implement non-linear functions based on the non-linearity properties of the sea clutter. Firstly, a study to determine the size and the topology of the ANN is developed, according to obtain the least *mean squared error* (mse), the difference between the desired outputs and actual outputs obtained from the network, and not very high computational load. For this reason, the MLP contemplated topology is 3 neurons in the input corresponding to sea state parameters, 15 neurons in the hidden layer and 1 neuron for the output layer corresponding to the H_s.

Secondly, diverse combinations of these sea state parameters as an input vector are generated to achieve the best solution, the best estimator. In these studies are collected all the possible
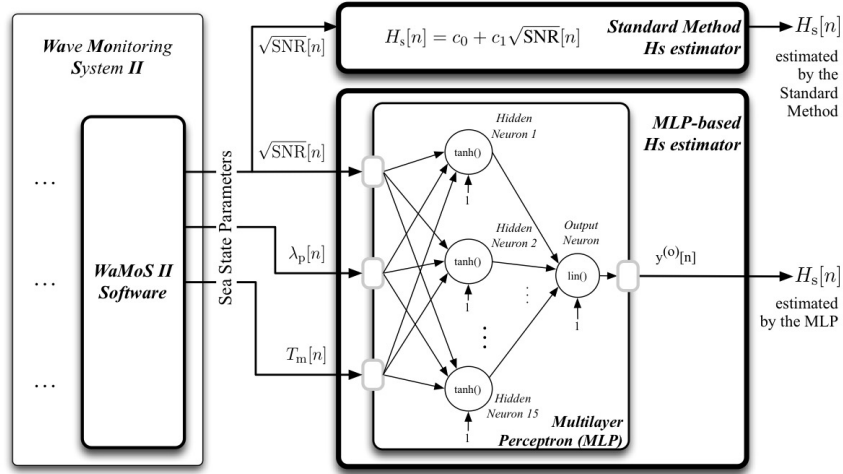
Figure 6.1: Scheme of the H_s estimator based on ANN. Adapted from [32].

combinations among these sea state parameters and it was obtained that the best combination was SNR, λ_p and T_{m02}. Hence, the input vector in $n\text{-}domain$, which represents the time scale of the sea state temporal evolution, is:

$$x[n] = \left[\sqrt{SNR[n]}, \lambda_p[n], T_{m02}[n] \right] \tag{6.1}$$

The ANN provides directly the estimation of the H_s as:

$$H_{s\text{ANN}}[n] = \gamma^{(\text{OUT})}[n] = f_{\text{ANN}}(x[n]) \tag{6.2}$$

This function $\gamma^{(\text{OUT})}$ is a combination of matrix and vectors of the bias ($\mathbf{b}$ and b) and the weights ($\mathbf{W}$ and $\mathbf{w}$) of the different layers of the ANN. In this concrete case, the $\gamma^{(\text{OUT})}$ can be expressed as:

$$\gamma^{(\text{OUT})} = \text{purelin}\left(\mathbf{w}^{(\text{OUT})} \cdot \left(\text{tansig}\left(\mathbf{W}^{(\text{HIDDEN})} \cdot x + \mathbf{b}^{(\text{HIDDEN})} \right) \right) + b^{(\text{OUT})} \right) \tag{6.3}$$

being tansig$(\cdot)$ a sigmoid tangent activation function in the hidden neurons and purelin$(\cdot)$ a pure linear activation function in the output neuron. In the Annex B a briefly synopsis related to the ANN is explained.

Finally, the results obtained for both source of data are optimum, especially for the data from FINO 1, where the error standard deviation has been reduced and the correlation coefficient has been increased. These can be seen in the figures 6.2 and 6.3. In both figures a comparison among the measures of the buoy, the standard method and the ANN-estimator is presented, and it is possible to see the improvements.
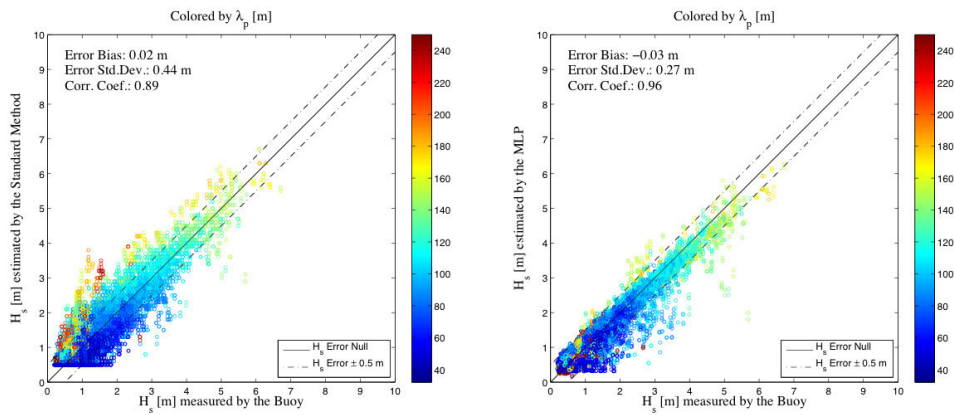
Figure 6.2: Scatter plot of the H_s measure by the buoy versus H_s estimated by the standard method on the left, and the scatter plot of the H_s measure by the buoy versus H_s estimated by the proposed ANN-based estimator on the right for FINO 1 data set.
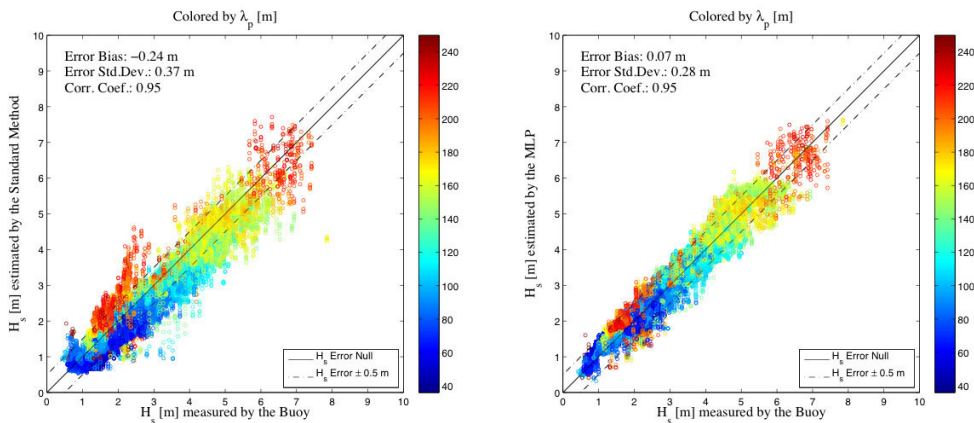
Figure 6.3: Scatter plot of the H_s measure by the buoy versus H_s estimated by the standard method on the left, and the scatter plot of the H_s measure by the buoy versus H_s estimated by the proposed ANN-based estimator on the right for Ekofisk data set.

6.2 Signal to Noise Ratio according to the azimuth and rage of the radar

Signal to Noise Ratio is one of the most important parameter to be considered. In this case, as it was commented in the previous chapters, *Signal* will be mainly the relation dispersion owing to the waves. Nevertheless *Noise* will be the background noise. But the main problem is that, in the spectrum, there are more phenomena caused by the waves, such as the first harmonic

and the group line. But sometimes, the group line could be considered as a signal or as a noise. Therefore, some different *Signals* and *Noises* will be studied according to these phenomena and the interpolation. The *Signals* have been classified according to the group line, theoretical and adaptive filter and the use of the *Modulation Transfer Function* (MTF):

- Without considering the group line. In this case, the group line is part of the noise.

  - S_1: Signal due to the dispersion shell filtered by the three-dimensional pass-band filter without MTF.
  - S_2: Signal due to the dispersion shell filtered by the three-dimensional pass-band filter with MTF.
  - S_3: Signal due to the dispersion shell filtered by the adaptive filter without MTF.
  - S_4: Signal due to the dispersion shell filtered by the adaptive filter with MTF.

- Considering the group line. In this classification, the group line is part of the signal waves.

  - S_5: Signal due to the dispersion shell filtered by the three-dimensional pass-band filter without MTF.
  - S_6: Signal due to the dispersion shell filtered by the three-dimensional pass-band filter with MTF.
  - S_7: Signal due to the dispersion shell filtered by the adaptive filter without MTF.
  - S_8: Signal due to the dispersion shell filtered by the adaptive filter with MTF.

The *Noises* have been classified according to the interpolation and the group line:

- Without considering the interpolation of the removed signal.

  - N_1: Noise without considering the group line.
  - N_2: Noise considering the group line.

- Considering the interpolation of the removed signal.

  - N_3: Noise without considering the group line. Only the dispersion shell is interpolated.
  - N_4: Noise considering the group line. The dispersion shell and the group line are interpolated.

The modulation transfer function (MTF) is related to the interaction of the ripple with long waves and it was mentioned in 3.4.2, where this function is

$$\mathcal{T}(\mathbf{k}) = k^{-1.2}$$

Therefore, there will be different *SNR* possible combinations ($SNR_{nm} = S_n/N_m$). In all these combinations, the first harmonic will be considered background noised, because the total spectra energy of these components is negligible comparing to the background noise energy [26].

But not all the SNR_{nm} combinations are possible, because if it is considered one of the Signals that consider that the group line is part of the noise (e.g. S_1, S_2, S_3, S_4), only the Noises that consider the group line as a noise have been chosen (e.g. N_2 and N_4). So the possible combinations employed here are the following:

- Signals that not consider the group line as a part of a signal (S_1, S_2, S_3, S_4) and Noises that consider the group line as a part of a noise (N_2 and N_4): SNR_{12}, SNR_{22}, SNR_{32}, SNR_{42}, SNR_{14}, SNR_{24}, SNR_{34}, SNR_{44}

- Signals that consider the group line as a part of a signal (S_5, S_6, S_7, S_8) and Noises that not consider the group line as a part of a noise (N_1 and N_3): SNR_{51}, SNR_{61}, SNR_{71}, SNR_{81}, SNR_{53}, SNR_{63}, SNR_{73}, SNR_{83}

6.3   The frequency wave spectrum $S(\omega)$

The number of SNR depending on what is considered Signal or what is considered Noise, give an idea that the SNR is not constant. What is more, the interpolation is a process to introduce another aleatory signal in parts of the spectrum that have been removed previously, and this signal is not constant. Therefore, to check if the method of interpolation works optimally, the best way is testing the frequency spectrum $S(\omega)$ which depends only on the angular frequency ω, which is associated with the time dependence of sea state.

Being $I(k_x, k_y, \omega)$ the marine radar image spectrum, it will be filtered and the dispersion shell will be removed. The dispersion relation will be the desired signal named $F(k_x, k_y, \omega)$. But the spectrum $I(k_x, k_y, \omega)$ can be filtered, removing the dispersion shell and besides, the empty space left by the dispersion shell could be refilled using a interpolation method, getting the interpolation noise spectrum $N(k_x, k_y, \omega)$.

In a theoretical way, it is supposed that:

$$F(\mathbf{k}, \omega) = I(\mathbf{k}, \omega) - N(\mathbf{k}, \omega) \tag{6.4}$$

It is considered that:

$$\tilde{F}(\mathbf{k}) = \sum_{\omega > 0} F(\mathbf{k}, \omega) \Delta \omega \tag{6.5}$$

And the frequency spectrum $S(\omega)$ can be obtained as:

$$S(\omega) = \sum_{k_x} \sum_{k_y} F(\mathbf{k}, \omega) \Delta k_x \Delta k_y \tag{6.6}$$

where the samples which obey $|\mathbf{k}| \leq \Delta k_x$ must be rejected.

Therefore

$$S(\omega) = \sum_{k_x} \sum_{k_y} (I(\mathbf{k}, \omega) - N(\mathbf{k}, \omega)) \Delta k_x \Delta k_y \tag{6.7}$$

6.4   Processing of the whole radar images

Continuing with the data set presented in the previous chapters 4 and 5, now the focus of the study is the *SNR* for the different acceptations described before in 6.2. Therefore, the *SNR*s under study are:

- SNR_{12}: Signal due to the dispersion shell and without group line filtered by the three-dimensional pass-band filter without MTF and Noise considering the group line but not considering the interpolation.

- SNR_{22}: Signal due to the dispersion shell and without group line filtered by the three-dimensional pass-band filter with MTF and Noise considering the group line but not considering the interpolation.

- SNR_{32}: Signal due to the dispersion shell and without group line filtered by the adaptive filter without MTF and Noise considering the group line but not considering the interpolation.

- SNR_{42}: Signal due to the dispersion shell and without group line filtered by the adaptive filter with MTF and Noise considering the group line but not considering the interpolation.

- SNR_{14}: Signal due to the dispersion shell and without group line filtered by the three-dimensional pass-band filter without MTF and Noise considering the group line and the interpolation.

- SNR_{24}: Signal due to the dispersion shell and without group line filtered by the three-dimensional pass-band filter with MTF and Noise considering the group line and the interpolation.

- SNR_{34}: Signal due to the dispersion shell and without group line filtered by the adaptive filter without MTF and Noise considering the group line and the interpolation.

- SNR_{44}: Signal due to the dispersion shell and without group line filtered by the adaptive filter with MTF and Noise considering the group line and the interpolation.

- SNR_{51}: Signal due to the dispersion shell and group line filtered by the three-dimensional pass-band filter without MTF and Noise without considering the group line neither the interpolation.

- SNR_{61}: Signal due to the dispersion shell and group line filtered by the three-dimensional pass-band filter with MTF and Noise without considering the group line neither the interpolation.

- SNR_{71}: Signal due to the dispersion shell and group line filtered by the adaptive filter without MTF and Noise without considering the group line neither the interpolation.

- SNR_{81}: Signal due to the dispersion shell and group line filtered by the adaptive filter with MTF and Noise without considering the group line neither the interpolation.

- SNR_{53}: Signal due to the dispersion shell and group line filtered by the three-dimensional pass-band filter without MTF and Noise without considering the group line but the interpolation is considered.

- SNR_{63}: Signal due to the dispersion shell and group line filtered by the three-dimensional pass-band filter with MTF and Noise without considering the group line but the interpolation is considered.

- SNR_{73}: Signal due to the dispersion shell and group line filtered by the adaptive filter without MTF and Noise without considering the group line but the interpolation is considered.

- SNR_{83}: Signal due to the dispersion shell and group line filtered by the adaptive filter with MTF and Noise without considering the group line but the interpolation is considered.

Table 6.1: Signals that not consider the group line as a part of a signal and Noises that consider the group line as a part of a noise.

	Value of SNR [dB]
SNR_{12}	0.14
SNR_{22}	2.30
$\mathbf{SNR_{32}}$	**0.10**
$\mathbf{SNR_{42}}$	**1.83**
SNR_{14}	0.13
SNR_{24}	2.22
$\mathbf{SNR_{34}}$	**0.10**
$\mathbf{SNR_{44}}$	**1.78**

Table 6.2: Signals that consider the group line as a part of a signal and Noises that not consider the group line as a part of a noise.

	Value of SNR [dB]
SNR_{51}	0.14
SNR_{61}	2.30
$\mathbf{SNR_{71}}$	**0.10**
$\mathbf{SNR_{81}}$	**1.83**
SNR_{53}	0.13
SNR_{63}	2.22
$\mathbf{SNR_{73}}$	**0.10**
$\mathbf{SNR_{83}}$	**1.78**

In the tables 6.1 and 6.2 the values of the SNR are collected, but they are separated according if the group line belongs to Signal or Noise. The values of SNR related to the adaptive filter are written in bold letters. The SNR values got by the adaptive filter are lower than those obtained

by the three-dimensional pass-band filter. Another observation is that applying the modulation transfer function, the value is greater, more than 1.5 dB. Looking at the results shown in tables 6.1 and 6.2 it can be seen that, although the individual values of the image spectrum for the group line spectral $(\mathbf{k}, \omega)$-components are comparable with the spectral values corresponding to the $(\mathbf{k}, \omega)$-components within the dispersion shell, the integral of those values does not affect significantly to the different estimations of SNR. That means that the important contribution to SNR came from the dispersion shell itself. Therefore, from the point of view of the effect of the group line in the H_s estimation, the use of $\sqrt{SNR}$ is a robust estimator, even for those cases where the filter is not capable of split completely all the $(\mathbf{k}, \omega)$-components related to the group line.

6.5 Window analysis of the radar images

In this chapter the windows analysis is concentrated in the SNR. To make it easier, the range and azimuth analysis is going to treat together. Summarising the previous facts, this section is a continuation of the section 4.6 in chapter 4 and 5.3 in chapter 5. Five ranges are contemplated, from near range (300 m) until far range (1900 m), covering in each range 700 m. There is a small overlap between two consecutive ranges, hence the whole range is covered efficiently. The possible azimuths under study are included in the interval [69° - 285°], and the rest of the angles (it means, from 0° to 68° and from 286° to 359°) belongs to the blanked areas. The angles sweep done for the azimuth takes the angles separated 15° from the wave direction provided by the WaMoS II system. For this analysis, the blanked parts are not filled by speckle noise, but the blanked areas are ignored.

6.5.1 Range and azimuth study

The figure 4.18 represents all windows where the SNR and the frequency spectrum $S(\omega)$ are going to be analysed. The different SNRs which are under study are explained previously with detail in 6.4. Hence, the figure 6.4 shows 8 pictures, which correspond to each SNR_{nm}. In each subplot five curves are presented, each curve represents the results obtained for each range for all the azimuths under study. It means, the pink curve represents the values obtained for all azimuths for short range $R1$, the yellow curve is the study done for $R2$, the blue colour describes the results for all azimuths in middle range, the green colour indicates the values got for range $R4$ and red colour for far range $R5$.

If these subplots are analysed in detail, it is got the following results:

- In the subplot of SNR_{12} and SNR_{22} the curves are similar, but for SNR_{22}, in which MTF is used, the level of the values are higher.

- The same happens for SNR_{32} and SNR_{42}. The curves are similar, but for SNR_{42}, in which MTF is used, the level of the values are higher.

- In the subplot of SNR_{14} and SNR_{24} the curves are similar, but for SNR_{24}, in which MTF is used, the level of the values of SNR are higher.

- The same happens for SNR_{34} and SNR_{44}. The curves are similar, but for SNR_{44}, in which MTF is used, the level of the values are higher.

- In all the subplot there are two things in common. Firstly, for near range the SNR is greater than for far range. And secondly the tendency of the curves are the equivalent. The SNR takes the lowest values for the azimuths around the cross direction, however the highest values are nearby the main direction (121º) and the wave direction (301º).

Apart of the SNR, the frequency spectrum $S(\omega)$ is analysed as well. The idea is to contrast that the dispersion shell that have been extracted is very similar to the subtraction between the original marine radar spectrum and the spectrum where the dispersion relation has been extracted and interpolated.

The figure 6.5 describes the evolution of the $S(\omega)$ in main direction (121º) for all the ranges, from $R1$, sited up on the left, to $R5$, sited down on the right. All subplots present a very well adjustment between the $S(\omega)$ of the dispersion shell, in red colour, and the subtraction of the original marine radar spectrum minus the interpolated spectrum, in green colour. Hence, the random interpolation in a similar way of the speckle noise here applied, works appropriately.

Now, the $S(\omega)$ is examined according to the azimuths prearranging the middle range $R3$. The figures 6.6 and 6.7 depict the results. The adjustment is very good for all the azimuths except for those azimuths around the cross direction from the wave direction. In this case, the azimuth corresponding to the cross direction is equal to 211º, and in this azimuth the extraction of the dispersion relation is more complicated because the dispersion relation is not so well defined and the noise of the background is a bit high in compare with the rest.
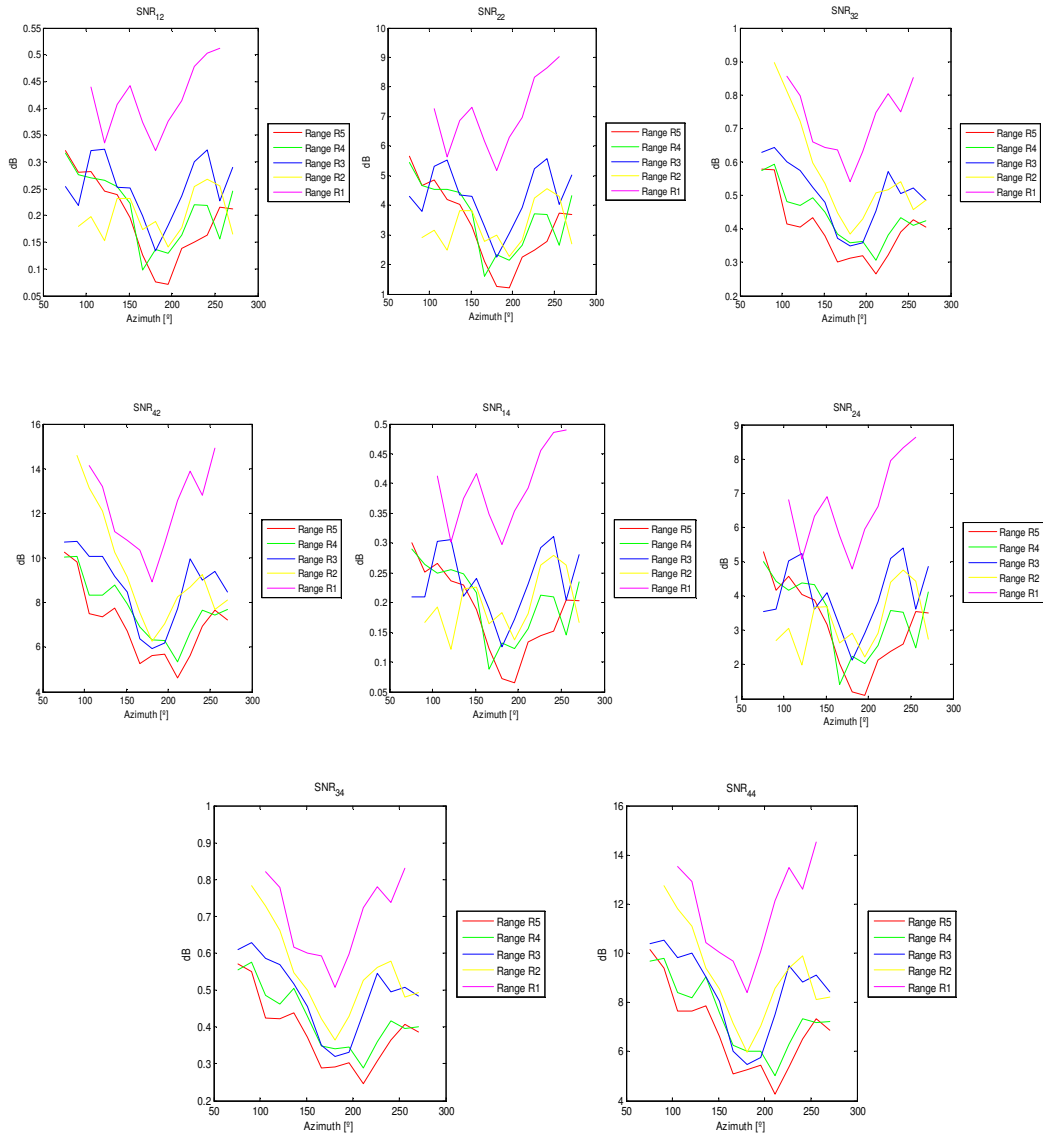
Figure 6.4: SNR_{nm} for all ranges and azimuths.
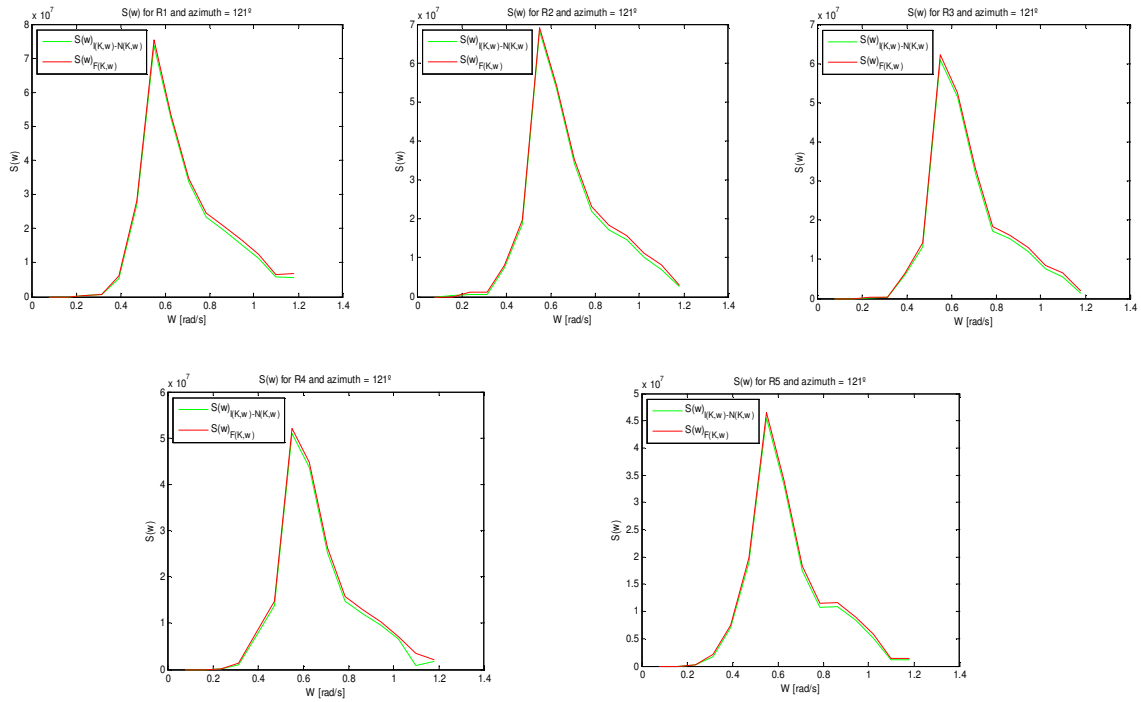
Figure 6.5: Evolution of the $S(\omega)$ of the dispersion relation (in red colour) and the $S(\omega)$ of
the subtraction of the original marine radar spectrum and the interpolated spectrum (in green
colour) according to the range for a prearranged azimuth equal to 121º.
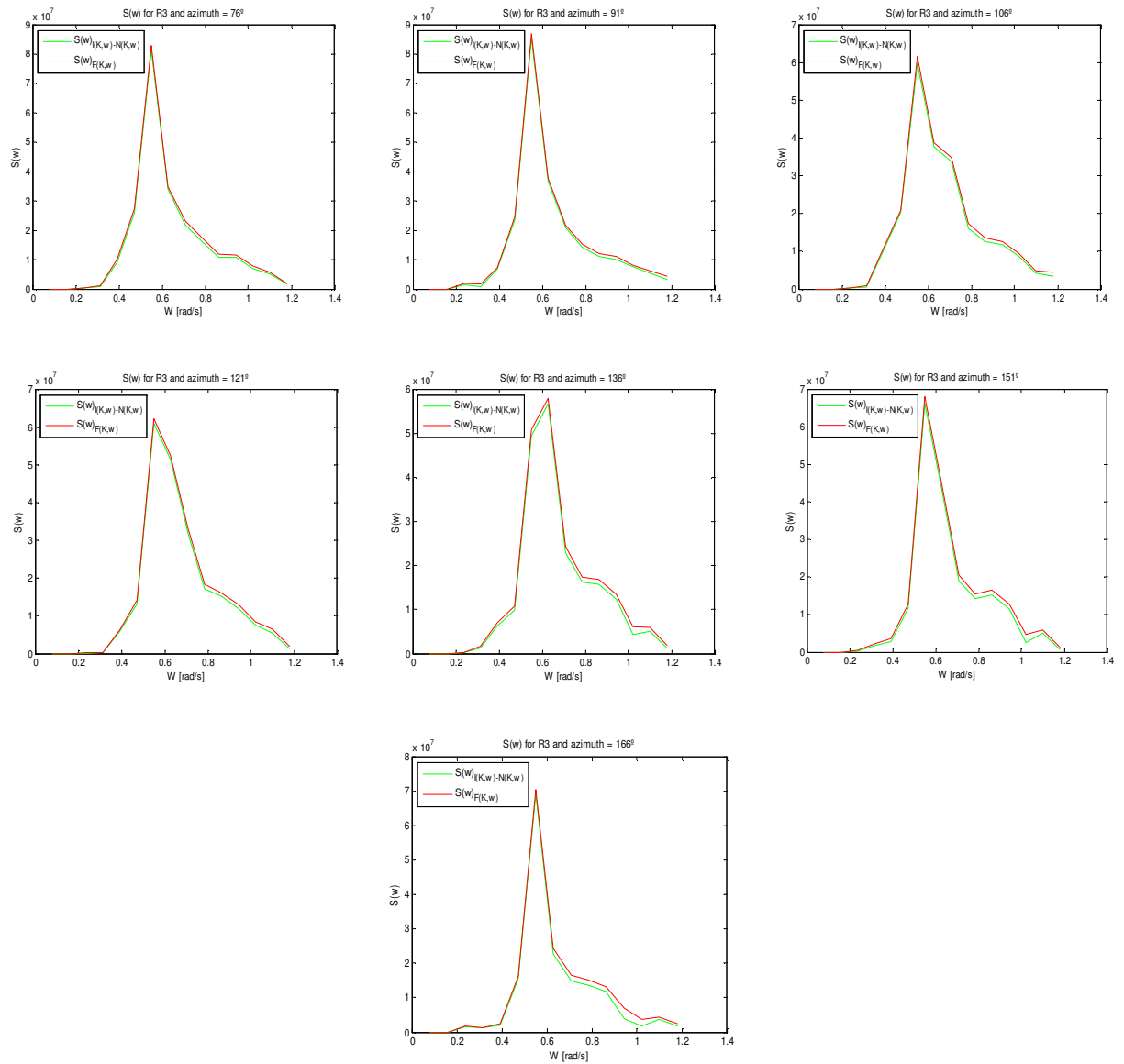
Figure 6.6: Evolution of the $S(\omega)$ of the dispersion relation (in red colour) and the $S(\omega)$ of the subtraction of the original marine radar spectrum minus the interpolated spectrum (in green colour) according to the azimuths between 76º and 166º for the $R3$ range fixed.
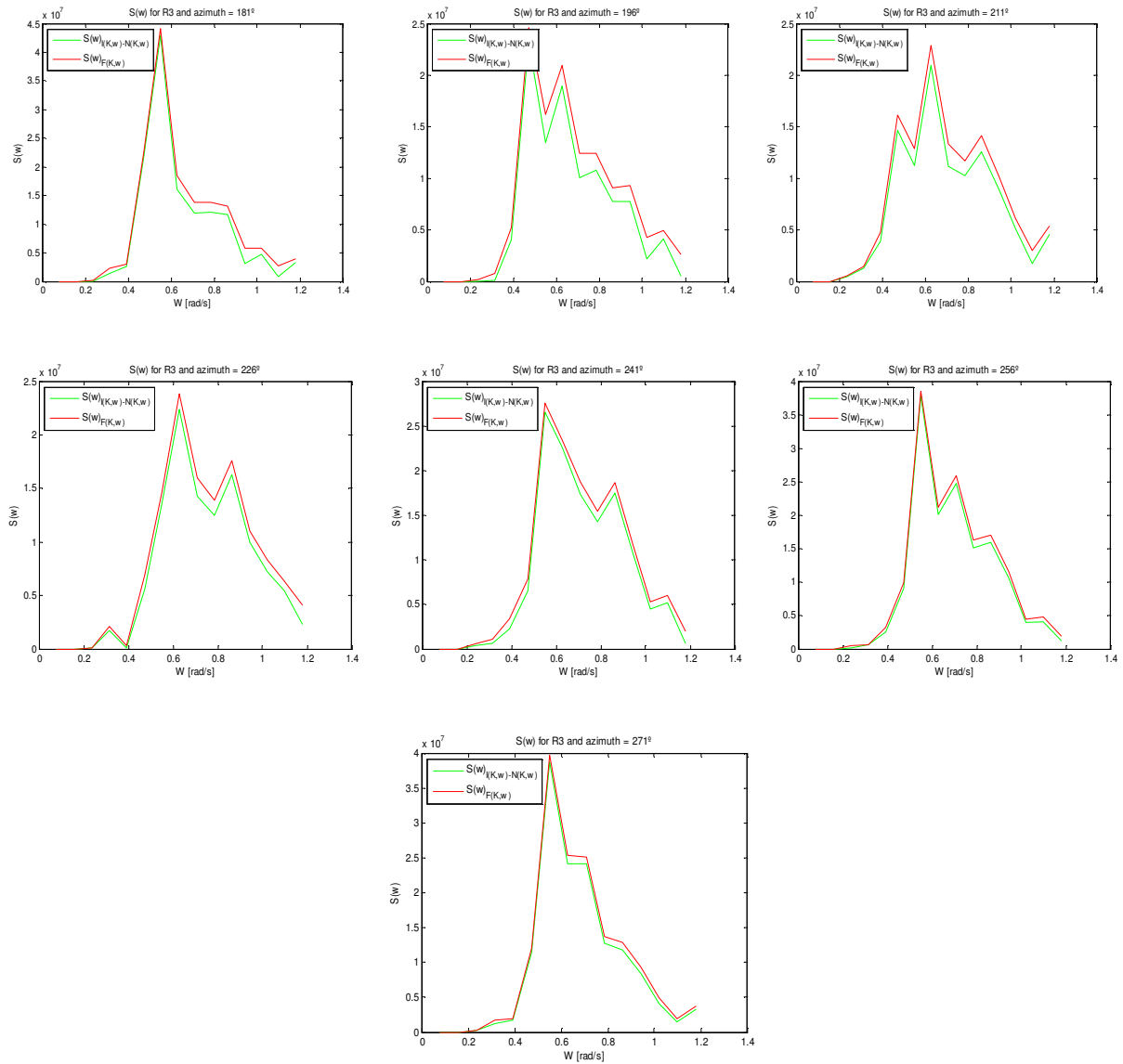
Figure 6.7: Evolution of the $S(\omega)$ of the dispersion relation (in red colour) and the $S(\omega)$ of the subtraction of the original marine radar spectrum minus the interpolated spectrum (in green colour) according to the azimuths between 181º and 271º for the $R3$ range fixed.

Chapter 7

Analysis of Hörnum Dataset

7.1   Introduction to the study developed

The radar data provided by the Hörnum station are characteristic because of only 180° of the circumference contains information. The another part is blanked and it is not possible to get information. According to this fact, the range and azimuth studies, which were evolved for FINO 1 radar data performed before, cannot be applied. In this case, the acceptable part is divided in three windows avoiding the small blanked areas that can be seen in figure 3.8 on the left and on the right of the radar.
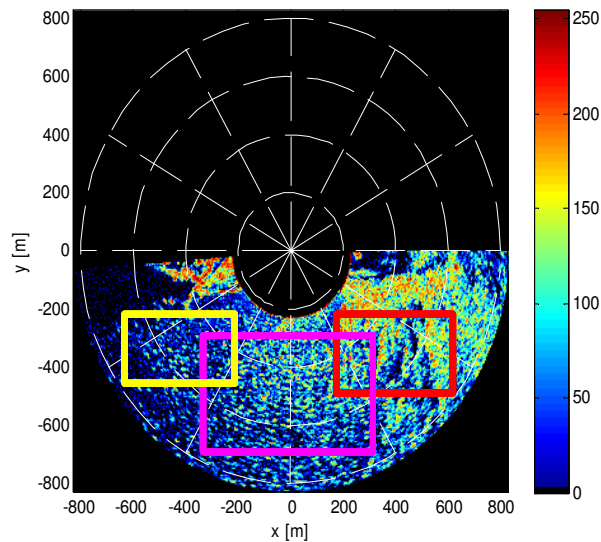
Figure 7.1: Radar image provided by Hörnum station and the three windows to analyse.

These three windows have different sizes according to cover the maximum sea surface area. The figure 7.1 represents the windows under study. The size of the red window is 889.2 m × 538.2 m. The size of the area for the pink one is 1287 m × 795.6 m. And for the yellow window, the size is 833 m × 468 m.

The range cover by the radar is smaller than FINO 1. In Hörnum data, the total distance covered is 1645 m, being the resolution of range equal to 4.68 m, therefore the radius of range of the radar is 822.5 m.

The main inconvenient found in these data sets is that the significant wave height is low, and these marine radar imagery have not got a distinguishable the front of waves. The data set selected to present this chapter is the file corresponding to the 20th of January 2006, at the time 11 p.m. In the figure 7.2 the sea surface for this set of data is represented. It is not very clear to sea the front of the waves. The main characteristics provided by the sensors are:

- Mean wave direction ($MDIR$): 254º

- Significant wave height (H_s): 1.3 m

- X component of the current (U_x): -0.52 m s^{-1}

- Y component of the current (U_y): -1.42 m s^{-1}

- Modulus of the current (U): 1.51 m s^{-1}

- Peak period (T_p): 5.5 s

- Mean period (T_{m02}): 5.5 s
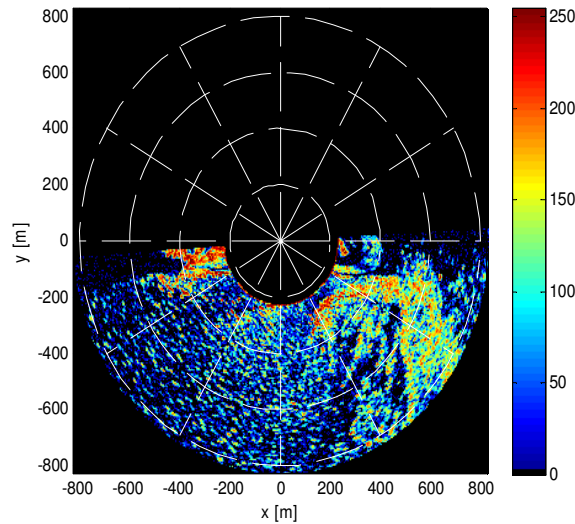
Figure 7.2: Image of one of the instants of the time series of the X-band marine radar for Hörnum data set.

The whole radar images sequences are evaluated and the process followed to manage it is:

- The WaMoS II system provides the radar images in Polar coordinates, therefore the first step is transforming the Polar coordinates to Cartesian.

- The three windows under study are taken.

- The Fast Fourier Transform is applied in the 32 images, which compose a data set.

- The dispersion shell, the first harmonic and the group line are extracted.

- The interpolation is carried out in the parts that have been removed, such as the dispersion shell, the first harmonic and the group line, as it is discussed before in section 4.3.

- The Inverse Fast Fourier Transform is done to obtain the resulting radar images.

- The Signal to Noise Ratio calculation is done considering different factors, how is presented in detail in the chapter 6.

For these three windows, the dispersion relation, the group line and the *SNR* are studied. Besides the main characteristics under study in each window will be:

- The mean intensity of the radar signal.

- The mean intensity contained in the 3D spectrum of the dispersion shell.

- The mean intensity contained in the 3D spectrum of the group line.

- The mean of the 3D spectrum.

- The mean of the 2D spectrum.

- Signal to Noise Ratio for both filters.

7.2 Study of the dispersion shell

The first step is to extract the dispersion shell for the three windows (the red, the pink and the yellow one).

The results obtained are collected in the following table 7.1, where the characteristics under study are the same than the chapter 4:

- I_{signal}: The mean intensity of the radar signal.

- $I_{\text{dispersion}}$: The mean intensity contained in the 3D spectrum of the dispersion shell.

- I_{3D}: The mean of the 3D spectrum.

- I_{2D}: The mean of the 2D spectrum.

Table 7.1: Results regarding the dispersion relation for the three windows for Hörnum data set.

Windows	I_{signal} [dB]	I_{3D} [dB]	I_{2D} [dB]	$I_{\text{dispersion}}$ [dB]
Red window	18.91	-24.10	-2.96	29.33
Pink window	16.46	-23.41	-21.41	24.48
Yellow window	14.86	-29.85	-33.06	27.48

Table 7.1 shows that the mean intensity contained in the 3D spectrum of the dispersion relation and the mean intensity of the radar signal correspond to the red window are the highest values. For yellow window, the biggest one, the mean intensity contained in the 2D and 3D spectra of the dispersion shell is the lowest.

In the figures 7.3, 7.4 and 7.5 the three-dimensional pass-band filter and the spectra of each window are described. In all of the spectra it is impossible to distinguish the dispersion shell or the group line. Even the three-dimensional pass-band filters have not a typical shape showed before. The filter is represented by 4 colours according to the phenomenon displayed, being the orange colour which represents the dispersion relation, in green colour the aliased of the dispersion relation, in light blue the first harmonic and in dark blue the aliased first harmonic.
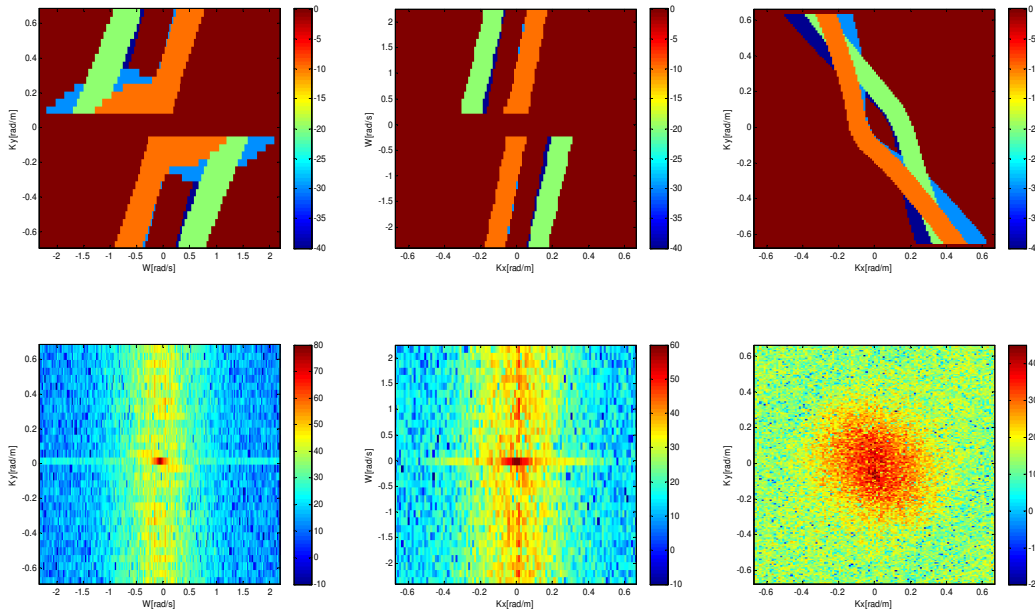
Figure 7.3: Pictures on the top represent the three-dimensional pass-band filter for the red window. The pictures on the bottom represent the spectra for red window before being filtering for the same transects than the first row. The first subplot in the first row depicts a transect in the 3D-spectrum for $k_x = 0$ rad m^{-1} axis, the second subplot in the first row represents a transect in the 3D-spectrum for $k_y = 0$ rad m^{-1} axis and the third subplot in the first row depicts a transect for ω.
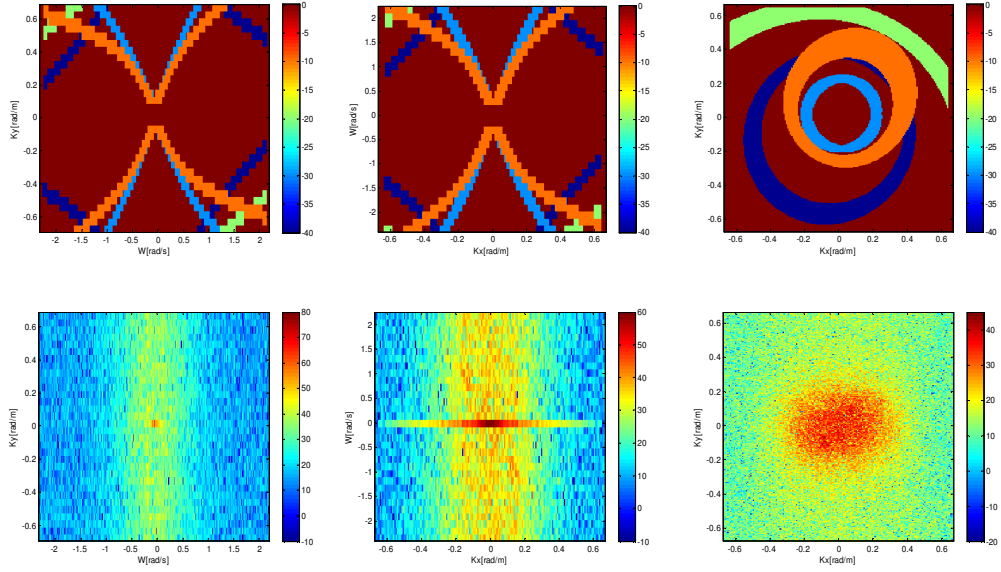
Figure 7.4: Pictures on the top represent the three-dimensional pass-band filter for the pink window. The pictures on the bottom represent the spectra for pink window before being filtering for the same transects than the first row. The first subplot in the first row depicts a transect in the 3D-spectrum for $k_x = 0$ rad m^{-1} axis, the second subplot in the first row represents a transect in the 3D-spectrum for $k_y = 0$ rad m^{-1} axis and the third subplot in the first row depicts a transect for ω.

In the figure 7.6 the three dispersion relations extracted by the adaptive filter are represented. The first corresponds to the red window, the second to the pink window and the third to the yellow window. All of them are well defined, however they can be seen in the spectra.

7.3   Study of the group line

The table 7.2 collects the values of the mean intensity contained in the 3D spectrum of the the group line for the three windows. In this case the group line is maximum in the red window and minimum in the yellow window.

Table 7.2: The mean intensity contained in the 3D spectrum of the group line.

	Red window	Pink window	Yellow window
I_{GL} [dB]	38.72	33.87	30.46

The values of the mean intensity contained in the 3D spectrum of the group line are greater than the values of the mean intensity contained in the 3D spectrum for the dispersion shell.
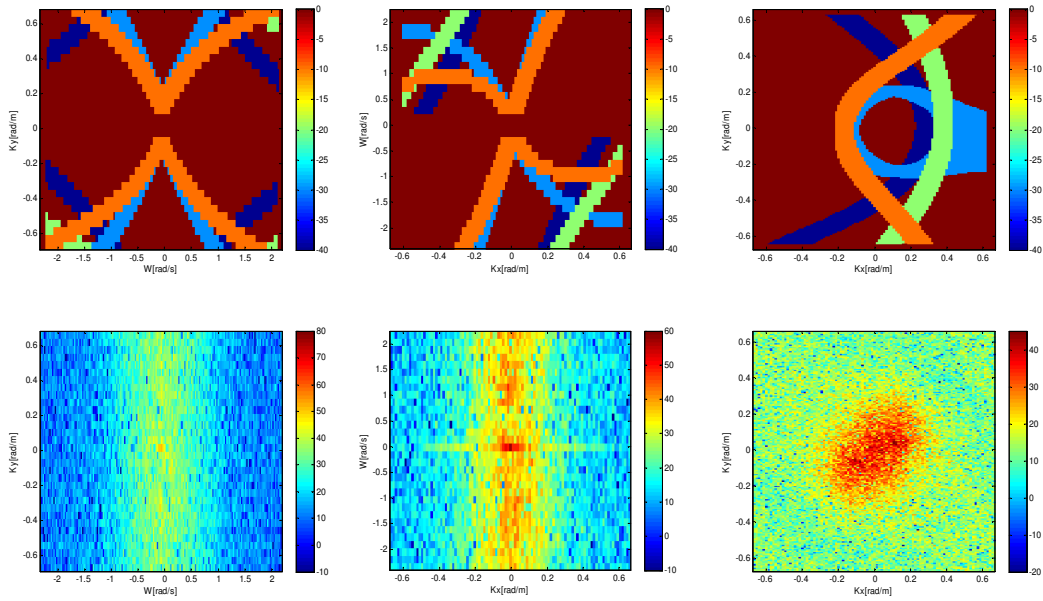
Figure 7.5: Pictures on the top represent the three-dimensional pass-band filter for the yellow window. The pictures on the bottom represent the spectra for yellow window before being filtering for the same transects than the first row. The first subplot in the first row depicts a transect in the 3D-spectrum for $k_x = 0$ rad m^{-1} axis, the second subplot in the first row represents a transect in the 3D-spectrum for $k_y = 0$ rad m^{-1} axis and the third subplot in the first row depicts a transect for ω.

How it was commented above, in the figures 7.3, 7.4 and 7.5 it is not possible to see the group line. However the extraction of the group lines for each window are shown in the figure 7.7. The first image represents the group line for the red window, the second for the pink one and the third picture shows the group line for the yellow window.

7.4 Study of the Signal to Noise Ratio

In chapter 6 different kind of SNR was presented and here is going to follow the same procedure. Therefore, the SNRs under study are:

- SNR_{12}: Signal due to the dispersion shell and without group line filtered by the three-dimensional pass-band filter without MTF and Noise considering the group line but not considering the interpolation.

- SNR_{22}: Signal due to the dispersion shell and without group line filtered by the three-dimensional pass-band filter with MTF and Noise considering the group line but not considering the interpolation.
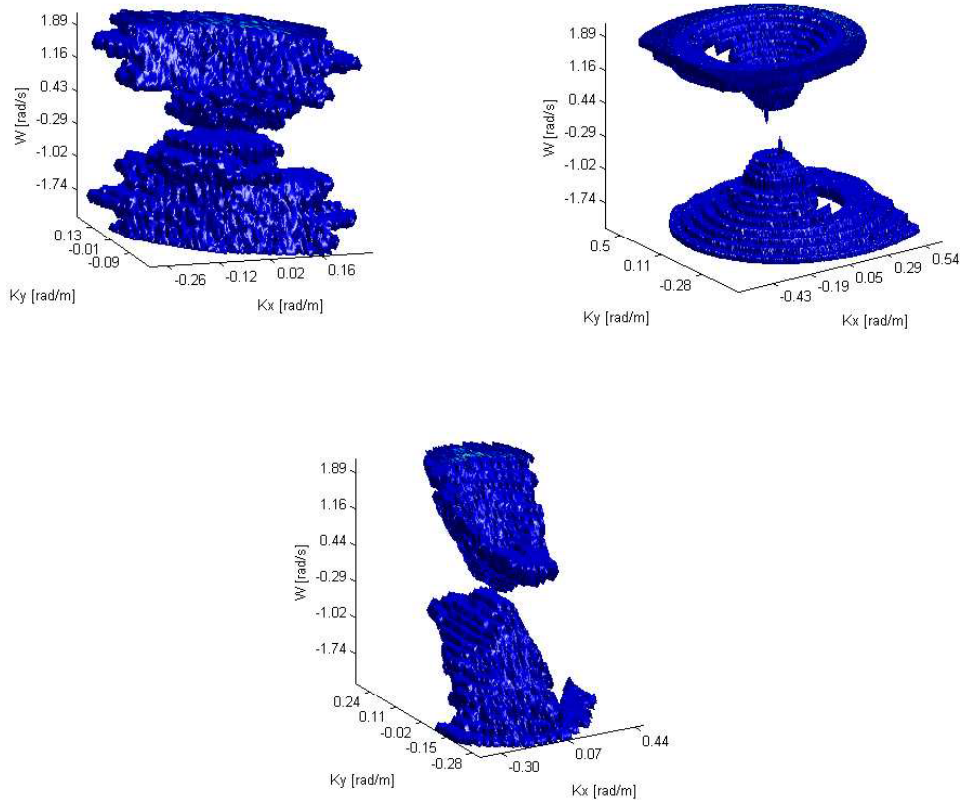
Figure 7.6: Dispersion relation for red, pink and yellow-labeled windows.

- SNR_{32}: Signal due to the dispersion shell and without group line filtered by the adaptive filter without MTF and Noise considering the group line but not considering the interpolation.

- SNR_{42}: Signal due to the dispersion shell and without group line filtered by the adaptive filter with MTF and Noise considering the group line but not considering the interpolation.

- SNR_{14}: Signal due to the dispersion shell and without group line filtered by the three-dimensional pass-band filter without MTF and Noise considering the group line and the interpolation.

- SNR_{24}: Signal due to the dispersion shell and without group line filtered by the three-dimensional pass-band filter with MTF and Noise considering the group line and the interpolation.

- SNR_{34}: Signal due to the dispersion shell and without group line filtered by the adaptive filter without MTF and Noise considering the group line and the interpolation.

- SNR_{44}: Signal due to the dispersion shell and without group line filtered by the adaptive

Figure 7.7: Group line for red, pink and yellow-labeled windows.

filter with MTF and Noise considering the group line and the interpolation.

- SNR_{51}: Signal due to the dispersion shell and group line filtered by the three-dimensional pass-band filter without MTF and Noise without considering the group line neither the interpolation.

- SNR_{61}: Signal due to the dispersion shell and group line filtered by the three-dimensional pass-band filter with MTF and Noise without considering the group line neither the interpolation.

- SNR_{71}: Signal due to the dispersion shell and group line filtered by the adaptive filter without MTF and Noise without considering the group line neither the interpolation.

- SNR_{81}: Signal due to the dispersion shell and group line filtered by the adaptive filter with MTF and Noise without considering the group line neither the interpolation.

- SNR_{53}: Signal due to the dispersion shell and group line filtered by the three-dimensional pass-band filter without MTF and Noise without considering the group line but the interpolation is considered.

- SNR_{63}: Signal due to the dispersion shell and group line filtered by the three-dimensional pass-band filter with MTF and Noise without considering the group line but the interpolation is considered.

- SNR_{73}: Signal due to the dispersion shell and group line filtered by the adaptive filter without MTF and Noise without considering the group line but the interpolation is considered.

- SNR_{83}: Signal due to the dispersion shell and group line filtered by the adaptive filter with MTF and Noise without considering the group line but the interpolation is considered.

In the tables 7.3 and 7.4 the values of the SNR are collected, but they are separated according if the group line belongs to Signal or Noise. The values of SNR related to the adaptive filter are written in bold letters.

Table 7.3: Signals that not consider the group line as a part of a signal and Noises that consider the group line as a part of a noise.

SNR [dB]	Red window	Pink window	Yellow window
SNR_{12}	0.12	0.17	0.19
SNR_{22}	1.91	2.13	2.96
$\mathbf{SNR_{32}}$	**0.49**	**0.15**	**0.38**
$\mathbf{SNR_{42}}$	**15.72**	**1.82**	**7.63**
SNR_{14}	0.11	0.16	0.18
SNR_{24}	1.81	2.21	2.82
$\mathbf{SNR_{34}}$	**0.42**	**0.15**	**0.37**
$\mathbf{SNR_{44}}$	**13.28**	**1.85**	**7.37**

Table 7.4: Signals that consider the group line as a part of a signal and Noises that not consider the group line as a part of a noise.

SNR [dB]	Red window	Pink window	Yellow window
SNR_{51}	0.18	0.27	0.24
SNR_{61}	3.89	4.15	4.49
$\mathbf{SNR_{71}}$	**0.62**	**0.25**	**0.44**
$\mathbf{SNR_{81}}$	**19.74**	**3.77**	**9.82**
SNR_{53}	0.17	0.25	0.22
SNR_{63}	3.56	3.89	4.17
$\mathbf{SNR_{73}}$	**0.49**	**0.24**	**0.41**
$\mathbf{SNR_{83}}$	**15.64**	**3.65**	**9.20**

The SNR values got by the adaptive filter for the red and yellow window are higher than those obtained by the three-dimensional pass-band filter. However, only for pink window, values got by the adaptive filter are lower than those obtained by the three-dimensional pass-band

filter. Another observation is that applying the modulation transfer function, the value is always greater. The main disadvantage observed here is that the table 7.3 is not equal to 7.4. In this case, the *SNR* not depends only on the dispersion relation, the group line must be taken into account.

The frequency wave spectrum $S(\omega)$ is represented in 7.8. The figure shows if the dispersion shell that have been extracted is very similar to the subtraction between the original marine radar spectrum and the spectrum where the dispersion relation has been extracted and interpolated. The first picture is the $S(\omega)$ for red window, the second corresponds to the pink window and the third is the $S(\omega)$ for the yellow window. But in all of them, the adjustment is not very good, there are big differences between the two curves.
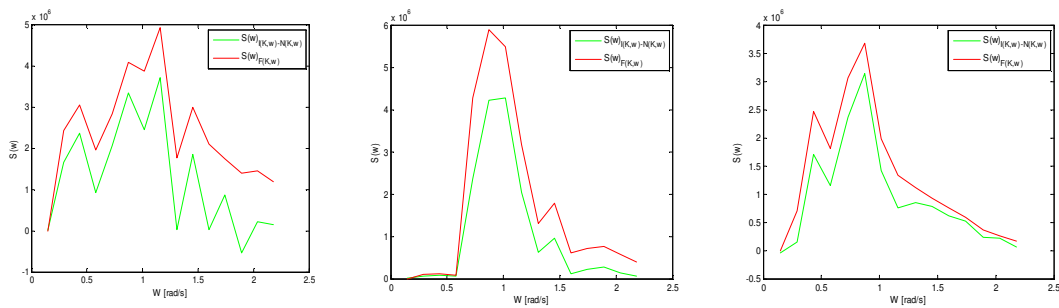
Figure 7.8: Evolution of the $S(\omega)$ of the dispersion relation (in red colour) and the $S(\omega)$ of the subtraction of the original marine radar spectrum minus the interpolated spectrum (in green colour) for the red, pink and yellow-labeled windows respectively.

Chapter 8

Simulation of Wave Fields and Associated X-Band Radar Images

The structure of the phenomena involved in the formation of the radar images of the sea surface and their related image spectra is still under investigation. There are different mechanism responsible of the radar imagery that are not well-understood yet. A possible way of analysis is to investigate all the physical phenomena involved in the backscattering due to the sea surface roughness using a full electromagnetic approach [13, 14]. This approach requires to model some physical effects, such as wave breaking and sea surface foam formation, that are responsible of strong back scatter, which are not well understood either. In addition, the full electromagnetic approach required the use of solving numerical models that need supercomputation facilities [14]. All of that means that the full electromagnetic approach is not fully feasible yet. A different approach is using stochastic approach that takes into account some of the most relevant physical phenomenon involved in the formation of the sea clutter. This approach permits to simulate radar images for given meteorological conditions. Thus, the use a simulation tool capable of provide reliable simulations of sea clutter images is useful for two different applications:

- Analysis of effects of different sea surface properties (e.g. wave spectral shape, wind conditions, etc.) and theirs effects on the sea clutter images (e.g. shadowing, tilt modulation, etc.) [34].

- Derivation of those sea surface properties from the simulated sea clutter image developing inverse modelling techniques [11].

- Obtaining of more realistic synthetic sea clutter images for developing of filter involved in radar applications, such as robust target detection in presence of strong clutter conditions. Hence, a simulation model based on the most relevant physical phenomena responsible on the backscatter is a most useful tool than the simplistic approach use on some of the radar filters that consider that the sea clutter is just a K-distributed random process [35, 36] (i.e. not important effects, such shadowing or tilt modulation are not considered in the K-distribution models).

This chapter deals with the application of a simulation scheme based on the stochastic description of ocean waves and their associate radar images (see chapters 2 and 3) to extract information about the structure of the image spectrum in the $(\mathbf{k}, \omega)$-domain.

8.1   Simulation of sea surface elevation fields

Under the frame of the linear wave theory described in chapter 2, and assuming an Eulerian description of the free sea surface [31] given the stochastic model (2.5), the wave elevation η for each sea surface position $\mathbf{r} = (x, y)$ at time t can be expressed as [37]

$$\eta(\mathbf{r}, t) = \sum_{\mathbf{k}} a_{\mathbf{k}} \cos\left(\mathbf{k} \cdot \mathbf{r} - \omega(\mathbf{k})t + \varphi_{\mathbf{k}}\right) \tag{8.1}$$

where $\mathbf{k} = (k_x, k_y)$ is the wave number vector, ω the angular frequency, which is related to $\mathbf{k}$ through the dispersion relation of linear gravity waves [3], and $a_{\mathbf{k}}$ and $\varphi_{\mathbf{k}}$ the respective amplitudes and phases of each wave component identified by the wave number $\mathbf{k}$. For practical purposes, equation (8.1) is computed by using a two-dimensional Fast Fourier Transform (FFT)-based algorithm [37]. In that case, the sea surface coordinates $\mathbf{r} = (x, y)$ are spatially sampled, with spatial resolutions $(\Delta x, \Delta y)$. In the same way, the wave number vectors $\mathbf{k} = (k_x, k_y)$ are as well sampled with the resolutions $(\Delta k_x, \Delta k_y)$ given by the Discrete Fourier Transform (DFT) theory. In that case, it is convenient to rewrite the expression (8.1) in the following way

$$\eta(\mathbf{r}, t) = \mathsf{Re}\left[\sum_{k_x}\sum_{k_y} c_{\mathbf{k}}(t)\, e^{j\mathbf{k}\cdot\mathbf{r}}\right] \tag{8.2}$$

where the complex coefficients $c_{\mathbf{k}}(t)$ are the input of a two-dimensional FFT algorithm for a given time t, i.e.

$$c_{\mathbf{k}}(t) \equiv a_{\mathbf{k}}\, e^{j(-\omega(\mathbf{k})t + \varphi_{\mathbf{k}})}. \tag{8.3}$$

Note that, for a given time t, the coefficients $c_{\mathbf{k}}(t)$ are distributed in a complex matrix depending on the sampling values, $(\Delta k_x, \Delta k_y)$, of the wave number vector $\mathbf{k} = (k_x, k_y)$.

As it was mentioned in the above chapter 2, those wave fields described by equation (8.1) are usually considered as stochastic processes [4], the random variables that lead the stochastic properties of η in the expression (8.1) are $\varphi_{\mathbf{k}}$ and $a_{\mathbf{k}}$. Assuming that the wave elevation field η is a zero-mean Gaussian-distributed variable, the phases $\varphi_{\mathbf{k}}$ are usually considered as uniformly distributed random variables in the interval $[-\pi, \pi)$, and the amplitudes $a_{\mathbf{k}}$ follow a Rayleigh distribution. The amplitudes $a_{\mathbf{k}}$ are derived from the so-called wave number spectrum $F(\mathbf{k})$ as [37]

$$a_{\mathbf{k}} = \sqrt{F^{(2)}(\mathbf{k})\Delta k_x \Delta k_y / 2} \cdot \left(\alpha_{\mathbf{k}}^2 + \beta_{\mathbf{k}}^2\right)^{1/2} \tag{8.4}$$

where $\alpha_{\mathbf{k}}$ and $\beta_{\mathbf{k}}$ are two uncorrelated zero-mean and unit-variance Gaussian variables. Hence, $a_{\mathbf{k}}$ is a Rayleigh-distributed random variable. The division by 2 inside the root squared in equation (8.4) is necessary to keep the variance of the process η and it is due to the fact of taking only the real part of at the end of the FFT algorithm. The spectrum $F^{(2)}(\mathbf{k})$ depends on the meteorological conditions responsible of the wave field generation [3]. To express the function $F^{(2)}(\mathbf{k})$ in terms of the theoretical parameterizations that lead the spectral properties from a given meteorological situation, $F^{(2)}(\mathbf{k})$ is factorized as [23]

$$F^{(2)}(\mathbf{k}) = S(\omega)D(\omega,\theta)\frac{1}{k}\frac{\mathrm{d}\omega}{\mathrm{d}k} \ , \tag{8.5}$$

where $S(\omega)$ is the frequency wave spectrum, which gives information of the wave energy distribution for each wave frequency ω, and $D(\omega,\theta)$ is known as the directional spreading function, which represents the wave propagation direction probability density function for each wave frequency ω (see chapter 2), being $\theta = \tan^{-1}(k_y/k_x)$ the wave propagation direction. The term $1/k \cdot \mathrm{d}\omega/\mathrm{d}k$ are the needed Jacobians to change from the (ω,θ) to the (k_x, k_y) spaces [23]. For that purpose, equation (8.5) takes into account the fact that ocean waves are dispersive, and the dispersion relation (2.3) for ocean waves

$$\omega = \sqrt{gk\tanh(kd)} + \mathbf{U} \cdot \mathbf{k}. \tag{8.6}$$

In presence of a current $\mathbf{U} = (U_x, U_y)$, the expression (8.6) has to be rewritten for a properly derivation of the group velocity $v_g = \mathrm{d}\omega/\mathrm{d}k$ that appears in equation (8.5). Hence, for a given wave direction θ and considering a fixed current direction $\theta_{\mathbf{U}} = \tan^{-1}(U_y/U_x)$, the expression (8.6) can be rewritten as

$$\omega = \sqrt{gk\tanh(kd)} + Uk\cos(\theta - \theta_{\mathbf{U}}) \tag{8.7}$$

where $U = |\mathbf{U}|$. Therefore, for a given wave direction θ, the group velocity v_g is

$$v_g(k,\theta) = \frac{\mathrm{d}\omega}{\mathrm{d}k} = g\frac{\tanh(kd) + kd/\cosh^2(kd)}{2\sqrt{gk\tanh(kd)}} + U\cos(\theta - \theta_{\mathbf{U}}). \tag{8.8}$$

To estimate $S(\omega)$ in equation (8.5), JONSWAP spectra [38] can be considered for wind sea conditions, and a Wallops spectra [39] for swell cases. For the directional spreading function $D(\omega,\theta)$ the parameterization proposed by Mitsuyasu et al. [40] has been taken into account. Figure 8.1 shows an example of simulated wave field using the stochastic description of sea states given by equation (8.1).
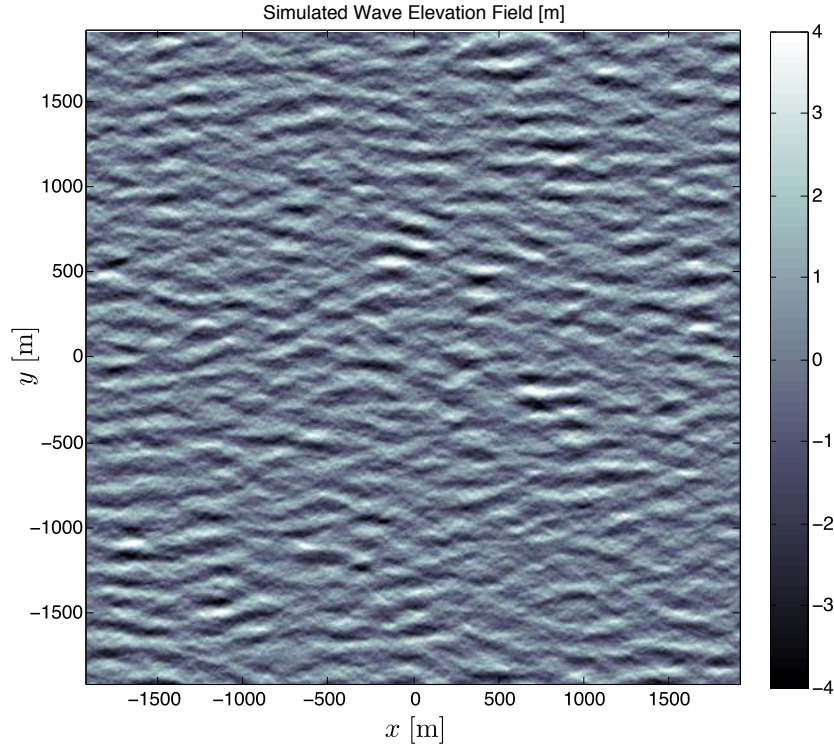
Figure 8.1: Simulated wave elevation field derived from a JONSWAP spectrum with $f_p = 0.12$ Hz and $H_s = 4$ m.

8.2   Simulation of X-band marine radar images

Once the sea surface elevation due to the wave field $\eta(\mathbf{r}, t)$ is derived by using equation (8.1), the next step is to simulate the corresponding marine radar images. For that purpose the different known mechanisms responsible of the backscatter phenomenon of the electromagnetic fields transmitted by the radar antenna have to be taken into account. The simulation method of marine radar images associated to a given wave field proposed in this work considers the basic form of the radar equation given by expression (3.9) [41], where the ratio between the transmitted power P_t and the received power P_r is given by

$$\frac{P_r}{P_t} = \frac{G\, A_{\text{eff}}\, \sigma}{(4\pi)^2 R^4} \tag{8.9}$$

The radar cross section (RCS) is represented by σ and it is factorised as $\sigma = \sigma_0 A_t$, where A_t is the area of the target and σ_0 is the so-called Normalized Radar Cross Section (NRCS). In this context, the target is the facet of the sea surface illuminated by the radar. The facet size depends on the azimuthal $\Delta\phi$ and range ΔR radar resolutions. The simulation method of radar images assumes the characteristics and operation conditions of a conventional marine radars [41], i.e. X-band, grazing incidence conditions, HH-polarized, logarithmic amplifier, and incoherent system with no frequency agility.

8.2.1 Steps of the sea clutter simulation for marine radar conditions

The method to simulate the sea clutter from a given sea surface, considers the position of the radar antenna (i.e. (x, y, z) coordinates, where $z = 0$ indicates the mean sea level), as well as the azimuthal $\Delta\phi$ and range ΔR resolutions. Hence, for a flat sea surface, and considering a rectangular radar pulse, the target area A_t of a radar beam at range R is $A_t \approx R\Delta R\Delta\phi$. Figure 8.2 illustrates the radar imaging geometry used for the simulation of sea clutter images. The basic steps to compute the radar image estimations can be summarised as
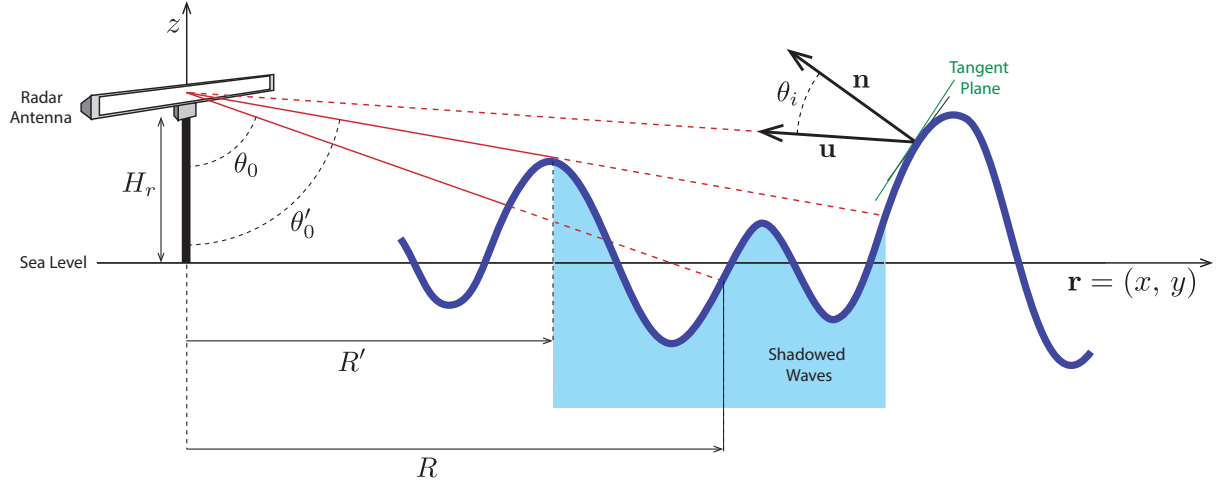
Figure 8.2: Two-dimensional scheme of the radar imaging geometry used for the sea clutter image simulation.

1. Shadowing modulation: This effect appears when high waves hide lower waves to the radar antenna. The shadowing modulation considers a geometric optics approach, which can be assumed valid as a first order approach of the backscattering phenomenon for HH-polarization and grazing incidence conditions at far ranges [11], which is the typical operational situation of a marine radar. Hence, this geometrical approach does not take into account higher order backscattering mechanisms, such as the diffraction of the electromagnetic fields behind the wave crests that are easily measured by other kind of more sensitive radar systems [42].

   At grazing incidence, the X-band radar imagery mechanisms induce a strong modulation in the radar images. The example shown in the previous figure 3.2 illustrates the shadowing effect as black areas of the radar intensity image behind the radar imaged wave fronts. Under these assumptions, for marine radar operational conditions, the local incidence angle on an illuminated facet of the sea surface at position $\mathbf{r} = (x, y)$ at time t is given by the radar range $R(\mathbf{r})$, the wave elevation $\eta(\mathbf{r}, t)$, and the radar antenna height over the sea level H_r as (see Figure 8.2)

$$\theta_0(\mathbf{r}, t) = \tan^{-1}\left[\frac{R(\mathbf{r})}{H_r - \eta(\mathbf{r}, t)}\right]. \tag{8.10}$$

At the instant t, the facet at point $\mathbf{r}$ will be shadowed to the antenna if there is another facet located at point $\mathbf{r}'$, with range $R' = R(\mathbf{r}') < R(\mathbf{r})$, with the same azimuthal angle ϕ than the point $\mathbf{r}$ (e.g. $\phi(\mathbf{r}') = \phi(\mathbf{r})$), that has an incidence angle $\theta_0' = \theta_0(\mathbf{r}', t) \geq \theta_0(\mathbf{r}, t)$. Hence, the illumination mask $m(\mathbf{r}, t)$ is constructed as

$$m(\mathbf{r}, t) = \begin{cases} 1, & \text{if no shadowing occurs} \\ 0, & \text{otherwise.} \end{cases} \tag{8.11}$$

The illumination mask $m(\mathbf{r}, t)$ contains information about the spatio-temporal evolution of the shadowing mechanism. Figure 8.3 shows an example of illumination mask m obtained from the simulated wave field shown in figure 8.1 for a value $H_r = 30$ m.
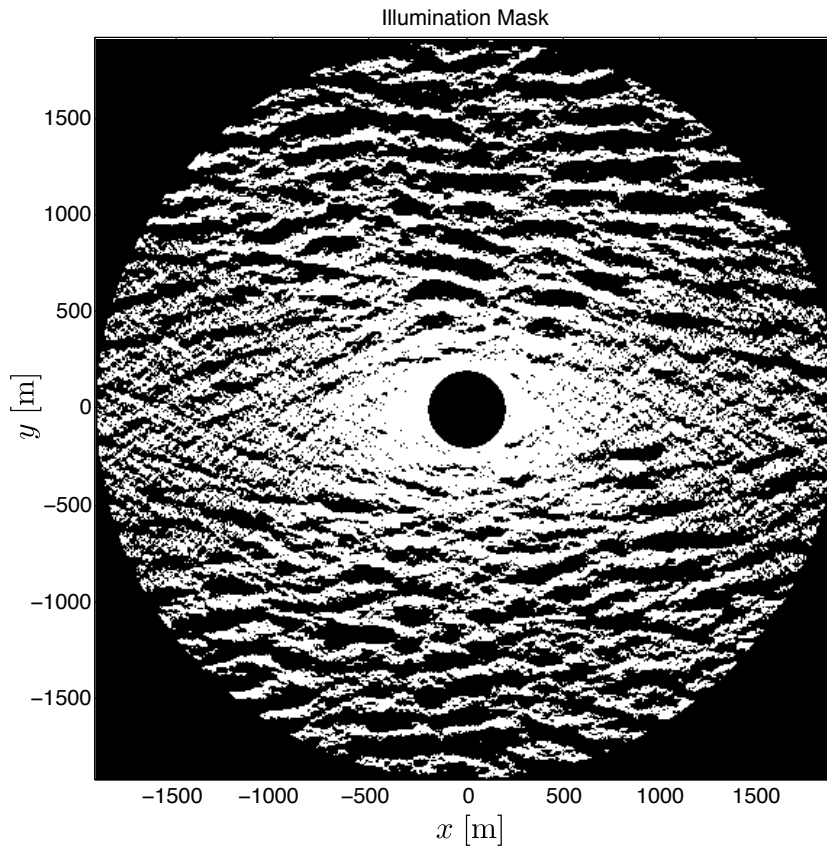
Figure 8.3: Illumination mask of the simulated wave field shown in figure 8.1. The illuminated areas are coded in white. The black areas are shadowed. The radar is located in the center of the image. The inner circle in black corresponds to the range where a typical marine radar presents saturation of the backscatter signal.

2. Tilt modulation: This effect depends on the orientation of the radar illuminated facet of the sea surface to the antenna [11]. Knowing the sea surface $\eta(\mathbf{r}, t)$, the tilt modulation can be evaluated by using the dot product between the three-dimensional unit exterior normal vector $\mathbf{n}(\mathbf{r}, t)$ to the simulated sea surface $\eta(\mathbf{r}, t)$, and the three-dimensional unit vector

from the facet to the radar antenna, $\mathbf{u}(\mathbf{r}, t)$ (see figure 8.2). For a given time t, the unit exterior normal vector to the sea surface $\mathbf{n}(\mathbf{r}, t)$ is constructed assuming that $z = \eta(x, y, t)$ is a differentiable surface in $\mathbb{R}^3$, which is a valid assumption for a spatial scale equal or larger than the facet size. Hence, the wave elevation surface can be described analytically by the following parameterized vector field $\boldsymbol{\eta}(\mathbf{r}, t) \in \mathbb{R}^3$

$$\boldsymbol{\eta}(\mathbf{r}, t) = \begin{pmatrix} x \\ y \\ \eta(\mathbf{r}, t) \end{pmatrix} \tag{8.12}$$

From equation (8.12), the three-dimensional tangent vector fields to the surface $\boldsymbol{\eta}(\mathbf{r}, t)$ along the x and y coordinates are respectively [43]

$$\boldsymbol{\tau}_x(\mathbf{r}, t) = \frac{\partial}{\partial x} \boldsymbol{\eta}(\mathbf{r}, t) = \begin{pmatrix} 1 \\ 0 \\ \partial \eta(\mathbf{r}, t)/\partial x \end{pmatrix} \tag{8.13}$$

and

$$\boldsymbol{\tau}_y(\mathbf{r}, t) = \frac{\partial}{\partial y} \boldsymbol{\eta}(\mathbf{r}, t) = \begin{pmatrix} 0 \\ 1 \\ \partial \eta(\mathbf{r}, t)/\partial y \end{pmatrix} \tag{8.14}$$

Assuming the expression (8.2), the spatial derivatives of $\eta(\mathbf{r}, t)$ used in equations (8.13) and (8.14) are given by

$$\frac{\partial \eta(\mathbf{r}, t)}{\partial x} = \mathsf{Re} \left[\sum_{k_x} \sum_{k_y} \mathrm{j} k_x \, c_{\mathbf{k}}(t) \, e^{\mathrm{j}\mathbf{k}\cdot\mathbf{r}} \right] \tag{8.15}$$

and

$$\frac{\partial \eta(\mathbf{r}, t)}{\partial y} = \mathsf{Re} \left[\sum_{k_x} \sum_{k_y} \mathrm{j} k_y \, c_{\mathbf{k}}(t) \, e^{\mathrm{j}\mathbf{k}\cdot\mathbf{r}} \right] \tag{8.16}$$

Hence, $\mathrm{j} k_x \, c_{\mathbf{k}}(t)$ and $\mathrm{j} k_y \, c_{\mathbf{k}}(t)$ are the input for the two-dimensional FFT algorithms to compute $\partial \eta/\partial x$ and $\partial \eta/\partial y$ respectively. Taking into account the expresssions (8.13) and (8.14), the vector field $\mathbf{n}(\mathbf{r}, t)$ is given by

$$\mathbf{n}(\mathbf{r}, t) = \frac{\boldsymbol{\tau}_x(\mathbf{r}, t) \times \boldsymbol{\tau}_y(\mathbf{r}, t)}{|\boldsymbol{\tau}_x(\mathbf{r}, t) \times \boldsymbol{\tau}_y(\mathbf{r}, t)|} = \frac{-\nabla \eta(\mathbf{r}, t) + \mathbf{e}_z}{\sqrt{|\nabla \eta(\mathbf{r}, t)|^2 + 1}} \tag{8.17}$$

where $\times$ denotes the vector product, and $\nabla = \partial/\partial x \, \mathbf{e}_x + \partial/\partial y \, \mathbf{e}_y$ is the two-dimensional gradient operator, being $\mathbf{e}_x$, $\mathbf{e}_y$, $\mathbf{e}_z$ the triad of unit vectors along each axis, x, y, z, respectively.

Therefore, using the expression (8.14), the tilt modulation $\mathcal{T}(\mathbf{r}, t)$ is given by the dot product

$$\mathcal{T}(\mathbf{r}, t) = \mathbf{n}(\mathbf{r}, t) \cdot \mathbf{u}(\mathbf{r}, t) = \cos \theta_i(\mathbf{r}, t) \tag{8.18}$$

where $\theta_i(\mathbf{r}, t)$ is the local angle of incidence due to the face orientation to the antenna (see figure 8.2).

3. Estimation of NRCS, σ_0: The estimation of σ_0 considers the local incident angle $\theta_i(\mathbf{r}, t)$ obtained from the tilt modulation $\mathcal{T}$ given by equation (8.18). Hence, from $\theta_i(\mathbf{r}, t)$, and assuming that the backscattering can be approached by the Small Perturbation Model (SPM) [44], and taking into account horizontal polarization, the fact of sea water presents good conductivity for X-band, and the wavelengths of the ocean waves are much larger than the decorrelation distance of the backscattering ripples that cause the backscattering, NRCS is approximately $\sigma_0(\mathbf{r}, t) \sim \cos^4 \theta_i(\mathbf{r}, t)$. Hence, taking into account the shadowing effect, NRCS is given by

$$\sigma_0(\mathbf{r}, t) \sim \mathcal{T}^4(\mathbf{r}, t) \cdot m(\mathbf{r}, t) \tag{8.19}$$

where m is the illumination mask defined in equation (8.11) and $\mathcal{T}$ is the tilt modulation (equation (8.18)). Note that, due to the effect of the illumination mask, equation (8.19) provides always zero or positive values, $\sigma_0 \geq 0$. From equation (8.19), RCS is computed considering a rectangular radar pulse as

$$\sigma(\mathbf{r}, t) \approx \sigma_0(\mathbf{r}, t) R \Delta R \Delta \phi.$$

4. Speckle noise: To simulate the speckle properties appearing on radar images, a multiplicative noise exponentially distributed [45] is applied to RCS, $\sigma(\mathbf{r}, t) \mapsto \sigma(\mathbf{r}, t) \cdot s(\mathbf{r}, t)$, where $s(\mathbf{r}, t)$ is the realization of the speckle noise for each sea surface position $\mathbf{r}$ at time t.

5. Radar equation: The range and RCS dependence appearing in the radar equation given by 8.9 is applied to each sea surface position $\mathbf{r}$ at time t.

6. Logarithmic amplifier: To simulate the responds of the radar amplifier the radar equation 8.9 is applied in a logarithmic version. Hence, excluding the variables that are not known of the radar antenna (e.g. G and A_{eff}), and taking into account equations 8.18 and 8.19, the received radar intensity signal is proportional to

$$4 \log[\cos \theta_i(\mathbf{r}, t)] + \log[s(\mathbf{r}, t)] + \log(\Delta R \Delta \phi) - 3 \log R \tag{8.20}$$

Note that for a logarithmic amplifier, the variables G and A_{eff} induce only an offset in the received signal. This offset should not be considered as marine radars are not calibrated systems and they only provide a set of grey level values.

7. Digitalization of the data: As marine radars are not calibrated radar systems (i.e. they do not provide direct information about the received power P_r, but a grey level pattern in the radar screen), the result of the simulated sea clutter is codified in a range of bits as the normal output of the video radar signal is sampled by the A/D converter of the WaMoS-II system. Using the same conditions that the WaMoS-II system install at FINO 1 research platform, the simulated data are codified in one unsigned byte.

There are still some physical phenomena that are not included in the scheme described above, like the background noise (see section 4.3.1), nor the dependence on the wind speed and direction, nor the electromagnetic diffraction mentioned before. In addition, additional features that appear in the radar imagery, like the hydrodynamical modulation is not considered either. In addition to those improvements, an exhaustive comparison of the simulated results with real measurements from WaMoS stations has been carried out. That would improve the simulation techniques providing more realistic sea clutter simulations. Figure 8.4 illustrates the corresponding simulated sea clutter image derived from the wave field shown in figure 8.1.
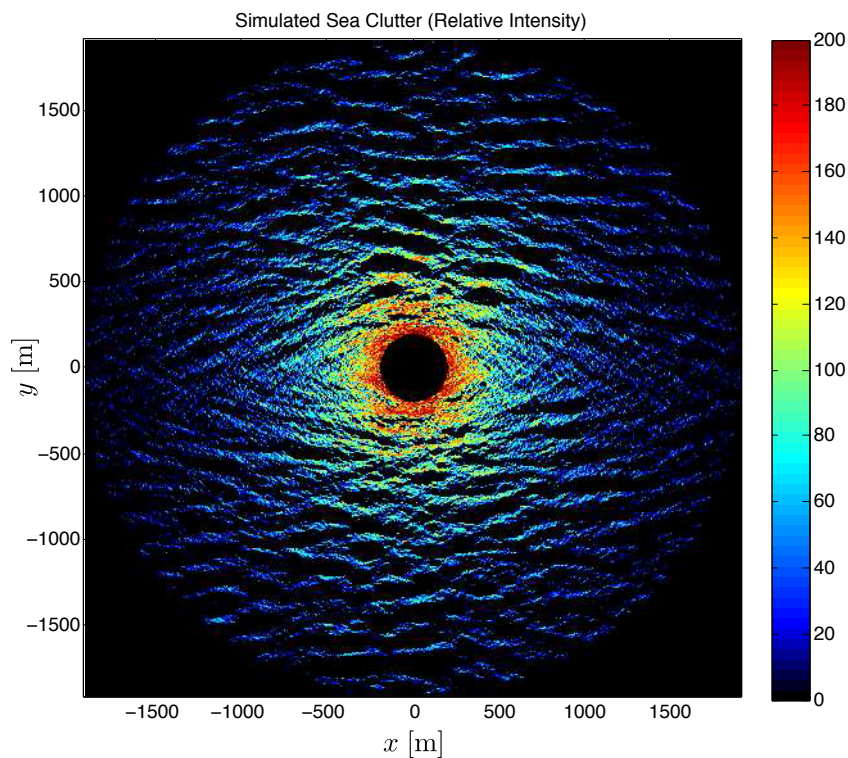
Figure 8.4: Simulated sea clutter image corresponding to the wind sea state shown in figure 8.1.

8.3   Example: image spectrum of a simulated sea clutter time series

This section shows an example of the sea clutter properties that can be reproduced from the simulation method described above. As an example, a sea state of an unimodal wave field has been numerically synthesised. The mean direction of the wave field is pointed to 270° (pointing to $y < 0$ direction). The simulated sea surface area is 4×4 km². And the simulated radar antenna is located at the three dimensional coordinate $(2000, -300, 40)$ [m]. For the simulation, a time series of wave elevation sea surfaces composed of 256 time steps, with a sampling time of $\Delta t = 2.5$ s, was derived. The spatial resolutions are $\Delta x = \Delta y = 7.5$ m. Those values correspond to the spatio-temporal resolution in the FINO 1 WaMoS-II set-up. Figure 8.5 shows the simulated sea surface (left side of the figure) for the first time step (i.e. $t = 0$ s), as well as the wave spectrum transect in the $(0, k_y, \omega)$-domain (right side of the figure). For this time step, the spatial derivatives, $\partial \eta / \partial x$ and $\partial \eta / \partial y$, used to define the unit exterior vector $\mathbf{n}$ (see expression (8.17)) are shown in figure 8.6.
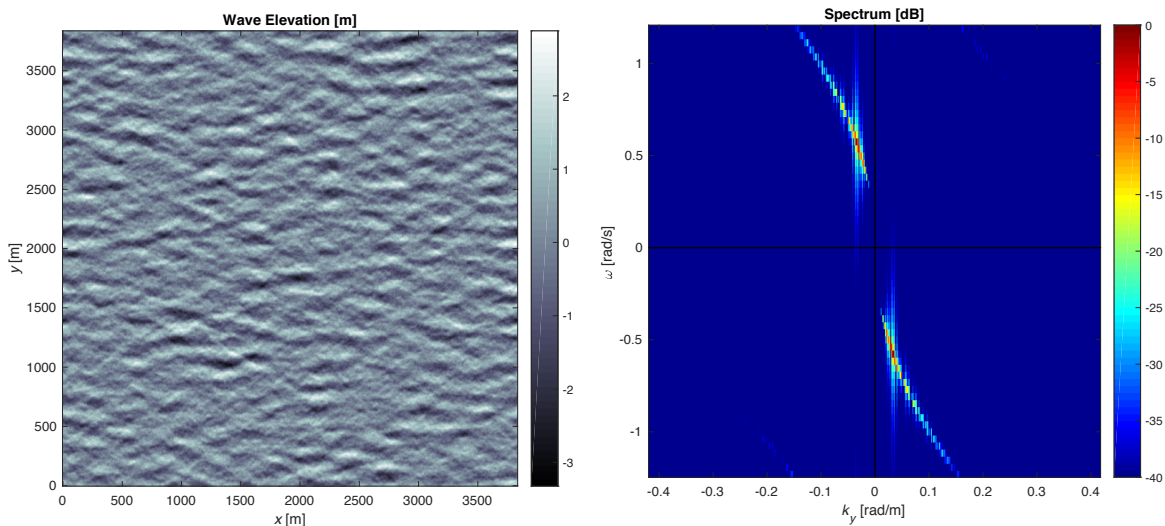
Figure 8.5: Simulated wave field with $f_p = 0.1$ Hz and $H_s = 3$ m (left) and corresponding wave spectrum transect in the $(0, k_y, \omega)$ domain, i.e. transect $k_x = 0$ (right).

For the first time step, the corresponding simulated radar image for these conditions and its related illumination mask are shown in figure 8.7. It can be seen how the shadowing (areas coded with black colour in the illumination mask) increases as the range R increases as well. It can be seen that the spectrum of the simulated radar image shown the main properties, such as the quasi-static patterns, for $|\omega| \approx 0$, the dispersion relation, the first harmonic, and the group line. In addition, those features, can be as well identified. This fact indicates that the shadowing is one of the most relevant modulation mechanisms for marine radar conditions (i.e. grazing incidence, incoherent radar receiver and HH-polarization).
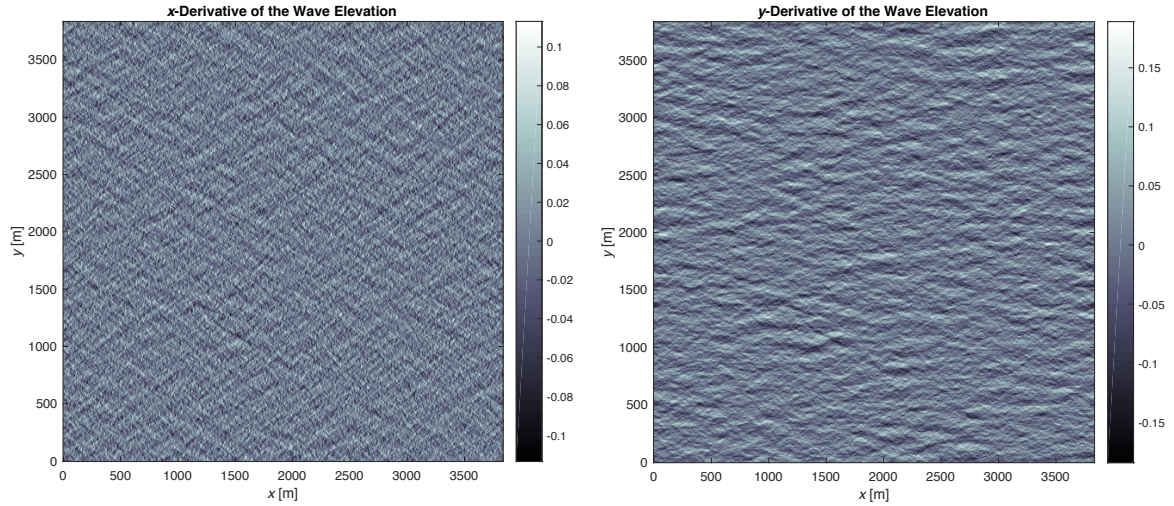
Figure 8.6: Spatial derivatives $\partial\eta/\partial x$ (left) and $\partial\eta/\partial y$ (right) of the simulated wave field shown in figure 8.5.
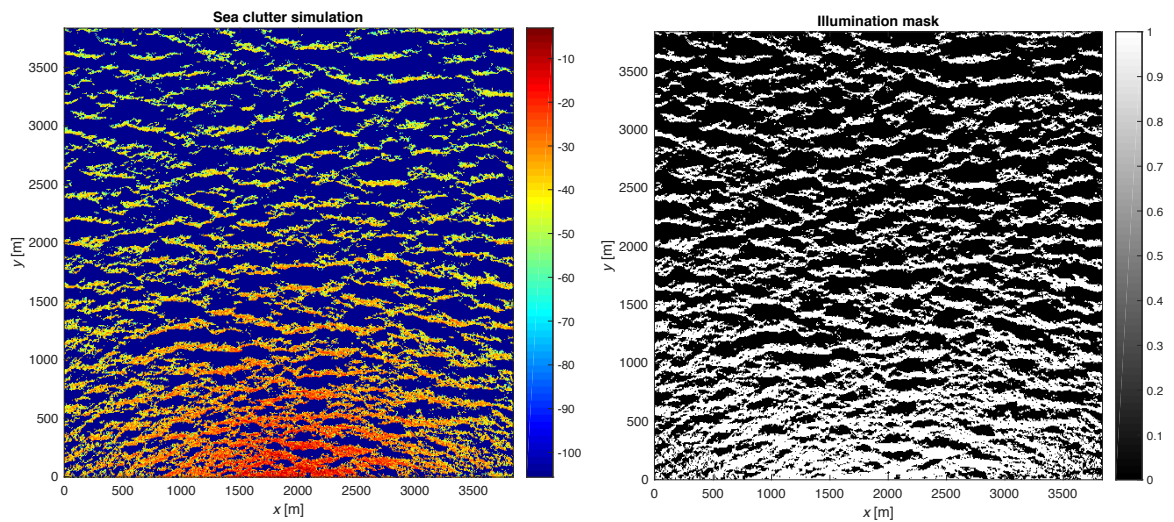
Figure 8.7: Simulated sea clutter image (left) and the corresponding illumination mask (right) for the simulated wave field shown in figure 8.5.

8.3.1 Illumination mask spectrum from real data acquired in FINO 1

In the previous text it was shown how the simulated illumination mask present the most relevant modulation features for grazing incidence and HH-polarization. This section shows a example of a real case measured in the FINO 1 platform. For the standard set-up of the WaMoS-II system in FINO 1, the length of the image time series is composed by 32 consecutive images. Therefore, in this case the expected frequency resolution is coarser than the examples above mentioned, which were obtained from the simulation scheme. Hence, figure 8.9 shows some time
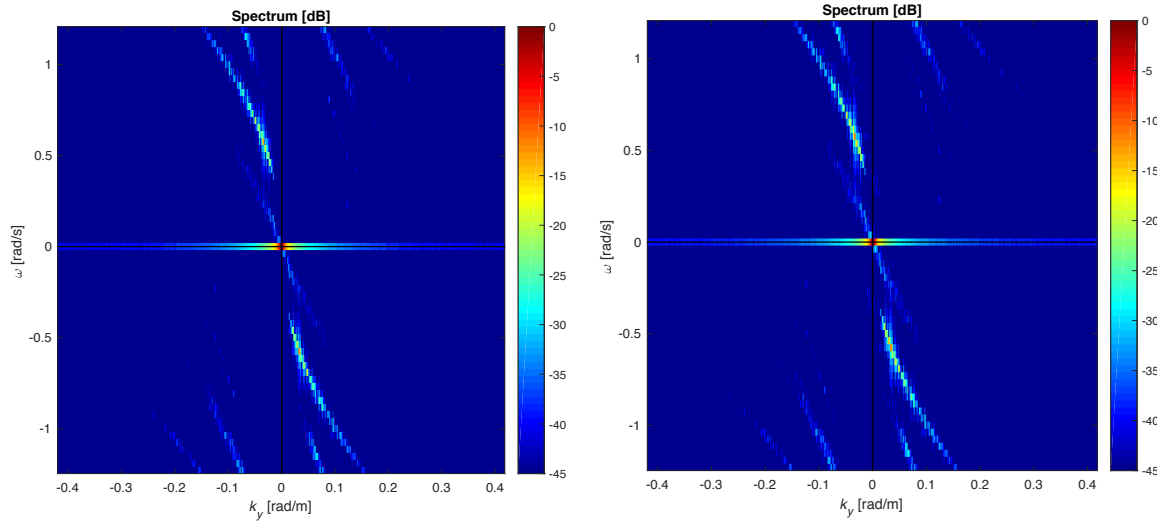
Figure 8.8: Image spectrum (left) of the simulated radar image shown in figure 8.7 and spectrum of the illumination mask (right). Both spectra are shown in the transect $k_x = 0$, $(0, k_y, \omega)$-domain.

steps of the analysis window of a sea clutter image and the corresponding illumination mask. The illumination mask has been obtaining by thresholding the values of the sea clutter intensity. Hence, for those values of the sea clutter higher than 1 byte, the illumination mask $m(\mathbf{r}, t)$ is set to 1, otherwise it $m(\mathbf{r}, t) = 0$. The corresponding spectral transect in the $(0, k_y, \omega)$-domain are shown in figure 8.10. It can be seen that the illumination mask spectrum keeps most of the relevant features of the image spectrum, such as the dispersion relation, the first harmonic (which is aliased in this case due to the coarse frequency resolution), as well as the group line. This indicates that the shadowing scheme described in this section is capable of reproducing most of the relevant features of the structure of the image spectrum.
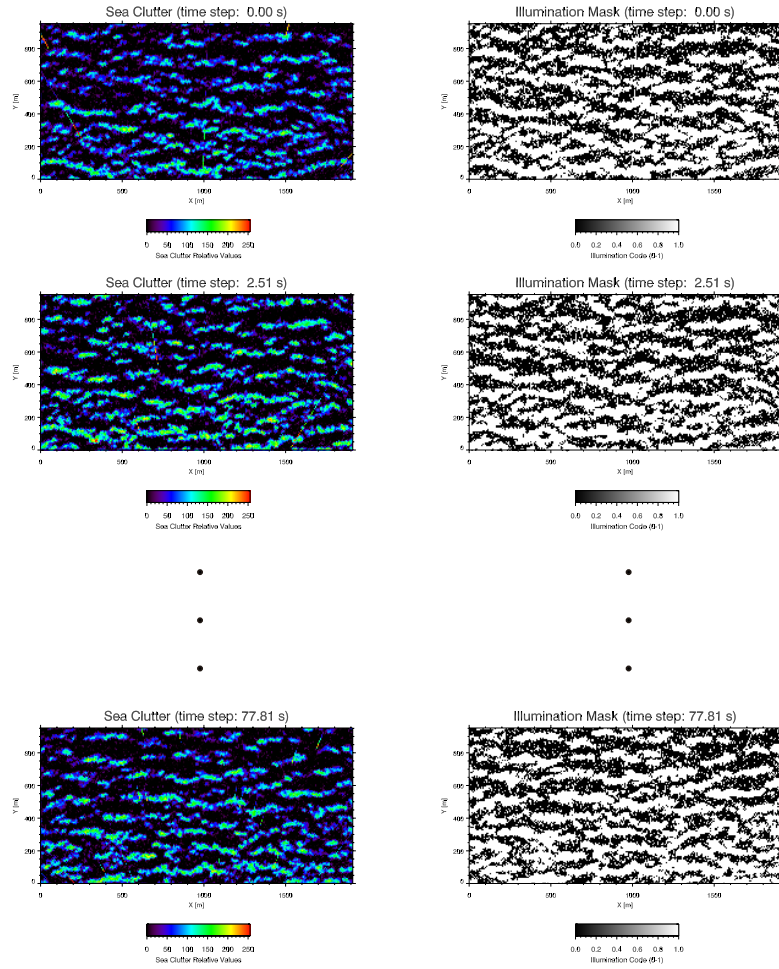
Figure 8.9: Example of sea clutter time series measured in Fino 1 platform (left) and the corresponding illumination mask (right).
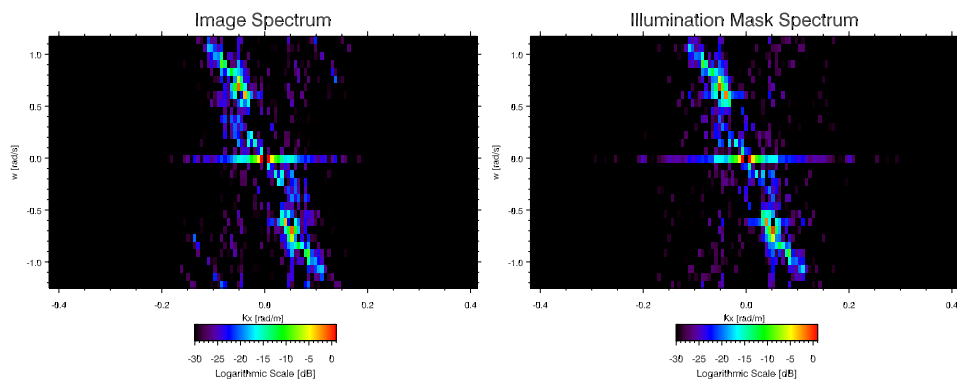
Figure 8.10: Image spectrum (left) and the corresponding illumination mask spectrum (right) of the image time series shown in figure 8.9. Both spectra are shown in the transect $k_x = 0$.

Chapter 9

Study of the Near-Surface Sea Current with Different Sensors

This work is focus on analysing X-band marine radar images to study the main characteristics of the sea such as the dispersion shell, the group line, the Signal to Noise Ratio and the wave height. But there is another important phenomenon to talk about, this is the *near-surface sea currents*.

This carried out study has been the aim of the article [46]. Considering that the remote sensing sensors and in-situ devices are not perfect, four *machine learning regressors base on artificial neural network* has been developed to improve the accuracy of the in-situ devices. The machine learning regressors are ANN trained by different algorithms such as Levenberg-Marquart and Extreme Learning algorithms, and other regressors as Support Vector Regression and Gaussian Processes.

The aim of this paper is taking the accurate current results provided by the in-situ device and correcting the estimation provided by the remote sensing sensors.

9.1 Sea current

Ocean currents are directed, continuous seawater movement, essential in the characteristics of the temperature in many of the Earth's regions. Tides are caused by the force of gravity of the Sun and the Moon. However, a sea current is generated by forces such as wind, breaking waves, cabbeling, tides, the Coriolis effect, the salinity and temperature differences. The direction and the strength of a current are due to interactions with other currents, shoreline configuration and depth profile.

The current is not constant related to depth, being less powerful in the bottom and stronger in the surface because of the atmospheric force. A significant part of the atmospheric momentum and energy fluxes goes into the waves. When the waves disappear, a flux of momentum and

turbulent kinetic energy from the waves to the ocean is generated. This is illustrated as a surface stress that accelerates the mean flow and increases near surface turbulent [47].

The current of encounter $\mathbf{U} = (U_x, U_y)$, is not a superficial current, but the weighted mean of the all currents existing in the superficial layer of the ocean [15]. Hence it is a contribution of different effects as relative velocity between the observer and swell, induced current produced by tides, the current produced by wind, the current introduced by swell and other currents associated by oceanic movement.

The main disadvantage of the marine radar to estimate the current of encounter is that the radar only considers the energy due to the wave field, refusing the spectral noise produced by the radar when the images are generated. Therefore, the high energy due to the wind sea is not considered in the estimation because this energy is in high frequencies where the effects of the radar noise are evident. The marine radar essentially measures the Eulerian current, measuring the signal in fixed regions in the sea surface.

9.2   The data set to analyse

The data are provided by the German research ice breaker vessel Polarstern. This vessel belongs to Alfred Wegener Institute for Polar and Marine Research. The length of the vessel is 118 m and is a double-hulled icebreaker, working even in temperatures equal to -50º C. It can break blocks of ice whose thickness is between 1.5 m to 3 m.

Figure 9.1: German research ice breaker vessel Polarstern.

The data used in this research are the measurements campaign over the North Sea (Norway and Greenland Sea) in May 2015. The data come from different sensors and all of them are complementary.

- Acoustic Doppler Current Profilers (ADCP): It is a hydroacoustic device that measures water current velocities over a range of depth applying the Doppler effect. The ADCP provides the three-dimensional current field information in a particular depth, giving accurate measurements. In this case, the data were collected as a 20 minutes average about 25 m water depth below the sea surface.

- WaMoS II System: Otherwise the X-band marine radar, provides the value of the sea surface current. But this value has a strong dependency on the local wind and the wave field conditions.

- Wind data measurements: These wind data were recording as well, and they were used to estimate the current.

9.3 Current field estimations by X-band marine radar

In all this work it has been commented that the marine radar images show the images related to the movements of the free sea surface. The current provided by the marine radar is the current or velocity of encounter [7], which is used to determine the dispersion relation. The marine radar only estimates those currents encounter which take part in the dispersion shell, it means, those which are generated by the wind that, at the same time, generate waves. The rest of the currents that are not considered in the dispersion relation, are disregarded. Besides, the current of encounter is sensitive with geophysical phenomena that cause current fields that could affect ocean waves, and the relative motion, doing a correction if the measure has taken on board:

$$\mathbf{U}^{\mathrm{geo}} = \mathbf{U}^{\mathrm{enc}} - \mathbf{U}^{\mathrm{gps}} \tag{9.1}$$

being $\mathbf{U}^{\mathrm{enc}}$ the current of encounter, $\mathbf{U}^{\mathrm{gps}}$ the course information of the GPS of the boat and $\mathbf{U}^{\mathrm{geo}}$ is the geophysical effects that can be written as:

$$\mathbf{U}^{\mathrm{geo}} = \mathbf{U}^{\mathrm{qe}} + \mathbf{U}^{\mathrm{wav}} \tag{9.2}$$

The geophysical current is due to the $\mathbf{U}^{\mathrm{qe}}$ quasi-Eulerian current and $\mathbf{U}^{\mathrm{wav}}$ wave factor or Stokes drift. The quasi-Eulerian current is a combination of different contributions such as internal motion, wind drifts and tides. This current is a weighted average of the current from the surface down to the penetration depth of the water particle orbital motions due to the wave. When the penetration depth increases, the weighted average decreases.

Therefore, X-band marine radars estimate the current of encounter with less accuracy than the in-situ devices, like ADCPs. This is the reason to use *machine learning regression techniques* to correct the current estimation by the radar, in order to get the accuracy measurement provided by the ADCP.

9.4   Machine Learning regression techniques

Machine Learning is a part of *Artificial Intelligent* that allows for creating systems capable to learn by themselves from a data set without explicit programming and whose purpose is predicting the future, events, tags, etc. These systems need techniques and algorithms to create predictive models and patterns. For these techniques the training vector, or predictive variable, is formed by the measurements of the current at a giving point in the sea obtained by the ADCP.

The regression techniques in [46], which are going to be commented, are:

- Multilayer Perceptron (MLP): It is a kind of ANN used to model nonlinear problems. It is capable to learn and generalise from input patterns to the known output targets, minimizing the error between the output generated by the MLP and the corresponding known output. A brief theory about neural network is collected in the annex B.

- Extreme Learning Machines (ELM): It is an avant-garden and fast learning method which is based on a feed-forward MLP structure. The most important characteristic is that the weights in hidden layer are not calculated and for this reason, this layer do not need be trained. The network weights are setting randomly and then a pseudo-inverse of hidden layer output matrix is estimated. A summarise of ELM can be found in the annex C.

- Gaussian Process for Regression (GPR): It is a generic supervised learning method use to solve regression problems. GPR is a kind of continuous stochastic process that defines a distribution of probability for functions and inferences taking place directly in the space of functions. In the annex D it is able to find a brief synopsis.

- Support Vector Regression algorithms (SVR): They are a set of supervised learning algorithms developed by Vladimir Vapnik and his team. They are related to linear classification and regression problems. A SVM builds a hyperplane in high dimensional space, where the hyperplane separates in optimal way the samples of different classes. The SVM searches the hyperplane whose distance between the samples and itself is maximal. A brief review is collected in the annex E.

9.5   Experimental results

The marine radar data provide spatio-temporal information, whereas the ADCP data give in-situ information about the temporal average of the current $\mathbf{U}^{i-s}$ for different depths. Machine Learning gives the opportunity to correct the estimation of the velocity of encounter estimated by the marine radar to the geophysical current $\mathbf{U}^{\text{geo}}$. Because of the depth, waves and wind conditions, generally, the modulus of the current given by the ADCP is lower than the current expected by the WaMoS system.

The study is focused on the modulus and the phase of the current of encounter. The best correction for the modulus $|\mathbf{U}^{\text{geo}}|$ and the phase Θ_U^{geo} are obtained by the GPR. The figures 9.2
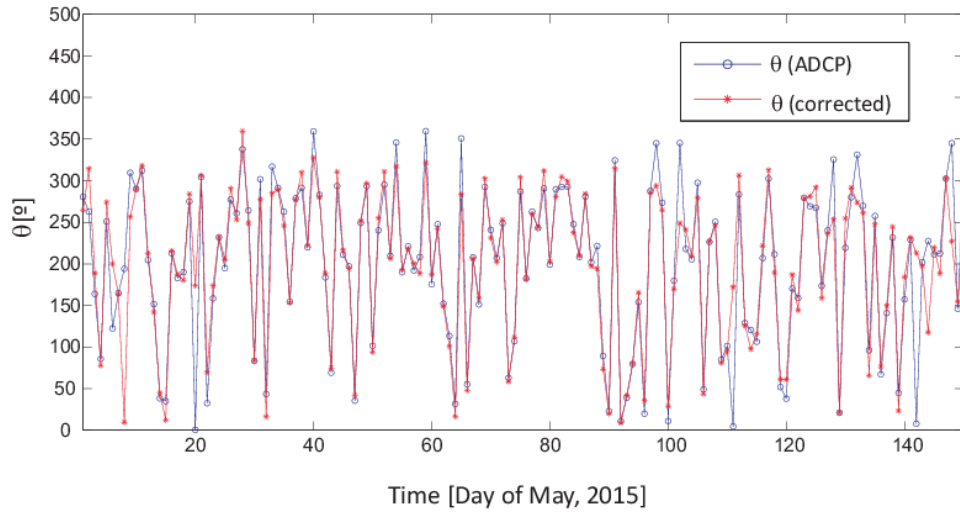
Figure 9.2: Θ_{II}^{geo} correction with GPR.
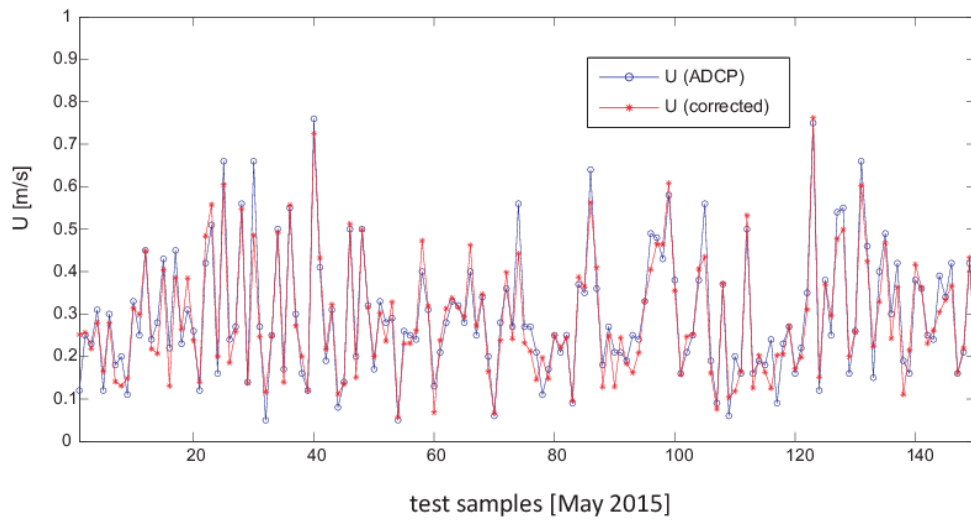
Figure 9.3: $|\mathbf{U}^{\text{geo}}|$ correction with GPR.

and 9.3 show the results with the best correction, the GPR, in phase and in modulus of the current. But three sea state parameters such as significant wave height, mean and peak period are used as well to correct the estimations.

Chapter 10

Conclusions

The spectra of the X-band marine radar images have been examined exhaustively. The targets of this analysis are the phenomena related to waves, which are visible in the radar image spectra because of their energy distributions. The main energy is located in the dispersion relation caused by the spatio-temporal dynamics of the waves. Hence, the dispersion shell relates the dependency between the angular frequency and the wave number describing the shape of the wave propagation. The spectral energy of the dispersion relation depends on external factors like the wind strength, this is the main reason that the data selected to carry out the study had to have high values of significant wave height. This consideration avoid those cases of low backscatter, with weak dispersion relation, higher harmonics and group line features that cannot permit to derive conclusive results. The main conclusion are summarised as:

- The intensity of the dispersion relation is high in near range, however it is weaker in far range.

- The shape definition of the dispersion relation is better in far range than in near range, because the noise of background is weaker. In addition, for moderate far range the shadowing modulation is stronger, which contributes to an easier detection of the dispersion shell.

- In cross azimuthal direction, respect to the wave direction, the intensity is weaker and the dispersion relation shape is not very well defined, and the background noise is higher.

Therefore, the detection of the dispersion relation is optimal for far range and in mean wave propagation direction, or 180° off the mean wave propagation direction. Therefore, the intensity of the dispersion relation is weaker, but the shape is very well defined, however in near range the dispersion relation and the group line are very close of each other, and it is difficult to isolate both features.

Another important part of energy is located in the group line, in the centre of the spectrum for small values of ω. The group line is the combination of different contributions, such as nonlinear phenomena existing in the surface of the ocean, such as the wind, the effects produced

by the waves breaking, etc. The group line study is not easy because of the closeness with the dispersion shell, making its isolation difficult. Moreover, the size and the intensity of the group line is modified by the intensity of the wind, the wave direction and the range in the radar image. The group line, how it can be shown in this work, can be characterised by

- The group line can be considered as a subharmonic of the dispersion relation, such as the subtraction of two fundamental modes. Hence, $\mathbf{k}_{GL} = \mathbf{k}_2 - \mathbf{k}_1$ and $\omega_{GL} = \omega_2 - \omega_1$.

- The spectral intensity of the group line is higher in the near range.

- The shape definition of the group line is better in far range than in near range. The high intensity level makes difficult to extract it, because the most of the cases the dispersion shell and the group line are very close located.

- In cross azimuthal direction, respect to the wave direction, the intensity is a bit lower, but this variability in the intensity is not so pronounced as in dispersion relation case, and the shape is not very well define, and the background noise is high.

- The intensity of the group line spectrum is bigger than the intensity of the dispersion relation spectrum.

- In addition, the stochastic simulations of radar images, as well as the real data, show that shadowing induces the group line features. So, the group line is caused as well by the radar imagery at grazing incidence, and not only due to geophysical reasons.

The dispersion relation is the desired signal of this study, and the background noise, with or without interpolation, it is the noise. Depending on considering what is signal and what is noise, different definitions of SNR can be done. But independently of this, all of the SNR commented in the work have the same tendency:

- For near range, the values of SNR are greater than for far range.

- The tendency of the curves are equivalent. The SNR takes the lowest values for the azimuths around the cross direction, however the highest values are nearby the main direction and the wave direction.

- The estimation of the SNR is not affected by the group line. Although the individual values of the image spectrum for the group line spectral $(\mathbf{k}, \omega)$-components are comparable with the spectral values corresponding to the $(\mathbf{k}, \omega)$-components within the dispersion shell, the integral of those values does not affect significantly to the different estimations of SNR. That means that the important contribution to SNR came from the dispersion shell itself.

When the significant wave height is low or the front of waves is vague, the results are not so good, because the energy of the phenomena is weak and their definition of the shape are not so clear, being the backscatter noise very high in comparison with the phenomena. For this reason, the results obtained for Hörnum data set are not so good, whose significant wave height is less than 1.6 m and the front of waves is not defined.

Moreover the real data provided by the stations FINO 1 and Hörnum, simulation techniques have been employed. Radar imagery have been obtained from simulated stochastic wave field from the sea surface elevation, getting realistic synthetic sea clutter images. The simulations techniques assume the characteristics and operation conditions of a conventional marine radars, considering the main sea surface modulation mechanism for grazing incident and horizontal polarization such as shadowing and tilt modulation, and what is more, they consider logarithmic amplifier and incoherent system with no frequency agility. The illuminated mask is generated, being equal to 1 the facet of the sea surface illuminated by the radar, and 0 for the rest. The most important is that the illuminated mask includes the main contributions of the image spectrum. It means, in the spectrum of the illuminated mask there are the dispersion relation, the higher harmonics such as the first harmonic, and the subharmonic group line.

Part III

Appendices

Appendix A

Basic Hydrodynamics Theory of Waves

The basic theory of waves is based on the studies of Bernoulli and Euler (in $XVIII$ century), Airy (1845) and Navier and Stokes (1847) [48]. From 1960, the spectrum description of the waves was a high impact because of the Fourier spectrum analysis [49, 50].

A.1 Fluid fundamental equations

The main fluid fundamental equations are:

- The law of conservation of mass:
  The quantity of mass is *conserved* over time. So for any system closed to all transfers of matter and energy, the mass of the system must remain constant over time, as system mass cannot change quantity if it is not added or removed. The main variable is the density $\rho(\mathbf{x}, t)$, where $\mathbf{x} = (x, y, z) \equiv (x_1, x_2, x_3)$. Hence, *density × volume* is *constant* and it can be written as:

$$\frac{\mathrm{d}}{\mathrm{d}t}(\rho J) = 0 \tag{A.1}$$

Where J is the Jacobian of the distortion of the particles happened between the time instants $t = 0$ and t, and $\mathrm{d}/\mathrm{d}t$ can be expressed as:

$$\frac{\mathrm{d}}{\mathrm{d}t} = \frac{\partial}{\partial t} + \mathbf{u} \cdot \nabla = \frac{\partial}{\partial t} + \sum_{i=1}^{3} u_i \frac{\partial}{\partial x_i} \tag{A.2}$$

Where $\mathbf{u} = (u_1, u_2, u_3)$ is the velocity. Hence, J is the volume expansion in a trajectory and its derivative in time is:

$$\frac{\mathrm{d}J}{\mathrm{d}t} = J\nabla \cdot \mathbf{u} \tag{A.3}$$

So the equation (A.1) can be written as:

$$\frac{\mathrm{d}}{\mathrm{d}t}(\rho J) = \frac{\mathrm{d}\rho}{\mathrm{d}t}J + \rho J (\nabla \cdot \mathbf{u}) \tag{A.4}$$

If it is expressed as a partial derivative, it is obtained the general equation:

$$\frac{\partial \rho}{\partial t} + \nabla \cdot (\rho \mathbf{u}) = 0 \tag{A.5}$$

- The law of momentum conservation:
  The total momentum of a collection of objects (a system) is conserved, that is, the total amount of momentum is a constant or unchanging value. The amount of movement is caused by different strengths such as f_e, force due to the external fields such as gravitational field, f_c contact force and f_v due to the viscosity. Hence, the momentum conservation for fluids is:

$$\rho \left(\frac{\partial \mathbf{u}}{\partial t} + \mathbf{u} \cdot \nabla \mathbf{u} \right) = -\nabla p + \lambda \nabla (\nabla \cdot \mathbf{u}) + \mu \nabla \mathbf{u} + f_e(\mathbf{x}, t) \tag{A.6}$$

Where p is the pressure, the parameters μ and λ are related to the viscosity of the fluid and ρ is the density.

Both equation (A.5) and (A.6) are nonlinear.

A.2 Euler's equations. Perfect fluids

Because of the problematic to find a mathematical model to describe the behaviour of the fluids, Euler simplified the problem considering two clauses:

- Fluids are incompressible: Fluids can not be compressed. This means that J is a constant equal to 1 and the density $\rho(\mathbf{x}, t)$ is a constant in time. For these reasons, it can be written:

$$\frac{\partial \rho}{\partial t} = 0 \tag{A.7}$$

$$\nabla \cdot \mathbf{u} = 0 \tag{A.8}$$

- Fluids are perfect: Fluids do not suffer the viscous effects, this means perfect fluids have no shear stresses, viscosity, or heat conduction ($\mu = \lambda = 0$). The contact force f_c is equal to the pressure component $f_p = -\nabla p$, so:

$$\rho \left(\frac{\partial \mathbf{u}}{\partial t} + \mathbf{u} \cdot \nabla \mathbf{u} \right) + \nabla p = f_e(\mathbf{x}, t) \tag{A.9}$$

And even it can be simplified considering $\rho = 1$.

These equations reduce the complexity of the dynamic fluids giving good accuracy to experimental results.
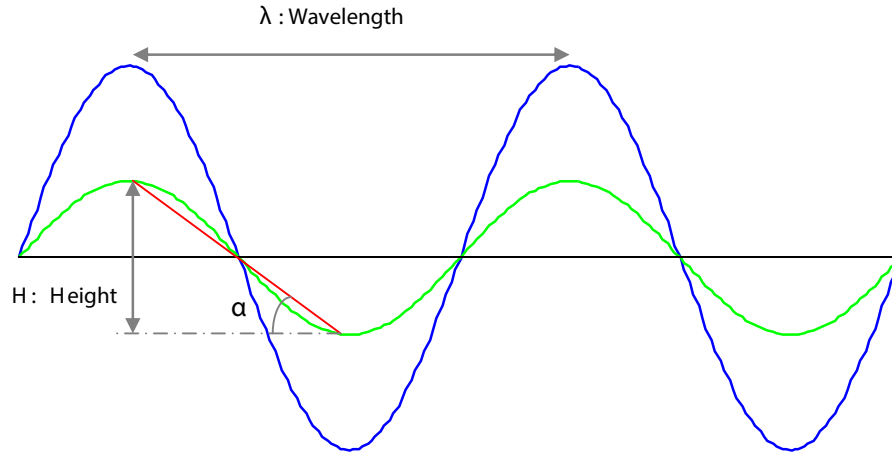
Figure A.1: Airy's model and the most important parameters of the waves.

A.3 Airy's theory. Linear wave

The hydrodynamics theory is nonlinear, but Airy's theory promulgated the simplest one. George Airy considered these hypothesis to simplify the complexity in hydrodynamics theory:

- Fluids are incompressible and no viscous.

- Considered main forces are the gravity and the pressure, and the superficial tangential components are negligible.

- The bottom of the sea is deep, the depth is constant and impervious.

- The motion is irrotational, so $\nabla \times \mathbf{u} = 0$.

- The wave is periodic, regular, two-dimensional and stationary.

- The amplitude is smaller than the wavelength and the depth.

The free surface elevation is considered as a sinusoidal wave with horizontal position x, time t and z is the vertical coordinate (positive in the upward direction):

$$z = \eta(x,t) = \frac{H}{2}\cos(kx - \omega t) \tag{A.10}$$

The figure A.1 represents the waves that are considered in this theory. The main parameters are shown as well.

- The wavelength (λ) is the distance between two consecutive maxima.

- The height (H) is the vertical distance between the maximum and minimum.

- The slope (the red line in the figure A.1) can be estimated as $tg(\alpha) = 2H/\lambda$.

- The wave number, related to the wavelength, is equal to $k = (2\pi)/\lambda$.

- The angular frequency (ω), related to the frequency (f) and the period (T), is equal to $\omega = 2\pi f = 2\pi/T$

- The wave celerity (C) is the speed of propagation of an ocean surface wave $C = \lambda/T = \lambda \cdot f$.

The accepted hypothesis for this theory involve to consider the equations (A.7), (A.8) and (A.9) as the basis of the study. Besides it is necessary to know the main equations which manage the swell propagation in an ideal fluid and the boundary conditions for this problem:

- Laplace's equation: The mass and the volume do not suffer any variation in time for incompressible and irrotational fluids. Hence, the velocity potential $\phi(x, z, t)$ must comply:

$$\frac{\partial^2 \phi}{\partial x^2} + \frac{\partial^2 \phi}{\partial z^2} = 0 \tag{A.11}$$

- Boundary condition in the bottom of the sea: The flow velocities have to go to zero in the limit as the vertical coordinate goes to minus infinity:

$$\text{For } z = -d \quad \Rightarrow \quad \frac{\partial \phi}{\partial z} = 0 \tag{A.12}$$

Where d is the depth of the sea.

- The first boundary condition for free surface: The vertical motion of the flow has to be equal to the vertical velocity of the free surface $(\eta(x, t))$:

$$\frac{\partial \phi}{\partial z} = \frac{\partial \eta}{\partial t} + \frac{\partial \phi}{\partial x}\frac{\partial \eta}{\partial x} \tag{A.13}$$

Because of the amplitude of the wave is very small in compare to the wavelength, it is said that $z \approx 0$. Therefore the equation (A.13) can be written:

$$\frac{\partial \phi}{\partial z} = \frac{\partial \eta}{\partial t} \tag{A.14}$$

- The second boundary condition for free surface: This is provided by Bernoulli's equation for an unsteady potential flow:

$$\frac{\partial \phi}{\partial t} + \frac{P_{atm}}{\rho} + \frac{1}{2}\left(\nabla\phi\right)^2 + g\eta = 0 \tag{A.15}$$

In free surface the atmospheric pressure P_{atm} can be considered equal to 0.

$$\text{For } z = 0 \quad \Rightarrow \quad \frac{\partial \phi}{\partial t} + g\eta = 0 \tag{A.16}$$

- Lateral boundary conditions: The waves are regular, so there is a periodicity in time (T) and in wavelength (L):

$$\phi(x, t) = \phi(x + L, t) \quad \text{and} \quad \phi(x, t) = \phi(x, t + T) \tag{A.17}$$
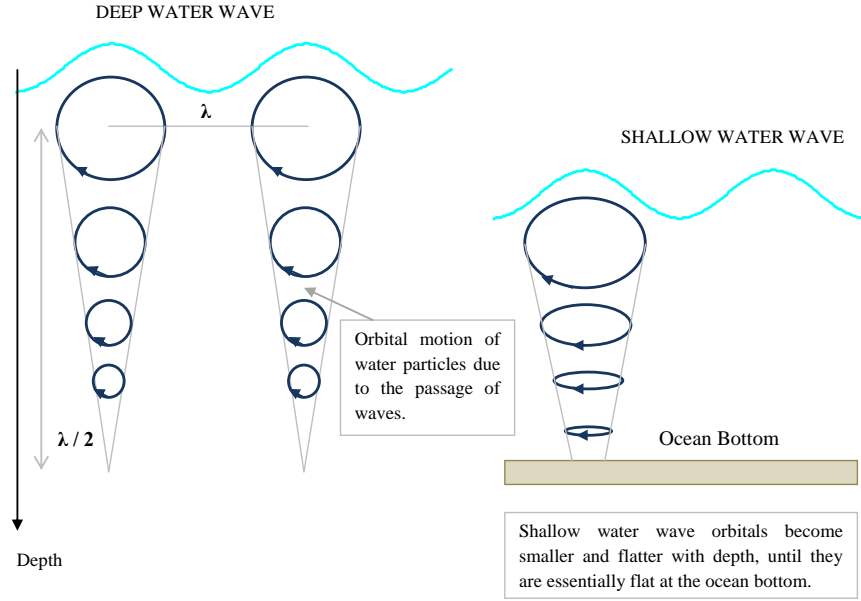
Figure A.2: Airy's linear theory of wave motion breaks down when waves enter shallow water. Adapted from New South Wales Coastline Management Manual (1990).

Airy supposes that the velocity potential $\phi(x, z, t)$ can be calculated like the product of three independent terms and being a solution of Laplace's equation:

$$\phi(x, z, t) = X(x) \cdot Z(z) \cdot R(t) \tag{A.18}$$

To make this possible, the term $R(t)$ must be regular and considered $R(t) = \sin(\omega t)$. Therefore, the velocity potential can be written as $\phi(x, z, t) = X(x) \cdot Z(z) \cdot \sin(\omega t)$ and the Laplace's equation (A.11) will be:

$$\frac{1}{X}\frac{\partial^2 X}{\partial x^2} + \frac{1}{Z}\frac{\partial^2 Z}{\partial z^2} = 0 \tag{A.19}$$

If the method based on separation of variables using partial derivatives is applied, the solution is:

$$\phi(x, z, t) = (A \cdot \cos(kx) + B \cdot \sin(kx)) \cdot \left(C \cdot e^{kz} + D \cdot e^{kz}\right) \cdot \sin(\omega t) \tag{A.20}$$

The value of the constants are obtained from the boundaries conditions and the solution for the velocity potential is:

$$\phi = \frac{H}{2}\frac{g}{\omega} \cdot \frac{\cosh\left(k(d+z)\right)}{\cosh\left(d+z\right)} \cdot \sin\left(k \cdot x - \omega t\right) \tag{A.21}$$

From this equation and considering the equation (A.16), the surface elevation can be estimated and the result would be (A.10):

$$\eta = \frac{1}{g} \cdot \left.\frac{\partial \phi}{\partial t}\right|_{z=0} = \frac{H}{2}\cos(kx - \omega t) \tag{A.22}$$

And what is more, the wavelength can be calculated by successive iterations from the formula:

$$\lambda = \frac{g}{2\pi} \cdot T^2 \cdot \tanh\left(\frac{2\pi d}{\lambda}\right) \tag{A.23}$$

The main conclusions got from Airy's theory are the following and the figure A.2 shows them:

- For deep water $(d \geq (\lambda/2))$, the fluid particles follow circular path, whose diameter suffers an exponential decrease when the depth increases.

- For intermediate depth $(\lambda/2 > d > \lambda/20)$, the particles follow elliptical path and the axis, the major (parallel to the surface) and the minor, decrease exponentially when the depth increases.

- For shallow water $(d \leq (\lambda/20))$, the trajectory is elliptical as well but the major axis is independent with the depth.

This approximation gives very good results, but only when the swell is low, it means the slope is between the values 0.05 and 0.08. If the crest is higher, it is necessary to use the nonlinear theory, such as *Navier-Stokes* for deep water and *Cnoidal* for shallow water.

A.4   Navier-Stokes' equation. Viscous fluids

The Navier-Stokes' theory gives a good description of the real swell. The fluid has its own volume and takes up Ω domain, where $\Omega \subset R^2$ or R^3. For each point of Ω there is fluid and for each instant of time t, the fluid particles present a bijective correspondence with the coordinates $\mathbf{x} = (x_1, x_2, x_3) \in \Omega$. The fluid can be characterised for these statements:

- Velocity field is the velocity of each particle in each point of the domain $x(x_1, x_2, x_3) \subset \Omega$ in every instant of time t: $\mathbf{u}(x,t) = (u_1, u_2, u_3)(x,t)$.

- The pressure in the fluid: $p = p(x,t)$.

- The fluid density: $\rho = \rho(x,t)$.

These equations are based on conservation of mass (A.5), the non-compressibilty of the fluids (A.8) and the second Newton's law, linked the particle acceleration and the forces, such as gravity, friction or viscosity. They consider that the fluids are viscous and the value of the viscosity ν is constant. Therefore, the equations are:

$$\frac{\partial \rho}{\partial t} + \nabla \cdot (\rho \mathbf{u}) = 0 \tag{A.24}$$

$$\nabla \mathbf{u} = 0 \tag{A.25}$$

$$\frac{\partial \mathbf{u}}{\partial t} + \mathbf{u} \cdot \nabla \mathbf{u} = -\frac{1}{\rho}\nabla p + \nu \nabla \mathbf{u} + \mathbf{F}_\epsilon \tag{A.26}$$

where ν is the kinematic viscosity and $\mathbf{F}_\epsilon$ is all the external forces. In cartesian coordinates, this last expression can be written:

$$
\begin{aligned}
\frac{\partial u_1}{\partial t} + u_1 \frac{\partial u_1}{\partial x} + u_2 \frac{\partial u_1}{\partial y} + u_3 \frac{\partial u_1}{\partial z} &= -\frac{1}{\rho}\frac{\partial p}{\partial x} + \nu \left(\frac{\partial^2 u_1}{\partial x^2} + \frac{\partial^2 u_1}{\partial y^2} + \frac{\partial^2 u_1}{\partial z^2} \right) + F_x \\
\frac{\partial u_2}{\partial t} + u_1 \frac{\partial u_2}{\partial x} + u_2 \frac{\partial u_2}{\partial y} + u_3 \frac{\partial u_2}{\partial z} &= -\frac{1}{\rho}\frac{\partial p}{\partial y} + \nu \left(\frac{\partial^2 u_2}{\partial x^2} + \frac{\partial^2 u_2}{\partial y^2} + \frac{\partial^2 u_2}{\partial z^2} \right) + F_y \quad \text{(A.27)} \\
\frac{\partial u_3}{\partial t} + u_1 \frac{\partial u_3}{\partial x} + u_2 \frac{\partial u_3}{\partial y} + u_3 \frac{\partial u_3}{\partial z} &= -\frac{1}{\rho}\frac{\partial p}{\partial z} + \nu \left(\frac{\partial^2 u_3}{\partial x^2} + \frac{\partial^2 u_3}{\partial y^2} + \frac{\partial^2 u_3}{\partial z^2} \right) + F_z
\end{aligned}
$$

Equation (A.26) is nonlinear and some of the more complex equations in the classical physics, which cannot be not analytically solved to obtain exact solutions of them.

Appendix B

Artificial Neural Networks

The human brain is capable to interpret the vague information provided by the senses in a very high speed. Neurons are highly specialized cells that make up the nervous system. The nervous system is proactive and constantly makes assumptions about the environment. Neurons can communicate with precision, speed and long distance with other cells, even if these cells are nerves, muscles or glands. But the most important neurons are brain cells, that have functions related to thinking, learning and memory. A set of physically interconnected neurons or a group of single neurons that receive signals processed in a recognizable way is what is known as *neural network*.

Nowadays, information treatment systems have been developed to work such as human brain, because of features such as robustness, flexibility, adaptive learning, the way it uses the vague information, low energy consumption, parallel data processing, very high speed and working in real time.

Artificial Neural Networks (ANNs) emulate the biological neural network behaviour. ANNs are the best choice in complicate situations where conventional methods do not get suitable solutions. ANNs can implement a nonlinear function between the input and output. Therefore, they are used in a wide range of applications such as pattern recognition [51], sonar, marine radar [52] (particularly to detection ships [53]), prediction, control and optimization, voice and images processing, process of noise elimination, etc.

Conventional computation systems work in a sequential way, and they usually have only one processor to manipulate data and instructions that are stored in the memory. However, ANN is a parallel system that do not execute instructions and the result is not stored in a memory cell, but it represents the state of the network when the equilibrium is achieved. Therefore, the power of the ANN is in its own topology and the connection values (*weights*) among the interconnected neurons.

B.1   Artificial Neural Network (ANN)

Artificial neural networks are information processing systems whose structure and function are inspired by biological neural networks of the human brain. ANNs do not reach the complexity of the brain, however there are two similarities between artificial and biological networks: the first is that the building blocks of both networks are simple computational elements highly interconnected, and the second is that the connection between neurons determines the function of the network.

An artificial neuron is equivalent to a circuit that performs a weighted sum of the parallel input signals and obtains an output whose value is 1 or 0 depending on the result of the sum relative to a trigger level or threshold. The ANN is an interconnection between neurons in a determined way.

- Entries p_i represent the input signals to the neurons.

- w_i represent the weights.

- φ is the transfer function that limits the amplitude of the output signal.

w_i and p_i signals are real, but with the distinction that in biological cells are discrete variables and continuous variables in the ANN. The output of the ANN is given by three functions:

- Propagation function: Is the sum of each input multiplied by the weight of their interconnection.

- Activation function: Makes a change on the previous one, and may not exist.

- Transfer function: Applies to the value returned by the activation function (and if it does not exist on the propagation). It is used to limit the output of the neuron.

Each input signal is multiplied by a weight or gain. This weight may be positive (exciting) or negative (inhibitor). The sum node adds up all weighted signals. The transfer function or threshold is applied to the resulting signal to get later the output signal. The output signal can be expressed such as

$$\mathbf{y} = \varphi \left(\sum_{i=1}^{m} \mathbf{w}_i \, \mathbf{p}_i + b \right) \tag{B.1}$$

The signal $\mathbf{y}$ can be expressed in matrix notation as

$$\mathbf{y} = \varphi \left(\mathbf{W}^T \mathbf{p} + b \right) \tag{B.2}$$

where the input and the weights vector are:

$$\mathbf{p} = [p_1, p_2, ..., p_m]^T, \quad \mathbf{W} = [w_1, w_2, ..., w_m]^T \tag{B.3}$$

$$y = \text{f}(\mathbf{wp} + b) \qquad\qquad y = \text{f}(\mathbf{wp} + b)$$
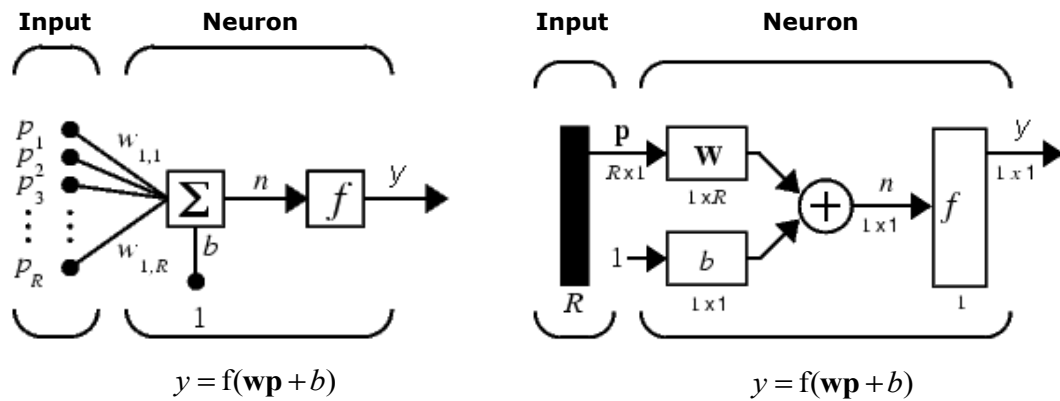
Figure B.1: At left, single artificial neuron. At right, its equivalent with abbreviated notation.

After calculating node activation is necessary to calculate the output value, with φ transfer function for that unit, which corresponds to the chosen function to transform the net input into output value; This function depends on the specific characteristics of each network.

Another way to represent a single neuron is shown in figure B.1 using a different notation. In this case the input signals are referenced by $p_1, p_2, ..., p_R$ where R is the number of elements of input vector and b is the gain of the neuron.

B.1.1 Classification of artificial neural networks

Artificial neural networks are classified into different categories according to different criteria:

- Given the network topology, the ANNs can be classified according to the number of layers, or the number of neurons per layer, or even the type of connection between them. If we consider the latter option, the classification is:

    1. Feedforward: The information is transmitted in one direction, passing from the input layer to output layer, through hidden layers previously, if they exist.
    2. Feedback: It has at least one closed loop, so the information can form loops, and even establish intralayers connections.

- However, if the number of layers is considered as a criterion, it is distinguished:

    1. Single layer: It consists of a single layer of neurons, performing connections between neurons that form the network. Figure B.2 shows the ANN structure of a single layer.
    2. Multilayer: Hierarchies neurons are sited in different layers. At least, it has an input layer and output layer, and it may have one or more intermediate or hidden layers. Figure B.3 shows this structure.

- Considering the learning or training system used by ANNs, the classification is defined as:

$$\mathbf{y} = \mathrm{f}(\mathbf{W}\mathbf{p} + \mathbf{b})$$
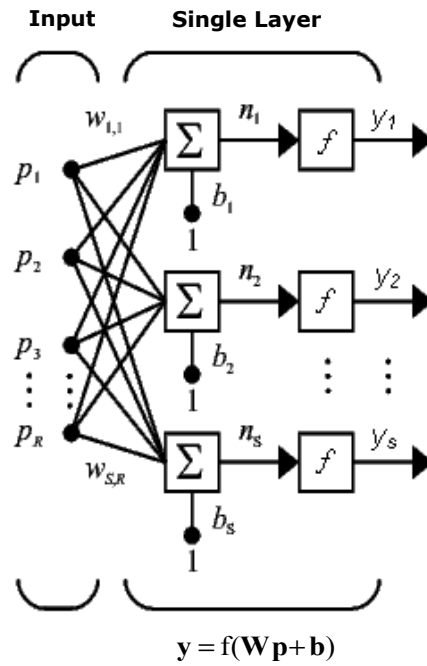
Figure B.2: Single layer ANN with S neurons.

1. Supervised: It is needed the input patterns of the network and the desired output associated with input patterns. It must adjust the value of the weights using a mathematical formula to minimize error, in order to get the output of the system as close as possible to the desired output.

2. Unsupervised: It is not needed to display the desired patterns in the output.

B.1.2   Transfer functions

The transfer function calculates the activation level of the neuron according to the total input and it also denotes the total output of the neuron. The main tasks carried out by the transfer functions are firstly, limiting the output to ensure that the output values are not too high (this does not happen in the biological neural networks), and second place, to provide non-linearity characteristics. The transfer function is chosen according to the specifications of each problem to be solved. The most common transfer functions are listed below, but in [51] these functions are explained with more details.

- *Step function or hard limiting function (Hardlim)*: Matches the network output to 0 if the input argument is less than 0, and equals 1 if the input argument is greater than or equal to 0 . It is commonly used in Perceptron networks, which are common in making decisions and classification. Its equation is:

$$\mathrm{hardlim}(n) = \begin{cases} 1 & \text{if } n \geq 0 \\ 0 & \text{otherwise} \end{cases} \tag{B.4}$$

- *Linear transfer function or pure linear (Purelin)*: The output value is equal to the value entered in the entry. Its expression is:

$$\text{linear}(n) = n \tag{B.5}$$

- *Sigmoidal transfer function or logarithmic sigmoidal function (Logsig)*: Takes the input value, that ranging between plus and minus infinity, giving an output bounded value in the range of 0 to 1. It is often used in multilayer Backpropagation networks. This function can be written as

$$\text{logsig}(n) = \frac{1}{1 + \text{e}^{-n}} \tag{B.6}$$

- *Hyperbolic tangent sigmoid function (Tansig)*: Takes the input value, ranging between plus and minus infinity, giving an output bounded value in the range of -1 to 1. This function can be written as

$$\text{tansig}(n) = \frac{2}{1 + \text{e}^{-2n}} - 1 \tag{B.7}$$

- *Symmetric saturating linear function (Satlins)*: Takes the input value, ranging between plus and minus infinity. The output value of the network will be equal to -1 if the input value is less than or equal to - 1, however, the output value will be equal to the value input if the input value is greater than -1 but less than or equal to 1, and the output will be equal to 1 if the input is greater than or equal to 1. Its expression is:

$$\text{satlins}(n) = \begin{cases} -1 & \text{if } n \leq -1 \\ n & \text{if } -1 \leq n \leq 1 \\ 1 & \text{if } n \geq 1 \end{cases} \tag{B.8}$$

B.1.3 ANN topology

Neurons are the basic elements that form an ANN, but neurons are distributed in parallel on different layers. The most common structure of an ANN is:

- Input layer: It is made by each of the input patterns. The number of entries is equal to the number of elements which each input vector or pattern has.

- Output layer: This is the last layer of neurons in the network. The number of neurons in this layer is equal to the number of outputs of the network.

- Hidden layers: They are located between the input and output layers. The ANN will posses hidden layers when the number of layers is greater than 1, therefore, if the neural network has only one layer, it will be the output. The number of neurons in the hidden layer is variable and they may have different connections between them, and even these connections will determine the topology of the network.

The nomenclature used to express the structure of a network is $R/H/O$, where R represents the number of entries to the network, the H letter indicates the number of neurons in the hidden

Input   **Layer 1**   **Layer 2**   **Layer 3**

$$\mathbf{y}^{(1)} = \mathbf{f}^1(\mathbf{W}^{(i)}{}_{11} \cdot \mathbf{p} + \mathbf{b}^{(1)}) \quad \mathbf{y}^{(2)} = \mathbf{f}^2(\mathbf{W}^{(h)}{}_{21} \cdot \mathbf{y}^{(1)} + \mathbf{b}^{(2)}) \quad \mathbf{y}^{(3)} = \mathbf{f}^3(\mathbf{W}^{(o)}{}_{32} \cdot \mathbf{y}^{(2)} + \mathbf{b}^{(3)})$$

$$\mathbf{y}^{(3)} = \mathbf{f}^3(\mathbf{W}^{(o)}{}_{32} \cdot \mathbf{f}^2(\mathbf{W}^{(h)}{}_{21} \cdot \mathbf{f}^1(\mathbf{W}^{(i)}{}_{11} \cdot \mathbf{p} + \mathbf{b}^{(1)}) + \mathbf{b}^{(2)}) + \mathbf{b}^{(3)})$$
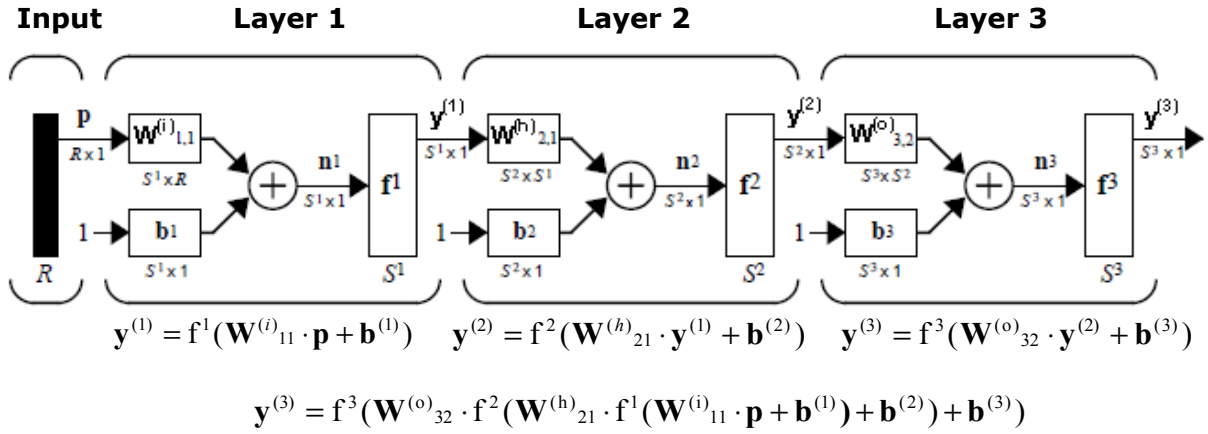
Figure B.3: ANN multilayer with abbreviated notation.

layer, and O is the number of output neurons of the neural network.

In the figure B.1 it is shown a neural network with R number of entries, where $\mathbf{p} = [p_1, p_2, ..., p_R]$ are the individual inputs multiplied by their corresponding weights $w_{1.1}, w_{1.2}, w_{1.3}, ..., w_{1,R}$ belonging to the weight matrix $\mathbf{W}$ and $\mathbf{b}$ is the gain of the neuron. The subscripts of the weights matrix $\mathbf{W}$ indicate the connections among elements. The first subscript indicates the target neuron and the second subscript represents the source of the input signal to the neuron, for example $w_{element1.3}$ indicates the connection of the third input with the first neuron. The output n will be:

$$n = p_1 w_{1,1} + p_2 w_{1,2} + \cdots + p_R w_{1,R} + \mathbf{b} \tag{B.9}$$

It can also be expressed in matrix notation for one neuron, where $\mathbf{p}$ is a column vector of $R \times 1$ elements and $\mathbf{W}$ is a row vector of dimension $1 \times R$ elements, as it is shown below:

$$n = \mathbf{W}\mathbf{p} + b \tag{B.10}$$

However, for a single layer ANN with S number of neurons in the layer, as it is the case shown in figure B.2, each R inputs are connected to the S neurons, therefore, the weight matrix has S rows and its size is $S \times R$. Besides the column vectors $\mathbf{a}$ and $\mathbf{b}$ have the dimension $S \times 1$

$$\mathbf{a} = f(\mathbf{W}\mathbf{p} + \mathbf{b}) \tag{B.11}$$

Multilayer neural networks are more powerful than single layers networks.

B.2 Multilayer Perceptron or MLP

The *Perceptron* was developed by F. Rosenblatt in 1962, according to the studies of Pitts and McCulloch about biological neurons. The *Perceptron* is a feedforward network, with only one layer, transfer functions and learning algorithm. The *Multilayer Perceptron* or MLP is an extension of a *Perceptron*. It consists of an input layer, an output layer and, at least, one hidden layer. The hidden layer of MLPs makes the conversion of dependent linear functions on independent linear function. It is one of the most important examples of artificial neural networks with supervised learning. The main virtue of a MLP network is that it can approximate universal functions.

Another important property of MLP networks is that they are capable of managing high dimensional tasks using relatively simple architecture. This set of properties makes MLP networks in general purpose tools, flexible and nonlinear.

B.2.1 Architecture of Multilayer Perceptron (MLP)

The *Multilayer Perceptron* is composed of an input layer, one or more hidden layers and an output layer. These layers are joined to spread the information forward (feedforward), flowing from the input layer to hidden layer, and from there to the output layer. The *Multilayer Perceptron* accepts real values.

Neurons in the hidden layer use the weighted sum of inputs with weights $w_{i,j}$ as a propagation rule, and above this weighted sum applies a transfer function, limiting the response. In this study, it is considered that the transfer function used in hidden layer is a tansig function and in the output layer is a purelin function. Hence, it can be written:

$$\mathbf{y}^{(h)} = \text{tansig}(\mathbf{W}^{(h)}\,\mathbf{p} + \mathbf{b}^{(h)}) \quad \text{and} \quad \mathbf{y}^{(o)} = \text{purelin}(\mathbf{W}^{(o)}\,\mathbf{y}^{(h)} + \mathbf{b}^{(o)}) \tag{B.12}$$

The learning that is typically used in such networks is called *Backpropagation*. As a global cost function, it is used the *mean square error*. That is, given a pair of values (p_k, t_k) input, being p the training data and t the associated desired output, it is calculated the sum of partial errors due to each pattern (referenced with index z), resulting from the difference between the desired output t_k and the output provided by the network with input vector p_k:

$$E(w_{i,j}, \theta, w'_{k,j}, \theta'_k) = \frac{1}{2} \sum_z \sum_k \left[d^z_k - f\left(\sum j w'_{k,j} y^z_j - \theta'_k \right) \right] \tag{B.13}$$

The *mean square error* will be high if the output obtained is very different from the desired output. In equation (B.13) f represents the activation function of neurons in the output layer and y represents the output that neurons of the last hidden layer provide. A minimization procedure is applied on this global cost function, using a descent gradient.

The learning algorithm *Backpropagation* performs the following steps:

1. Initialises the initial weights and thresholds for each neuron, being the most common the introduction of small random values.

2. For each pattern of the training data set:

   - The network response is got with that pattern, where the outputs of one layer serve as inputs to neurons in the next layer, processing them according to the rule of propagation and the corresponding activation function.

   - Associated errors are calculated.

   - The partial increases are calculated (addends of the sums).

3. The total increase in the weights and thresholds for all patterns are calculated.

4. Weights and thresholds are updated.

5. The current error is calculated, and return to step 2 if the result is not satisfactory.

B.3   Training algorithms

The network training is done once the weights and profits of the neural network have been initialised. The network can be trained by function approximation (nonlinear regression), by pattern classification or pattern association. The training process requires a set of input-output patterns (p_i, t_i) to define the correct behaviour of the network. During the training, weights and profits of the network are adjusted iteratively to minimize the error function of the network. This error function, for feedforward neural networks, is by default the *mean square error* or *mse* (average error between network outputs and desired outputs).

The most commonly used training algorithms are explained below. They use the gradient of the error function to determine the adjustment of the weights to reduce the error to a minimum. The technique *Backpropagation* is used to determine the gradient, making calculations back through the network.

1. **Backpropagation Algorithm**
   There are many variations of the algorithm *Backpropagation*. The simplest solution fits the profits and weights in the direction in which the error function decreases as rapid as possible, going in the negative direction of the gradient. An iteration (k) of this algorithm can be expressed as follow:

   $$\mathbf{w}_{k+1} = \mathbf{w}_k - \alpha_k \, \mathbf{g_k} \qquad (B.14)$$

   where $\mathbf{w}_k$ is the current weights vector and profits, g_k is the current gradient and α_k is the rate of learning.

2. **Gradient descent with momentum and adaptive learning rate backpropagation algorithm (GDX)**
   This algorithm is based on the algorithm of *Backpropagation*, but it provides a modification that makes it faster. The implementation of this algorithm is very sensitive to the parameter value associated with the learning rate α_k, since it allows the learning rate α_k to change during the training process. When the value of α_k is too high, the performance of this algorithm may oscillate and becomes unstable. However, if α_k is too small, the algorithm may spend too much time to converge. It is not easy to determine an optimum fixed value for this parameter, in fact, this optimal value varies along the algorithm execution. GDX algorithm proposes a variable value of the parameter α_k. For each iteration this algorithm will search for a largest possible value for α_k to be stable.

3. **Levenberg-Marquardt backpropagation algorithm (LM)**
   This algorithm tries to exploit the best features of the Newton's method and descent gradient algorithm. Newton's method is faster, and it converges in fewer iterations and is more accurate than the descent gradient algorithm. However, it requires greater computing power when it operates and stores data, since for each iteration is needed to compute the Hessian matrix for the error function used in the neural network. The update of the coefficients for each iteration is expressed as

$$\mathbf{x}_{k+1} = \mathbf{x}_k - \mathbf{A}_k^{-1} \, \mathbf{g}_k \tag{B.15}$$

where $\mathbf{A}_k$ is the Hessian matrix.
LM algorithm makes the following approaches (if the network uses an error function of the form of quadratic sums, such as mean square error) to avoid computing the Hessian matrix:

$$\mathbf{H} = \mathbf{J}^T \, \mathbf{J} \tag{B.16}$$

$$\mathbf{g} = \mathbf{J}^T \, \mathbf{e} \tag{B.17}$$

where $\mathbf{J}$ is the Jacobian matrix (easier to compute than Hessian matrix), $\mathbf{g}$ is the gradient and $\mathbf{e}$ are the errors network vector.

The Levenberg-Marquardt algorithm is a hybrid between the Newton's method and descent gradient algorithm. Therefore, after each iteration the error function of the neural network is discussed, if the function is reduced, the Newton's method will still apply. Instead, if the error function increases, a method closer to the descending gradient algorithm will be applied .The dependence of the LM algorithm with Newton's method and the descending gradient algorithm can be written down as

$$\mathbf{x}_{k+1} = \mathbf{x}_k - [\mathbf{J}^T \, \mathbf{J} + \mu \, \mathbf{I}]^{-1} \, \mathbf{J}^T \, \mathbf{e} \tag{B.18}$$

In this case, μ represents the coefficient that will give more or less importance to the descent gradient algorithm. Then, if μ is small, the algorithm used will be close to the Newton's method, but if μ is high, an algorithm similar to the descending gradient algorithm will be applied.

B.4   Procedure to determine the ANNs

The training process of neural networks consists of four phases. First of all a data collection is performed, which is used as input vectors to the neural network. Secondly, the neural network is created, defining the structure, and the number of layers and the number of neurons in them. In third place, the networks created will be training to learn the ANN to distinguish the two types of patterns. And finally, the correct behaviour of the trained network will be verified, where new input vectors, different from training pattern, will be presented to the ANN, to check the output produced, and determine if the trained network is generalized to any kind of input vectors to follow the same pattern.

B.4.1   Stage 1: Collection of observation vectors

In this first stage the different vectors are formed. The data used for the analysis are from the platform under study. Three groups of vectors should be generated. Each group of vectors is generated to be used in a specific phase with a specific mission. These groups of vectors are called: *training vector*, *validation vector* and *test vector or test*. The training and validation vectors are used in the training stage, however the test vector is used in the testing stage.

B.4.2   Stage 2: Creation of the neural network

In this stage the structure of the ANN will be defined. It is necessary to know the number of layers, the number of neurons that will have each layer, the interconnection between the layers and the activation function used by each neuron in the network.

The neural network used in this thesis will be a Multilayer Perceptron (MLP) with supervised learning. The number of neurons will be:

- R neurons in the input layer: These are due to the R input parameters that will used to analyse the behaviour of the sea.

- S neurons in the hidden layer: This number of neurons has been selected because of the computational load is not very high and the *mse* and results obtained for this number are very similar than the others obtained with more neurons in hidden layer.

- N neuron in the output layer: One neuron for each parameter under study to be determined.

The activation functions used for the hidden and output layer are respectively tansig and purelin. The training algorithm will be Levenberg-Marquardt because the *mse* obtained is the lowest in compare to other training algorithms.

B.4.3   Stage 3: Training of the ANN

In this stage, the intrinsic parameters used in the neural network are calculated, such as the weights and gains. These parameters can be initialised to certain or random values. During the training process these values are iteratively adjusted to minimize the error at the output of the network. This error is the difference between the desired outputs and actual outputs obtained from the network. The *mean square error (mse)* will be used as error function and the objective is to minimize this error function during training.

In this stage *training vectors* and *validation vectors* are necessary. The neural network will try to learn from the training vectors that serve as input to the neural network. Through training and learning algorithm used, the network will readjust in each iteration its internal coefficients (weights and gains) to get the outputs of the network are equal, or as close as possible, to the relevant objectives of the training vectors.

Validation vectors are used to improve network generalization. The outputs of the network should match the desired outputs, but without distancing from the objectives of validation vectors. When the outputs of the network exceed the threshold distance respect to the objectives of validation vectors, training will be interrupted and it will finish. For this reason, better results will get in the generalization of the network, achieving a better performance when new input vectors are presented to the network.

B.4.4   Stage 4: ANN simulation

When the network is trained it can proceed with the simulation or testing phase. In this stage new input vectors are introduced into the network to analyse their outputs. These vectors are different to the training and validation vectors.

To evaluate the performance of the network, the error and its deviation must be computed. The parameters are:

- Mean squared error (mse): Is the difference between the desired outputs and actual outputs obtained from the network.

- Error deviation: Is the standard deviation of the mean squared error.

- Correlation coefficient (r): Measures the strength and the direction of a linear relationship between two random variables. If its value is close to 1, the two variables are very similar; However, if its value is close to 0, the two variables will be very different. In this thesis, these two variables will be the data provided by the ADCP sensor and the actual output obtained by the ANN.

$$r = \frac{\sum (x_i - \overline{x})(y_i - \overline{y})}{N \, \sigma_x \, \sigma_y} \tag{B.19}$$

where $\overline{x}$ is the average of the desired output, $\overline{y}$ is the average of the actual output, σ_x is the standard deviation of the desired output, σ_y is the standard deviation of the actual output and N is the number of elements of the desired output vector.

Appendix C

Extreme Learning Machines

It is an avant-garden and fast learning method which is based on a feedforward MLP structure. The most important characteristic is that the weights in hidden layer are not calculated and for this reason, this layer do not need be trained. The network weights are setting randomly and then a pseudo-inverse of hidden layer output matrix is estimated.

The essence of the ELM resides in:

- The hidden layer of the net should not be calculated recurrently.

- The train error $\|\mathbf{H}\beta - \mathbf{T}\|$ and the norm of the weights $\|\beta\|$ have to be minimized.

- The weights of the nodes in the hidden layer $\|\beta_i\|$ can be generated randomly. Therefore the weight vectors between the hidden and output layers can be calculated directly with minimum squared.

C.1   Basic ELM

Once the parameters of the nodes $(\mathbf{w}_i, b_i)$ are set up, they will be fixed. Training the net is equivalent to find the solution of the lineal system by minimum squared $\mathbf{H}\beta = \mathbf{T}$

$$\left\|\mathbf{H}\hat{\beta} - \mathbf{T}\right\|_{min\,\beta} = \|\mathbf{H}\beta - \mathbf{T}\| \tag{C.1}$$

being $\mathbf{T} = [u_1, \cdots, u_l]^T$ the training output vector.

If the number of hidden nodes $(\widetilde{N})$ are equal to the number of training samples (L), the matrix $\mathbf{H}$ will be squared and $\mathbf{H}$ can be inverted when the parameters $(\mathbf{w}_i, b_i)$ are choose randomly. But the most of time, the number of hidden nodes is less than the number of training samples. Hence the matrix $\mathbf{H}$ is not squared and the $(\mathbf{w}_i, b_i, \beta_i)$ cannot verify $\mathbf{H}\beta = \mathbf{T}$. Therefore, the equation that minimize the system using minimum squared is:

$$\hat{\beta} = \mathbf{H}^\dagger \mathbf{T} \tag{C.2}$$

being $\mathbf{H}^\dagger$ the Moore-Penrose inverse of matrix $\mathbf{H}$ [54]

For this algorithm is needed a training set ($\mathbb{T}$), an activation function ($g(x)$) and the of hidden nodes ($\widetilde{N}$). The training set is:

$$\mathbb{T} = (\mathbf{x_i}, \mathbf{u_i}) \quad \text{where} \quad \mathbf{x_i} \in \text{Re}^n, \, u_i \in \text{Re}, \, i = 1, \cdots, l \tag{C.3}$$

The main steps in ELM algorithm are the following:

1. Input weights $\mathbf{w_i}$ and bias b_i (being $i = 1, \cdots, l$) are assigned randomly.

2. The hidden layer output matrix $\mathbf{H}$ is calculated. The size of the matrix $\mathbf{H}$ is $l \times \widetilde{N}$ and it is defined as:

$$\begin{bmatrix} g(\mathbf{w_1}\mathbf{x_1} + b_1) & g(\mathbf{w_{\widetilde{N}}}\mathbf{x_{\widetilde{N}}} + b_{\widetilde{N}}) \\ \vdots & \vdots \\ g(\mathbf{w_1}\mathbf{x_l} + b_1) & g(\mathbf{w_{\widetilde{N}}}\mathbf{x_{\widetilde{N}}} + b_{\widetilde{N}}) \end{bmatrix} \tag{C.4}$$

3. The output weight vector β is calculated as:

$$\beta = \mathbf{H}^\dagger \mathbf{T} \tag{C.5}$$

The ELM algorithm can use several activation functions and it can be used to train directly networks. The number of hidden nodes must be estimated and is a free parameter of the ELM training.

C.2   ELM based on random mapping of the hidden layer

The orthogonal projection method could be used in the ELM:

- $\mathbf{H}^\dagger = (\mathbf{H}^T\mathbf{H})^{-1}\mathbf{H}^T$ if $\mathbf{H}^T\mathbf{H}$ is not singular.

- $\mathbf{H}^\dagger = \mathbf{H}^T(\mathbf{H}\mathbf{H}^T)^{-1}$ if $\mathbf{H}\mathbf{H}^T$ is not singular.

According to the regression theory, a positive number $1/\lambda$ could be added in the main diagonal of $\mathbf{H}^T\mathbf{H}$ or $\mathbf{H}\mathbf{H}^T$ to calculate the output weight vector, supplying stability and better training generalization. The algorithm is the same than the basic ELM commented before, but the only difference is the method to calculate the output weight vector:

$$\beta = \mathbf{H}^T \left(\frac{\mathbf{I}}{\lambda} + \mathbf{H}\mathbf{H}^T \right)^{-1} \mathbf{T} \quad ; \quad \beta = \left(\frac{\mathbf{I}}{\lambda} + \mathbf{H}^T\mathbf{H} \right)^{-1} \mathbf{H}^T\mathbf{T} \tag{C.6}$$

The output function of the ELM is: $f(\mathbf{x}) = \mathbf{h}(\mathbf{x})\beta$

Appendix D

Gaussian Process for Regression

Gaussian Process for Regression (GPR) is a generic supervised learning method use to solve regression problems. GPR is a kind of continuous stochastic process that defines a distribution of probability for functions and inferences taking place directly in the space of functions. In [55] can be found an extensive information about GPR, however here a brief summarise is presented.

D.1   Gaussian distribution

The Gaussian distribution is the most usual distribution. The probability function is:

$$p(y|\mu\sigma^2) = \frac{1}{\sqrt{2\pi\sigma^2}}\mathrm{e}^{\left(-\frac{(x-\mu)^2}{2\sigma^2}\right)} = \mathcal{N}(\mu, \sigma^2) \tag{D.1}$$

The mean value, or mathematical expectation is $\mathrm{E}(x) = \mu$, the variance is equal to σ^2 and the standard deviation is σ

The main property is that the addition of Gaussian is a Gaussian as well. If the terms of the addition is increasing, the addition of the independent aleatory variables tends to a Gaussian

$$\sum_{i=1}^{n} y_i \sim \mathcal{N}\left(\sum_{i=1}^{n} \mu_i, \sum_{i=1}^{n} \sigma_i^2\right)$$

Another property is that if Gaussian is multiplied by a constant, the product is a Gaussian as well

$$c \cdot y \sim \mathcal{N}\left(c \cdot \mu, c^2 \cdot \sigma_i^2\right)$$

In general, the definition of the multivariable Gaussian distribution is:

$$p(y|\mu\Sigma) = \frac{1}{(2\pi)^{n/2} |\Sigma|^{1/2}}\mathrm{e}^{-\frac{1}{2}(\mathbf{X}-\mu)^T\Sigma^{-1}(\mathbf{X}-\mu)} \tag{D.2}$$

being $\mathbf{X}$ the vector of variables and Σ the matrix of covariance among variables.

D.2 Gaussian Process

A Gaussian process is an extension towards infinite variables collection. Therefore, the Gaussian process is a distribution of distributions aleatory functions. It means, the Gaussian process is a stochastic process so that any subset of finite aleatory variables has a multivariable Gaussian distribution. In general, a finite set of aleatory variables $h(x_1), h(x_2), \ldots, h(x_m)$ has the following distribution:

$$\begin{bmatrix} \boldsymbol{h(x_1)} \\ \vdots \\ \boldsymbol{h(x_m)} \end{bmatrix} \sim \mathcal{N} \left(\begin{bmatrix} m(x_1) \\ \vdots \\ m(x_m) \end{bmatrix}, \begin{bmatrix} k(\mathbf{x}_1, \mathbf{x}_1) & k(\mathbf{x}_1, \mathbf{x}_m) \\ \vdots & \vdots \\ k(\mathbf{x}_m, \mathbf{x}_1) & k(\mathbf{x}_m, \mathbf{x}_m) \end{bmatrix} \right) \tag{D.3}$$

The distribution can be denoted as: $h(\cdot) \sim \mathfrak{GP}(m(\cdot), k(\cdot, \cdot))$, where $m(\cdot)$ is the mathematical expectation function and it is a real function, $k(\cdot, \cdot)$ is the covariance function and it is a Kernel.

In this particular case, the data set is $\mathcal{D} \equiv \mathbf{x}_n, u_{n\,i=1}^{l}$, where $\mathbf{x}_n$ is the N-dimensional inputs and u_n is their corresponding scalar outputs. The target of the GPR is getting the predictive distribution, so when a new input $\mathbf{x}_*$ is introduced in the system, its corresponding observation u_* is obtained based on $\mathcal{D}$. In the GPR method, each observed target value u can be written as:

$$f(\mathbf{x}) = \mathbf{x}^T \mathbf{w} \qquad u = f(\mathbf{x} + \epsilon) \tag{D.4}$$

where $f(\mathbf{x})$ is the function value, $\mathbf{x}$ is the input vector, $\mathbf{w}$ is the vector of weights and ϵ is the noise. The model assumes that each observation u differs from the function value $f(\mathbf{x})$ by additive noise ϵ. This noise is independent and follows identically distributed Gaussian distribution with zero mean and variance σ^2, therefore noise $\epsilon \sim \mathcal{N}(0, \sigma^2)$. Therefore, it is possible to say that $f(\mathbf{x}) \sim \mathfrak{GP}(0, k(\mathbf{x}, \mathbf{x}'))$. The Gaussian distribution for the noise will be:

$$\begin{bmatrix} \boldsymbol{\epsilon} \\ \boldsymbol{\epsilon_*} \end{bmatrix} \sim \mathcal{N} \left(\mathbf{0}, \begin{bmatrix} \sigma^2 \mathbf{I} & \mathbf{0} \\ \mathbf{0}^T & \sigma^2 \mathbf{I} \end{bmatrix} \right) \tag{D.5}$$

To express this model as matrix notation, it is necessary to work with the covariance function $k(\mathbf{x}, \mathbf{x}')$. The covariance function will be high when $u(\mathbf{x})$ and $u(\mathbf{x}')$ are close in the space, however the covariance will be low they are separated. The predictive distribution is a multivariate Gaussian distribution, and can be expressed as:

$$\begin{bmatrix} \boldsymbol{u} \\ \boldsymbol{u_*} \end{bmatrix} = \begin{bmatrix} \mathbf{h} \\ \mathbf{h_*} \end{bmatrix} + \begin{bmatrix} \epsilon \\ \epsilon_* \end{bmatrix} \tag{D.6}$$

$$\begin{bmatrix} \boldsymbol{u} \\ u_* \end{bmatrix} \sim \mathcal{N} \left(0, \begin{bmatrix} k(\mathbf{X}, \mathbf{X}) + \sigma^2 \mathbf{I}_N & k(\mathbf{X}, \mathbf{X}_*) \\ k(\mathbf{X}_*, \mathbf{X}) & k(\mathbf{X}_*, \mathbf{X}_*) + \sigma^2 \end{bmatrix} \right) \tag{D.7}$$

being $\mathbf{I}_N$ the identity matrix of size N. From equation (D.7) it is possible to obtain the main characteristics from the distribution GPR:

$$p_{\mathfrak{GP}}(u_*|\mathbf{x}_*, \mathcal{D}) = \mathcal{N}(u_*|\mu_{\mathfrak{GP}*}, \sigma^2_{\mathfrak{GP}*})$$

$$\mu_{\mathfrak{GP}*} = k(\mathbf{X}_*, \mathbf{X})(\mathbf{K} + \sigma^2\mathbf{I}_N)^{-1}\mathbf{u} \qquad\qquad (D.8)$$

$$\sigma^2_{\mathfrak{GP}*} = \sigma^2 + k(\mathbf{X}_*, \mathbf{X}_*) - k(\mathbf{X}_*, \mathbf{X})(\mathbf{K} + \sigma^2\mathbf{I}_N)^{-1}k(\mathbf{X}, \mathbf{X}_*)$$

Some advantages are that GPR interpolates the observations, the prediction is a Gaussian probability and simplicity of implementation. The main drawback is that the flexibility is limited.

Appendix E

Support Vector Regression Algorithms

Support Vector Regression Algorithms (SVR) are a set of supervised learning algorithms developed by Vladimir Vapnik and his team. They are related to linear classification and regression problems. A SVR builds a hyperplane in high dimensional space, where the hyperplane separates in optimal way the samples of different classes. The SVR searches the hyperplane, or a set of hyperplanes, whose distance between the samples and itself is maximal. An algorithm based on SVR determines in which category is a new input sample.

The models based on SVR are related to neural network. The main idea of SVR consists on doing a nonlinear mapping $(\varphi : X \rightarrow F)$ with the training samples $x \in X$, towards bigger space F, where a linear regression can be done.

In a generic classification problem there is a training set with independent samples $(\mathbf{x}_i, u^i), i = 1, \ldots, l \in X \times U$. The vector $\mathbf{x}_i$ has a probability density function $p(\mathbf{x})$ and the connection between the samples and their labels u^i is represented by an unknown determined probability density function $u|\mathbf{x}$. The classification system uses a set of functions $f(\mathbf{x}, \mathbf{w}), \mathbf{w} \in W$ to give a label $\widehat{u}^i = f(\mathbf{x}_i, \mathbf{w})$ for an input $\mathbf{x}_i$. The aim of the learning process is selecting the function $f(\mathbf{x}, \mathbf{w})$ in a proper way, minimizing the discrepancies between the true labels (u^i) and the labels provided by the SVR $(\widehat{u}^i)$. To evaluate this approximation, a cost function (or loss function) $c(u, f(\mathbf{x}, \mathbf{w}))$. Then the risk function of the SVR having used the function $f(\mathbf{x}, \mathbf{w})$ is calculated as:

$$R_{empirical} = \frac{1}{l} \sum_{i=1}^{l} c(u^i, f(\mathbf{x}_i, \mathbf{w})) \tag{E.1}$$

The risk must be minimizing to get better results.

E.1 Support Vector Regression

The SVR method for regression consists of training a model with a set of training vectors $\mathbb{T}$:

$$\mathbb{T} = (\mathbf{x_i}, \mathbf{u^i}) \quad \text{where } i = 1, \ldots, l \tag{E.2}$$

$$\widehat{u}(\mathbf{x}) = g(\mathbf{x}) + b = \mathbf{w}^T \phi(\mathbf{x}) + b \tag{E.3}$$

being $\mathbf{x}$ the vector of predictive variables, $u(\mathbf{x})$ in this particular case is the ADCP measures of the current ($u^i = |\mathbf{U}^{i-s}|$), $\widehat{u}(\mathbf{x})$ is the estimation of the current provided by the SVR, b the bias and ϕ a function of protection of the input space to the feature space ($\phi : \mathbb{R}^d \to \mathfrak{H}$).

The cost function accepts a maximum deviation ε of the function $g(x)$ without penalty:

$$L\left(u^i, g(\mathbf{x}_i)\right) = \begin{cases} 0 & \text{if } |u^i - g(\mathbf{x}_i)| \leq \varepsilon \\ |u^i - g(\mathbf{x}_i)| - \varepsilon & \text{otherwise} \end{cases} \tag{E.4}$$

The risk function must be minimizing and it can be expressed as:

$$R[g] = \frac{1}{2} \|\mathbf{w}\|^2 + C \sum_{i=1}^{n} c(u^i, g(\mathbf{x}_i)) \tag{E.5}$$

where C determines the agreement between the smoothness of the function $g(\mathbf{x})$ and the deviations greater than the threshold error ε that are allowed.

En error lower than ε is not always possible, therefore width variables ($\xi_i, \xi_i^* > 0$, $i = 1, \ldots, n$) are introduced. This model has to be trained optimizing the problem:

$$\min \left(\frac{1}{2} \|\mathbf{w}\|^2 + C \sum_{i=1}^{l} (\xi_i + \xi_i^*) \right) \tag{E.6}$$

subject to:

$$u^i - \mathbf{w}^T \phi(\mathbf{x}_i) - b \leq \varepsilon + \xi_i, \quad i = 1, \ldots, l \tag{E.7}$$

$$-u^i + \mathbf{w}^T \phi(\mathbf{x}_i) + b \leq \varepsilon + \xi_i^*, \quad i = 1, \ldots, l \tag{E.8}$$

$$\xi_i, \xi_i^* \geq 0, \quad i = 1, \ldots, l \tag{E.9}$$

Lagrange variables ($\alpha_i, \alpha_i^*, \mu_i, \mu_i^*$) are introduced, and the equation (E.6) will be written as:

$$L_p = \frac{1}{2} \|\mathbf{w}\|^2 + C \sum_{i=1}^{l} (\xi_i + \xi_i^*) - \sum_{i=1}^{l} \mu_i \xi_i + \mu_i^* \xi_i^*$$

$$- \sum_{i=1}^{l} \alpha_i \left[\varepsilon + \xi_i - u^i + (\mathbf{w}^T \phi(\mathbf{x}_i) + b) \right] -$$

$$- \sum_{i=1}^{l} \alpha_i^* \left[\varepsilon + \xi_i^* + u^i - (\mathbf{w}^T \phi(\mathbf{x}_i) + b) \right] \tag{E.10}$$

The equation (E.10) must be minimized by $\mathbf{w}, b, \xi_i^*$ and must be maximized respect to $\alpha_i, \alpha_i^*, \mu_i, \mu_i^*$. In this case, the dual form of the optimization problem is the following:

$$\max \left(-\frac{1}{2} \sum_{i=1}^{l} \sum_{j=1}^{l} (\alpha_i - \alpha_i^*)(\alpha_j - \alpha_j^*) \phi(\mathbf{x}_i) \phi(\mathbf{x}_j) - \varepsilon \sum_{i=1}^{l} (\alpha_i + \alpha_i^*) + \sum_{i=1}^{l} u^i (\alpha_i - \alpha_i^*) \right) \tag{E.11}$$

subject to:

$$\sum_{i=1}^{l} (\alpha_i - \alpha_i^*) = 0 \quad where \quad \alpha_i, \alpha_i^* \in [0, C] \tag{E.12}$$

The equation (E.11) expressed in matrix form is:

$$\max \left(-\frac{1}{2} \sum_{i,j=1}^{l} (\alpha_i - \alpha_i^*)(\alpha_j - \alpha_j^*) K(\mathbf{x}_i, \mathbf{x}_j) - \varepsilon \sum_{i=1}^{l} (\alpha_i + \alpha_i^*) + \sum_{i=1}^{l} u^i (\alpha_i - \alpha_i^*) \right) \tag{E.13}$$

The optimization problem is equivalent to the dot product $\langle \phi(\mathbf{x}_i), \phi(\mathbf{x}_j) \rangle$, which can be evaluated by a Kernel function $K(\mathbf{x}_i, \mathbf{x}_j)$:

$$K(\mathbf{x}_i, \mathbf{x}_j) = \mathrm{e}(-\gamma \cdot \|\mathbf{x}_i - \mathbf{x}_j\|^2). \tag{E.14}$$

In summarise, the equation (E.3) can be written as a function related to a Kernel matrix $K(\mathbf{x_i}, \mathbf{x})$ and Lagrange multipliers (α_i, α_i^*):

$$\widehat{u}(\mathbf{x}) = g(\mathbf{x}) + b = \sum_{i=1}^{l} (\alpha_i - \alpha_i^*) K(\mathbf{x}_i, \mathbf{x}) + b \tag{E.15}$$

A complete explanation is presented in [56].

Appendix F

Published contributions

The following published contributions have been achieved in the frame of this work:

- Lidó-Muela, C., Carrasco, R. and Horstmann, J., Retrieval of Ocean Surface Wind Fields from Marine Radar Image Sequences. FR4.9.FR4.9.1, *IEEE International Geoscience and Remote Sensing Symposium. IGARSS 2012.* 22-26 July 2012, Munich, Germany. 2012. pp. 4.

- Vicen-Bueno, R., Lidó-Muela, C., and Nieto Borge, J.C., Estimate of significant wave height from non-coherent marine radar images by multilayer perceptrons. *EURASIP Journal on Advances in Signal Processing.* 2012, vol. 2012:84, pp. 1-20.
  Impact Factor (JCR): **0.928**.

- Lidó-Muela, C., Cornejo-Bueno, L., Nieto Borge, J. C., Hessner, K., and Salcedo-Sanz, S., Robust Estimation of Near-surface Sea Currents using X-Band Radar Measurements and Machine Learning Techniques. Submitted to *Journal of Marine Systems*, 2015.
  Impact Factor (JCR): **2.174**.

Part IV

Bibliography

Bibliography

[1] S. Pond and G.L. Pickard. *Introductory Dynamical Oceanography.* Pergamon Press, 1983.

[2] J. Brown and G. Bearman. *Waves, Tides and Shallow–Water Processes.* Pergamon Press, USA, 2 edition, 2000.

[3] L. H. Holthuijsen. *Waves in Oceanic and Coastal Waters.* Cambridge University Press, USA, 1 edition, 2007.

[4] M. K. Ochi. *Ocean Waves: The Stochastic Approach.* Cambridge University Press, USA, 2 edition, 2008.

[5] J. C. Nieto Borge. The gaussian model of wind-generated waves. urlhttp://www.uio.no/studier/emner/matnat/math/MEK4350/h16/pensumliste/gaussian-waves.pdf, 2016.

[6] G.J. Komen, L. Cavaleri, and M. Donelan. *Dynamics and Modelling of Ocean Waves Paperback.* Cambridge University Press, 2008.

[7] C.M. Senet, J. Seemann, and F. Ziemer. The near-surface current velocity determined from image sequences of the sea surface. *IEEE Transactions on Geoscience and Remote Sensing*, 39(3):492–505, 2001.

[8] Ian R. Young, Wolfgang Rosenthal, and Friedwart Ziemer. A three dimensional analysis of marine radar images for the determination of ocean waves directionality and surface currents. *J. Geophys. Res.*, 90:1049–1059, July 1985.

[9] J. C. Nieto Borge. *Significant wave height estimation from nautical radar data sets.* Postdoctoral thesis, GKSS, 1998.

[10] G. Lindgren. *Stationary Stochastic Processes: Theory and Applications.* Chapman & Hall, UK, 1 edition, 2012.

[11] J.C. Nieto Borge, G. Rodriguez, K. Hessner, and P. Izquierdo. Inversion of marine radar images for surface wave analysis. *J. Atmos. Ocean. Technol.*, 21(8):1291–1300, 2004.

[12] C. Lidó de la Muela. *Estimate of significant wave height from marine radar images of the sea surface by using artificial neural networks.* Master thesis, University of Alcalá, 2011.

[13] L. Tsang, J. A. Kong, and K.-H. Ding. *Scattering of Electromagnetic Waves, Theories and Applications.* Wiley, USA, 2 edition, 2000.

[14] L. Tsang and J. A. Kong. *Scattering of Electromagnetic Waves, Advanced Topics.* Wiley, USA, 2 edition, 2001.

[15] J. C. Nieto Borge. *Análisis de campos de oleaje mediante radar de navegación en banda X.* Doctoral thesis, Universidad de Alcalá, 1996.

[16] Friedwart Ziemer and Heinz Günther. A system to monitor ocean wave fields. *Proc. of the Second Int. Conf. on Air-Sea Interaction and Meteorology and Oceanography of the Coastal Zone, Lisbon, Portugal*, 1994.

[17] H. Hatten. *Untersuchungen zur Korrelation des spektralen Rauschhintergrundes eines nautischen Radars mit dem Windgeschwindigkeitsvektor (in German).* Diplomarbeit, Universität Hamburg, 1998.

[18] K. Reichert. *Untersuchung zur azimuthalen Abhängigkeit der Abbildung von Seegang mit dem Schiffsradar (in German).* Diplomarbeit, Fachbereich Geowissenschaften Universität Hamburg, 1994.

[19] H. Dankert and W. Rosenthal. Ocean surface determination from X-band radar images sequences. *J. Geophysical Res., Oceans*, 109, 2004.

[20] F. Ziemer, C. Brockmann, R. A. Vaughan, J. Seemann, and C. M. Senet. Radar survey of near shore bathymetry within the oroma project. *EARSeL eProceedings*, 3(2):282–288, 2004.

[21] J. C. Nieto Borge and K. Hessner. Comparision of wamos ii with in situ measurements. *EU COST*, 714:465, 2005.

[22] F. Ziemer, W. Rosenthal, and H. Carlson. Measurements of directional wave spectra by ship radar. IAPSO Symp., General Assembly, Int. Assoc. for Phys. Sci. of the OceansHamburg, 1983.

[23] J. C. Nieto Borge and C. Guedes Soares. Analysis of directional wave fields using X-band navigation radar. *Coastal Ehg.*, 40:375–391, 2000.

[24] J.C. Nieto Borge, K. Hessner, P. Jarabo Amores, and D. de la Mata Moya. Signal-to-noise ratio analysis to estimate ocean wave heights from X-band marine radar image time series. *IET Radar Sonar Navig*, 2(1):35–41, February 2008.

[25] Werner Alpers and Klauss Hasselmann. Spectral signal to clutter and thermal noise properties of ocean wave imaging synthetic aperture radars. *International Journal of Remote Sensing*, 3(4):423–446, 1982.

[26] J. Seemann. *Interpretation der Struktur des Wellenzahl-Frequenzspektrums von Radar-Bildsequenzen. (in German).* Ph. d thesis, Universität Hamburg, 1997.

[27] José Carlos Nieto Borge. *Developments on the new dispersion shell filter for image time series of wave fields.* EPPE-CM and GKSS-GMS, January 1998.

[28] K. Bala Prakash, R. Venu Babu, and Venu Gopal B. Image independent filter for removal of speckle noise. *IJCSI International Journal of Computer Science Issues*, 8, September 2011.

[29] S. J. Frasier and R. E. McIntosh. Observed wavenumber–frequency properties of microwave backscatter from the ocean surface at near–grazing angles. *J. Geophys. Res.*, 101:18391–18407, 1996.

[30] C. L. Stevens, E. M. Poulter, M. J. Smith, and J. A. McCregor. Nonlinear features in wave–resolving microwave radar observations of ocean waves. *IEEE J. Ocean. Eng.*, 24(4):470–480, 1999.

[31] H. E. Krogstad and K. Trulsen. Interpretations and observations of ocean wave spectra. *Ocean Dynamics*, 60(4):973–991, 2010.

[32] R. Vicen Bueno, C. Lido-Muela, and J. C. Nieto Borge. Estimate of significant wave height from noncoherent marine radar images by multilayer perceptrons. *EURASIP Journal on Advances in Signal Processing*, 84, 2012.

[33] Jeffrey L. Hanson and Owen M. Phillips. Automated analysis of ocean surface directional wave spectra. *Journal of Atmospheric and Oceanic Technology*, February 2001.

[34] S. Salcedo-Sanz, J. C. Nieto Borge, L. Carro-Calvo, L. Cuadra, K. Hessner, and E. Alexandre. Significant wave height estimation using SVR algorithms and shadowing information from simulated and real measured X-band radar images of the sea surface. *Ocean Engineering*, 101(6):244–253, 2015.

[35] K. Ward, Tough R., and S. Watts. *Sea Clutter: Scattering, the K Distribution and Radar Performance.* IET Digital Library, UK, 2 edition, 2013.

[36] Z. Jie, C. Dong, and S. Dewei. K distribution sea clutter modeling and simulation based on ZMNL. In *2015 8th International Conference on Intelligent Computation Technology and Automation (ICICTA)*, pages 506–509, 2015.

[37] J.C. Nieto Borge, J. Schulz-Stellenfleth, A. Niedermeier, and S. Lehner. Analysis of statistical wave properties of linear and non linear two-dimensional wave fields derived from stochastic simulations. *ASCE Waves 2005 Int. Conf. Proc.*, 2005.

[38] K. Hasselmann, T. P. Barnett, E. Bouws, H. Carlson, D. E. Cartwright, K. Eake, and et al. Measurements of wind-wave growth and swell decay during the joint north sea wave project (jonswap). *Ergnzungsheft zur Deutschen Hydrographischen Zeitschrift Reihe*, 8(12):95, 1973.

[39] N. E. Huang, S. R. Long, C.-C. Tung, Y. Yuen, and L. F. Bliven. A unified two-parameter wave spectral model for a general sea state. *Journal of Fluid Mechanics*, 112:203–224, 1981.

[40] H. Mitsuyasu, F. Tasai, T. Suhara, S. Mizuno, M. Ohkusu, T. Honda, and et al. Observation of the power spectrum of ocean waves using a cloverleaf buoy. *Journal of Physical Oceanografy*, 10:286–296, 1980.

[41] Merrill I. Skolnik. *Introduction to radar systems.* McGraw-Hill International Editions, 3 edition, 2001.

[42] W.J. Plant and G. Farquharson. Origins of features in wave number-frequency spectra of space-time images of the ocean. *Journal of Physical Oceanografy*, 117:1–10, 2012.

[43] M. M. Lipschutz. *Schaum's Outline of Differential Geometry.* McGraw-Hill Education, USA, 1 edition, 1969.

[44] W. G. Rees. *Physical Principles of Remote Sensing.* Cambridge University Press, USA, 3 edition, 2012.

[45] J. C. Curlander and R. N. McDonough.

[46] C. Lido-Muela, L. Cornejo-Bueno, J. C. Nieto Borge, K. Hessner, and S. Salcedo-Sanz. Robust estimation of near-surface sea currents using X-band radar measurements and machine learning techniques. *Journal of Ocean Engineering*, October 2016.

[47] J. Röhrs, K. H. Christensen, L. R. Hole, G. Broström, M. Drivdal, and S. Sundby. Observation-based evaluation of the surface wave effects on currents and trajectory forecasts. *Ocean Dynamics*, 62:1519–1533, 2012.

[48] Diego Córdoba Gozalaz. *Las ecuaciones de Navier-Stokes.* Jornada sobre los problemas del milenio. Instituto de Ciencias Matemáticas, 2011.

[49] M.C. Palomino and J.L. Almazan. *Descripción, medida y análisis del oleaje.* E.T.S. Ingenieros de Caminos, Canales y Puertos, 2000.

[50] J.L. Vázquez. *La ecuación de Navier-Stokes. Un reto físico-matemático para el siglo XXI.* Departamento de Matemáticas. Univ. Autónoma de Madrid, 2004.

[51] C. M. Bishop. *Neural networks for pattern recognition.* Oxford University Press, Great Britain, 1 edition, 1995.

[52] R. Vicen-Bueno, Carrasco-Álvarez, M. R.and Rosa-Zurera, J. C. Nieto-Borge, and M. P. Jarabo-Amores. Artificial neural network-based clutter reduction systems for ship size estimation in maritime radars. *EURASIP J. Advances Signal Proc.*, 2010:1–15, Jan 2010.

[53] R. Vicen-Bueno, R. Carrasco-Álvarez, M. P. Jarabo-Amores, J. C. Nieto-Borge, and M. Rosa-Zurera. Ship detection by different data selection templates and multilayer perceptrons from incoherent maritime radar data. *IET Radar Son. Nav.*, 5(2):144–154, Feb. 2011.

[54] G.B. Huang and Q. Y. Zhu. Extreme learning machine: theory and applications. *Neurocomputing*, 70:489–501, 2006.

[55] M. Lázaro Gredilla, S. van Vaerenbergh, and N. Lawrence. Overlapping mixtures of gaussian process for the data association problem. *Pattern Recognition*, 45:1386–1395, 2012.

[56] A.J. Smola and B. Schölkopf. A tutorial on support vector regression. *Statistics and Computing*, 14:199–222, 2004.